universität wien

DISSERTATION / DOCTORAL THESIS

Titel der Dissertation /Title of the Doctoral Thesis

„Computational Spectroscopy of Solvation Phenomena in Soft Matter“

verfasst von / submitted by

Michael Schmollngruber BSc MSc

angestrebter akademischer Grad / in partial fulfilment of the requirements for the degree of

Doktor der Naturwissenschaften (Dr. rer. nat.)

Wien, 2016 / Vienna 2016

Studienkennzahl lt. Studienblatt / degree programme code as it appears on the student record sheet:	A 796 605 419
Dissertationsgebiet lt. Studienblatt / field of study as it appears on the student record sheet:	Chemie
Betreut von / Supervisor:	Univ.-Prof. Dr. Othmar Steinhauser
Mitbetreut von / Co-Supervisor:	Ass.-Prof. Dipl.-Chem. Dr. Christian Schröder

Danksagung

Am Institut für Computergestützte Biologische Chemie hatte ich das große Glück, meine Ideen in einer stets unterstützenden und offenen Atmosphäre entwickeln zu können. Ich möchte mich an dieser Stelle bei allen Menschen bedanken, die mich in den letzten Jahren auf meinem Weg begleitet haben.

Besonderer Dank gilt meinem Betreuer Othmar Steinhauser, der mich jederzeit mit einem offenen Ohr empfangen hat, wenn guter Rat vonnöten war. Innerhalb der vielen Stunden, die er sich trotz seiner vielfältigen Verpflichtungen immer für die persönliche Betreuung seiner Studenten frei hält, hat er mir immer mit großer Geduld die komplexen Zusammenhänge erklärt, die unserem Forschungsgebiet zugrunde liegen. Ebenso möchte ich Christian Schröder für die sehr konstruktive Zusammenarbeit danken. Er stand mir jederzeit als hilfsbereiter und kompetenter Ansprechpartner in allen wissenschaftlichen Belangen zur Verfügung. Speziellen Dank richte ich auch an meinen langjährigen Kollegen Daniel Braun. In unseren vielen Diskussionen gelang es uns oft, ein Problem auf das Wesentliche zu reduzieren und so zu einer Lösung zu finden. Nicht zuletzt möchte ich an dieser Stelle auch Stefan Boresch für die Gelegenheit danken, mein Interesse an Linux-Systemen erkunden zu können. Auch in dieser Hinsicht konnte ich am Institut für Computergestützte Biologische Chemie sehr viel Neues lernen.

Meinen ganz persönlichen Dank richte ich auch an meine Lebensgefährtin Denise und an meine Familie, die mich auf dem langen Weg hierher immer bedingungslos unterstützt haben. Es endet für mich an dieser Stelle ein Lebensabschnitt, der mich in vielerlei Hinsicht geprägt hat und an den ich mich auch in Zukunft immer freudig erinnern werde.

Zusammenfassung

Unter dem Überbegriff Spektroskopie versteht man Messungen der Interaktion zwischen Materie und elektromagnetischer Strahlung. In Abhängigkeit der Frequenz der einfallenden Strahlung treten dabei verschiedene Bestandteile der Materie auf charakteristische Weise mit ihr in Resonanz. Spektroskopische Methoden wie zum Beispiel dielektrische Spektroskopie, Terahertzspektroskopie oder der zeitabhängige *Stokes-Shift* messen verschiedene Aspekte der Kernbewegung von Molekülen. Insbesondere erlauben die genannten Methoden das Studium der gekoppelten Bewegung vieler Moleküle und ermöglichen so eine Beschreibung des Verhaltens von kondensierter Materie auf mesoskopischer Ebene.

In dieser Arbeit liegt der Fokus auf dem Studium von sogenannter Weicher Materie. Darunter versteht man kondensierte Materie, die schon bei Raumtemperatur vielfältige dynamische Prozesse auf mikro- und mesoskopischer Ebene aufweist, welche man mittels der oben genannten spektroskopischen Methoden messen kann. Bei der Interpretation spektroskopischer Resultate stellen Computersimulationen der molekularen Dynamik solcher Systeme eine wertvolle Ergänzung zum Experiment dar. Im Experiment betrachtet man stets nur einen Ausschnitt der gesamten vorhandenen Dynamik, während man in Computersimulationen eine große Vielfalt molekularer Dynamik greifbar machen kann.

Computergestützte Spektroskopie stellt die Kombination von Beidem dar, indem man spektroskopische Messgrößen aus der simulierten Moleküldynamik berechnet. Dies erlaubt den direkten Vergleich von aus der Simulationen berechneten Spektren mit experimentellen Resultaten und somit auch eine Validierung der Simulation. Die Simulation kann darüber hinaus verwendet werden, um die spektroskopisch gemessene Dynamik im größeren Kontext der gesamten molekularen Dynamik zu betrachten. Außerdem kann das gemessene Signal mit Hilfe der Simulation zerlegt werden in verschiedene Komponenten des Systems, was eine direkte und tiefgreifende Analyse des Messergebnisses erlaubt.

Die vorliegende Arbeit besteht aus drei Teilen. Im ersten Teil liegt der Fokus auf den dielektrischen Eigenschaften Reverser Mizellen. Darunter versteht man von einem hydrophoben Medium und Detergens umschlossenene Wassertröpfchen in der Größe von Nanometern, welche als Modellsysteme für subzelluläre membranumschlossene Strukturen dienen. Es wird die gesamte mit klassischen Simulation beschreibbare Dynamik des kollektiven Dipolmoments beschrieben und in dielektrische Spektren sowie in Terahertzspektren umgerechnet. Dabei werden reverse Mizellen mit unterschiedlichem Wassergehalt betrachtet. Weiters wird untersucht, wie die Inklusion des Proteins Ubiquitin die dielektrischen Eigenschaften verändert. Im zweiten Teil der Arbeit wird zunächst die Verbindung zwischen dielektrischen Spektren und dem zeitabängigen *Stokes-Shift* in ionischen Flüssigkeiten untersucht. Darauf folgt eine detaillierte Studie zu den molekularen Ursprüngen des zeitabhängigen *Stokes-Shift* in ionischen Flüssigkeiten durch umfangreiche Nichtgleichgewichtssimulationen unter Zuhilfenahme eines vereinfachten *coarse-grained* Modells. Im dritten Teil dieser Dissertation werden zwei methodische Studien präsentiert, die den Einfluss von Polarisierbarkeit auf Struktur und Dynamik ionischer Flüssigkeiten untersuchen. Dabei werden verschiedene Methoden einander direkt gegenüber gestellt.

Abstract

The umbrella term spectroscopy encompasses various kinds of measurements of the interaction between matter and electromagnetic waves. Depending on the latter's frequency, different constituents of physical matter will resonate with the incoming radiation. Spectroscopic methods such as dielectric spektroscopy, terahertz spectroscopy and the time-dependent Stokes shift measure different aspects of nuclear motion. In particular, these methods allow for a description of the coupled motion of many molecules and thus can characterize the behaviour of matter on a mesoscopic level.

In this present work the focus lies on the study of so-called Soft Matter, *i.e.* condensed matter, that already at room temperature exhibits manifold dynamical processes on a microscopic as well as on a mesoscopic level, which are typically described using the abovementioned spectroscopic techniques. In the interpretation of experimental spectroscopic results computer simulations of molecular dynamics are a valuable additional source of information. While experiments can always show only a part of a system's dynamical capacity, computer simulation can make tangible directly the diversity of molecular dynamics.

Computational spectroscopy represents the combination of both, as one calculates spectroscopic observables directly from computer simulations of molecular dynamics. This allows for a direct comparison of computational results to experimental data, which also provides a source of validation for the models used in the simulation. Furthermore, computer simulation can be used to study the origin of the experimentally measured signal in the greater context of the whole dynamics of the system. Additionally, the total signal can often be decomposed into contributions from various components of a system, which allows for an immediate and profound analysis of experimental results.

This work consists of three parts. The first part has its focus on the dielectric properties of reverse micelles. These are nano-scale water droplets surrounded by a detergent and a hydrophobic medium, which can be seen as a model system for sub-cellular membrane-enclosed structures. The whole dynamical range of the collective dipole moment is characterized within the boundaries of classical simulations and transformed into dielectric spectra and terahertz absorption spectra. Reverse micelles with different amounts of water loading are compared. Additionally, the influence of the inclusion of a strongly dipolar biomolecule is studied using the example of the protein ubiquitin. The second part of this work starts out with a study of the connection between dielectric spectra and the time-dependent Stokes shift in ionic liquids. This is followed by a detailed study concerning the molecular origins of the time-dependent Stokes shift in ionic liquids via comprehensive non-equilibrium simulations employing coarse-grained modelling. In the third and last part of this thesis two methodical studies concerning the use of charge polarizability in molecular dynamics simulations of ionic liquids are presented. Two techniques, induced point-dipoles and Drude oscillators, are directly compared in their consequences on structural and dynamical properties. Additionally, the influence of different so-called Thole functions is thoroughly investigated.

Declaration of authorship

In this doctoral thesis I present six related studies on the topics of computational spectroscopy and solvation. Four of them have been published previously in peer-reviewed scientific journals. I am the principal author of three of the published articles and co-author of the fourth. Additionally, two manuscripts recently submitted for publication in peer-reviewed journals are included, of both of which I am the principal author.

[1] M. Schmollngruber, D. Braun, D. Oser and O. Steinhauser
Dielectric depolarisation and concerted collective dynamics in AOT reverse micelles with and without ubiquitin
Phys. Chem. Chem. Phys, **18**, 3606 (2016)

The underlying computer experiments have been designed and carried out together with Daniel Braun. The theory in this work was developed together with my supervisor Othmar Steinhauser. Most of the new analysis software was written by myself, with contributions from Daniel Braun. I am responsible for all the data presented in this work. The resulting paper is presented in Sec. 2.2.

[2] M. Schmollngruber, D. Braun and O. Steinhauser
A computational component analysis of dielectric relaxation and THz spectra of water/AOT reverse micelles with different water loading
submitted to J. Chem. Phys. on 4 October, 2016

The underlying computer experiments have been designed and carried out together with Daniel Braun. The theory in this work was developed together with my supervisor Othmar Steinhauser. All analysis software used in this work I have written myself and I am responsible for all the data presented in this work. The resulting manuscript is presented in Sec. 2.3.

[3] M. Schmollngruber, C. Schröder and O. Steinhauser
Dielectric spectra of ionic liquids and their conversion to solvation dynamics: a detailed computational analysis of polarizable systems
Phys. Chem. Chem. Phys., **16**, 10999 (2014)

The underlying computer experiments have been provided by Christian Schröder. The theory in this work was developed together with my supervisor Othmar Steinhauser. All new analysis software was written by myself and I am responsible for all the data presented in this work. The resulting paper is presented in Sec. 3.2.

[4] M. Schmollngruber, D. Braun and O. Steinhauser
Combining non-equilibrium simulations and coarse-grained modelling allows for a fine-grained decomposition of solvation dynamics
submitted to Phys. Chem. Chem. Phys. on 12 September, 2016

I have designed and carried out all the computer simulations for this work. The coarse-grained model employed here was developed by Daniel Braun. The theory in this work

was developed together with my supervisor Othmar Steinhauser. All analysis software used in this work I have written myself and I am responsible for all the data presented in this work. The resulting manuscript is presented in Sec. 3.3.

[5] T. Taylor, M. Schmollngruber, C. Schröder and O. Steinhauser
The effect of Thole functions on the simulation of ionic liquids with point induced dipoles at various densities
J. Chem. Phys., **138**, 204119 (2013)

The underlying computer experiment have been designed and carried out by Thomas Taylor using the program package AMBER. I have written a special-purpose C++ program to convert the trajectory data from AMBER NetCDF format to CHARMM binary trajectory format to make use of our well-established analysis program GEPETTO. Consequently, I also carried out all data analyses. Christian Schröder and Othmar Steinhauser have developed the theoretical background. The resulting paper is presented in Sec. 4.2.

[6] M. Schmollngruber, V. Lesch, C. Schröder, A. Heuer and O. Steinhauser
Comparing induced point-dipoles and Drude oscillators
Phys. Chem. Chem. Phys, **17**, 14297 (2015)

The underlying computer experiments have been designed and carried out together with Christian Schröder and Volker Lesch. The theory in this work was developed together with my supervisor Othmar Steinhauser. All new analysis software was written by myself and I am responsible for all the data presented in this work. The resulting paper is presented in Sec. 4.3.

Contents

1 Introduction

In this introductory chapter I will provide the reader with a brief overview of the scientific field of computational spectroscopy and the methods employed. Also, I will describe in short the two classes of Soft Matter systems that I have studied in the course of writing this thesis. More detail on the subjects at hand will be given in corresponding later chapters.

1.1 Soft Matter

Soft Matter, such as matter in the liquid state, is characterized by a combination of two properties. First, attractive intermolecular interactions are strong enough to ensure a condensed aggregate state. Second, and what discerns Soft Matter from solids, is that the thermal energy available at room temperature is sufficient for particles to overcome potential energy barriers in the microscopic structure. In other words, a particle is not caught in the cage set up by its neighbors, but rather will escape it solely by means of thermal motion. Both of these characteristic properties taken together lead to complex, highly correlated molecular dynamics on a microscopic as well as on a mesoscopic level.

On a macroscopic level, this lower-level dynamical capacity translates into the bulk deformability, which is the namesake for Soft Matter itself. Apart from that, this plethora of dynamical processes remains invisible to the naked eye. However, as such processes are often accompanied by characteristic changes in electromagnetic properties, certain spectroscopic techniques that measure nuclear motion lend themselves to their study. Often used to study correlated dynamics on a mesoscopic level are dielectric spectroscopy, THz spectroscopy, the time-dependent Stokes shift, and Nuclear Magnetic Resonance spectroscopy. Each of these methods operates within a limited frequency window and thus can observe only dynamical processes in the sample within the corresponding time window. Taken together, however, these techniques cover a broad frequency range of MHz - THz, which is sufficient to cover most of the collective modes of motion in typical liquids.

In this thesis I will present related studies on the dynamical properties of two specific kinds of Soft Matter, both of which are in the liquid state: ionic liquids and reverse micelles. Both substance classes are characterized by unusual structural and dynamical properties related to their respective unique compositions.

1.1.1 Ionic liquids

Ionic liquids (IL) are a class of organic solvents consisting solely of ions and exist in a liquid state at room temperature.[1,2] In distinction to conventional molten salts consisting of small

Property	Organic solvents	Ionic liquids
Number of solvents	> 1000	> 1000000
Applicability	Single function	Multifunction
Catalytic ability	Rare	Common and tuneable
Chirality	Rare	Common and tuneable
Vapour pressure	Obeys the Clausius-Clapeyron equation	Negligible vapour pressure under normal conditions
Flammability	Usually flammable	Usually nonflammable
Solvation	Weakly solvating	Strongly solvating
Polarity	Conventional polarity concepts apply	Polarity concept questionable
Tuneability	Limited range of solvents available	Virtually unlimited range means "designer solvents"
Cost	Normally cheap	Typically between 2 and 100 times the cost of organic solvents
Recyclability	Green imperative	economic imperative
Viscosity [cP]	0.2 - 100	22 - 40000
Density [g cm^{-3}]	0.6 - 1.7	0.8 - 3.3
Refractive index	1.3 - 1.6	1.5 - 2.2

Table 1.1 A comparison of conventional organic solvents and ionic liquids reproduced from Plechkova and Seddon [1].

molecules or atoms, the formation of a stable crystal lattice at standard conditions is hindered by anisotropy of both, molecular shape as well as molecular charge distribution. However, the presence of net molecular charges still leads to strong intermolecular electrostatic interactions, resulting in highly coupled molecular dynamics and sophisticated structural features. Another consequence of the presence of ions with the ability to diffuse freely is that IL conduct electric current. Taken together, this unique set of properties not only opens up many possible applications of IL, but also makes them interesting for fundamental research into their peculiar form of the liquid state.

Physical and chemical properties of IL can be modified in a multitude of ways, e.g. by adapting the length of alkyl side chains, exchanging cations or anions, or adding co-solvents such as water. It is due to the great flexibility of IL that they have come to be considered "designer solvents",[1,2] *i.e.* solvents highly optimized to specific tasks. In comparison to conventional organic solvents many IL have some advantages that are of special interest in the development of new technologies, with a short overview being shown in Tab. 1.1, reproduced from Plechkova and Seddon [1]. Based on their unique properties IL have found many applications, e.g. as specialized reaction media with catalytic function,[3] or as highly efficient media for extracting substances from organic material.[4]

To fully utilize the potential IL undoubtedly have as solvents, a better understanding of their characteristic properties on a molecular level is of importance. In Chapter 3 two studies are presented, which elucidate solute-solvent interactions in IL. On the other hand, in the two studies presented in Chapter 4 a selected IL was chosen as a model system due to the complex electrostatic properties of IL. Based on this system, the influence of adding models of atomic charge polarizability in molecular dynamics simulations is thoroughly investigated.

1.1.2 Reverse micelles

Reverse micelles (RM) are water-in-oil micro-emulsions, where nanometer-scale water droplets are surrounded by a surfactant, and engulfed by a non-polar medium. The surfactant molecules are oriented in such a way that their polar or ionic head groups are oriented towards the water molecules inside the RM. Fig. 1.1 shows a graphic illustration of a RM,

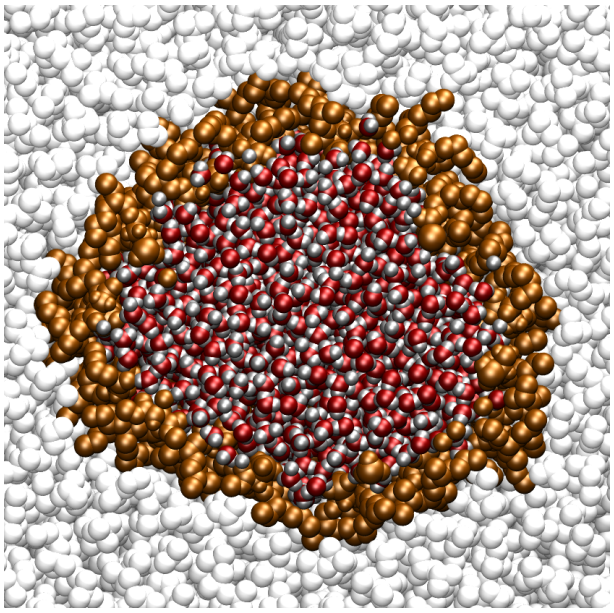

Figure 1.1 Intersection of an AOT/water reverse micelle made from data used in Chapter 2. The water pool in the center is surrounded by the surfactant AOT (shown in orange) and isooctane (shown in white).

which is taken from one of the simulations used for the studies presented in Chapter 2. RM are often seen as model systems for sub-cellular membrane-enclosed compartments, as in both cases small water pools are confined in limited space by a surfactant. Water as well as solvated biomolecules inside a RM have exhibited peculiar behaviour in comparison to bulk solutions. Encapsulation of proteins has been shown to increase protein folding stability through a limitation of available space, which favors folded conformations.[5] The choice of surfactant is of consequence, too. Most often used in studies of RM is sodium bis(2-ethylhexyl) sulfosuccinate, also known as Aerosol-OT, or AOT in short. Due to its anionic head group, AOT has recently been shown to cause denaturation of many enclosed proteins and a replacement by a combination of non-ionic detergents was suggested.[6] Additionally, AOT has been shown to cause strong retardation in the single-particle dynamics of water molecules near the water/AOT interface.[7]

In Chapter 2 two studies on collective electrostatic properties of AOT RM as a whole are presented. As the surrounding non-polar medium does not significantly contribute to the electrostatic properties of the system, one can observe the dynamics of the RM alone by using spectroscopy. The two studies in Chapter 2 focus on dielectric relaxation and THz spectra of AOT RM, where experimental spectra are available in the literature.[8–15] Both studies aim to exploit the strengths of computer simulations of molecular dynamics to provide new insights for the interpretation of spectral data of RM.

1.2 Molecular dynamics simulation

For computational studies on the physico-chemical properties of large soft matter systems, classical molecular dynamics (MD) simulation is the method of choice.[16] In MD simulations

the time evolution of an ensemble of atoms is simulated within the framework of a classical mechanical description. In this way, a system of N atoms is defined by the set of atomic coordinates

$$\vec{r} = (\vec{r}_1, \vec{r}_2, \ldots, \vec{r}_N) \tag{1.1}$$

and momenta

$$\vec{p} = (\vec{p}_1, \vec{p}_2, \ldots, \vec{p}_N). \tag{1.2}$$

Here, each $\vec{r}_i$ is the set of cartesian coordinates of particle i and $\vec{p}_i = m_i \vec{v}_i$ is the momentum of particle i with mass m_i and velocity $\vec{v}_i$. Using these quantities, the Hamiltonian $\mathscr{H}$ of this system, *i.e.* its total energy function, can be expressed as

$$\mathscr{H}(\vec{r}, \vec{p}) = \mathscr{K}(\vec{p}) + \mathscr{U}(\vec{r}), \tag{1.3}$$

where $\mathscr{K}(\vec{p})$ is the total kinetic energy and $\mathscr{U}(\vec{r})$ is the total potential energy. The kinetic energy is usually written as

$$\mathscr{K}(\vec{p}) = \sum_{i=1}^{N} \frac{\vec{p}_i^2}{2m_i}. \tag{1.4}$$

The energy of a structural conformation of the system is given by the potential energy function, which describes all atomic interactions in the system.[16] In classical MD simulations, the potential energy is usually calculated by a set of empirical potential functions, which traditionally is called the force field. These empirical potential functions are designed to model effective quantum-mechanical interactions in a simplified form. This allows for the simulation of the large molecular samples needed to properly study the behaviour of soft matter.[17] The actual functional form of the force field varies between the many software packages available. In recent versions of CHARMM, the MD simulation program mainly used in this work, the potential energy function is implemented as[18]

$$\begin{aligned}
\mathscr{U}(\vec{r}) = & \sum_{\text{bonds}} K_b (b - b_0)^2 + \sum_{\text{angles}} K_\theta (\theta - \theta_0)^2 + \sum_{\text{Urey-Bradley}} K_{UB} (S - S_0)^2 \\
& + \sum_{\text{dihedrals}} K_\phi (1 + \cos(n\phi - \delta)) + \sum_{\text{impropers}} K_\omega (\omega - \omega_0)^2 \\
& + \sum_{\text{non-bonded pairs}} \left\{ \varepsilon_{ij}^{\min} \left[\left(\frac{R_{ij}^{\min}}{r_{ij}} \right)^{12} - 2 \left(\frac{R_{ij}^{\min}}{r_{ij}} \right)^{6} \right] + \frac{q_i q_j}{4\pi\varepsilon_0 \varepsilon r_{ij}} \right\}.
\end{aligned} \tag{1.5}$$

Bonded interactions in this force field include all intramolecular bond, angle and dihedral potentials. Non-bonded interactions are described by two energy functions: the Lennard-Jones 6-12 potential, which models both the strong repulsive forces between atoms at very short distances and attractive van der Waals interactions at longer distances; the Coulomb energy term describes electrostatic interactions between atoms. Please refer to Brooks *et al.* [18] for a complete description of the CHARMM force field.

Having set a potential energy function $\mathscr{U}(\vec{r})$ and providing a set of atomic coordinates $\vec{r}(t)$ and momenta $\vec{p}(t)$ at a given time t, one can solve the classical equations of motion to propagate the system by a discrete time step Δt to the time $t + \Delta t$. The time series of coordinates

and velocities obtained by repeating this processes many times characterize the structure and the dynamics of the molecular ensemble and can be used to compute a multitude of physico-chemical properties.

Where experimental methods often yield results, which are difficult to interpret on a molecular level, MD simulation can provide direct insight into the molecular mechanics of a system. However, the quality of simulation results always depends on the force field in use. Thus, simulation results have to be validated by computing an observable obtainable by experiment and comparing computational and experimental results. Computational spectroscopy provides such a route for validation by allowing for a direct comparison of computed spectra to experimental data.

1.2.1 Polarizability models

Classical MD simulation by design cannot account for electronic degrees of freedom, as the electron density around each atom i is modeled by a fixed point charge q_i reflecting the electron density around that atom. There have been various attempts to mimic electronic degrees of freedom by introducing some kind of flexibility to the charge distribution. Such models of atomic polarizability allow the charge distribution to quickly react to changes in the local environment, even before any nuclear motion occurs. As spectroscopy measures the interaction between matter and electromagnetic fields, including such fast degrees of freedom in computer simulations of spectroscopic properties is paramount for bringing simulation results closer to experiment.[19]

Several methods of modeling polarizability have been implemented. In the Drude oscillator model,[20–26] atomic polarizability is achieved by introducing a pair of virtual, oppositely charged Drude particles for each atom. One of the particles is united with the corresponding atom, while the other is tethered to the atom via a flexible bond. The pair of particles forms an electric dipole, the direction of which is changed by rotation of the tethered particle around the atom and its magnitude is determined by adapting the length of the tether. Another widely used model, called the induced point-dipole model,[27–34] adds mathematical dipoles to each atomic site. This does not require the addition of any virtual particles to the simulation. However, the treatment of electrostatics is more complex, as charge-dipole and dipole-dipole interactions need to be considered. A third often-used method to introduce electronic polarizability is the fluctuating charge model,[35–42] which allows for partial charge transfer between atoms inside a molecule. This approach comes with the downside that the polarization is limited to the molecular geometry, whereas Drude particles and inducible point-dipoles can also realize out-of-plane polarization in planar molecules, for example.

The addition of polarization forces to classical MD simulations comes at the cost of greatly increased computational effort, which is not only caused by more particles or more complex energy functions. Including atomic polarizability in many-particle simulations breaks the additivity of the classical force field shown in Eq. 1.5. Instead, non-additive polarization forces have to be computed for all particles at once by either a self-consistent field approach or, alternatively, using a Lagrangian formalism.[20] This procedure has to be repeated at every

time step of the simulation, which also adds to the computational cost.

The two studies presented in Chapter 4 address the question, which of the available polarizability models is best suited for mimicking electronic degrees of freedom in classical MD simulations. Two such models - Drude oscillators and induced point-dipoles - will be discussed and compared in detail in Sec. 4.3. In the presented publication, the influence of polarizability on the structure and dynamics of the ionic liquid 1-ethyl-3-methylimidazolium triflate is studied systematically. As an ionic liquid is characterized by complex and strong electrostatic interactions, 1-ethyl-3-methylimidazolium triflate was chosen as an ideal model system for studying polarizability models.

The implementation of such polarizability models also brings along unwanted side-effects, such as unphysical behaviour of induced dipoles at short distances. This can be mitigated by the introduction of so-called Thole functions,[43] which dampen short-range dipolar interactions. Several such functions have been suggested by Thole. In Sec. 4.2 a thorough analysis of the effect different Thole functions have on simulations with induced point-dipoles is presented.

1.3 Computational spectroscopy

Spectroscopy as an umbrella term describes various experimental techniques that study the interaction between electromagnetic radiation and physical matter. Depending on the frequency of the radiation, different resonance phenomena can be observed. This work focuses on the study of soft matter, the characteristics of which stem from complex molecular dynamics. Experimental spectroscopic studies of such processes require a frequency window, where many-particle modes of motion can be observed, which is typically ranging from Megahertz to Terahertz. Often used methods are dielectric relaxation spectroscopy (DRS) and THz spectroscopy, which is also known as far infrared (FIR) spectroscopy. Both of these methods measure relaxation processes of the collective dipole moment of a sample. Another method that can be used to study the relaxation behaviour of a solvent is the time-dependent Stokes shift (TDSS).

Common to all the aforementioned techniques is that in the theoretical description of the molecular mechanics involved, quantum effects can be neglected. In fact, all these spectroscopic methods can be studied using classical molecular dynamics simulations, which omit quantum chemical detail in exchange for larger system sizes and longer simulated times.

1.3.1 Dielectric relaxation spectroscopy

Dielectric relaxation spectroscopy measures the response of physical matter to an applied oscillating electric field. This response is usually called the frequency-dependent dielectric permittivity $\varepsilon(\omega)$, which relates the local electric field $\vec{E}(\omega)$, *i.e.* the Maxwell field, to the induced collective polarization $\vec{P}(\omega)$ of the sample via the constitutive relation

$$\vec{P}(\omega) = \frac{\varepsilon(\omega) - 1}{4\pi} \vec{E}(\omega). \tag{1.6}$$

The polarization is related to the dipole density via

$$\vec{P} = \frac{\vec{M}}{V}, \tag{1.7}$$

where $\vec{M}$ is the collective dipole moment of the sample and V is the sample volume. In this way, DRS measures how susceptible a sample of matter is to the induction of an electric dipole moment by an externally applied electric field at a given frequency ω.

Depending on the properties of the sample this dipole moment can arise through different mechanisms. This is especially valid for ionic liquids, where each molecule carries a net charge as well as an electric dipole moment.[44] In that case, polarization can occur through (i) the collective alignment of molecular dipoles, (ii) the intermolecular dipole arising from a non-isotropic distribution of ions or (iii) the polarization of the electron cloud of an atom or molecule. Classical MD simulations can be used without modification to model the first two kinds of polarization, while electronic polarizability can only be modeled by one of the aforementioned atomic polarizability models (cf. Sec. 1.2.1).

In the THz region DRS is related to THz spectroscopy. The frequency-dependent dielectric permittivity $\varepsilon(\omega)$ can be converted to the molar extinction coefficient $\varepsilon_m(\bar{\nu})$ recorded in THz spectra, as shown in Sec. 2.2.4. In this way, collective librational modes of motion of the sample can be compared to experimental data.[15]

Simulation studies can be a valuable tool in decomposing a complex observable into various contributions and thus facilitating interpretation. Besides decomposing different kinds of polarization and different mechanisms of relaxation[44] a species-wise decomposition is also possible. The two studies presented in Chapter 2 explore different ways to decompose dielectric relaxation spectra as well as THz spectra of reverse micelles.

1.3.2 Time-dependent Stokes shift

The time-dependent Stokes shift (TDSS) is observed as the itinerant shift of a fluorescence peak maximum. This method utilizes a solvated chromophore as a probe for the dynamical changes of the surrounding solvent molecules after electronic excitation of the chromophore. Solvent molecules react to the perturbation caused by the change of the electronic charge distribution of the solute by reorganizing until a more energetically favorable structure is reached.

In an experimental setup the normalized TDSS is given by

$$S(t) = \frac{\nu(t) - \nu(\infty)}{\nu(0) - \nu(\infty)}, \tag{1.8}$$

describing the time-dependent shift of the peak frequency $\nu(t)$ observed in the fluorescence spectrum from its initial value $\nu(0)$ to the asymptotic value $\nu(\infty)$.[45] As shown in Sec. 3.3.2, the time dependence of $\nu(t)$ can be approximated to stem entirely from changes in the solva-

tion energy difference $\Delta U(t) = U_{S_1}(t) - U_{S_0}(t)$, allowing for Eq. 1.8 to be rewritten as

$$S(t) = \frac{\overline{\Delta U(t)} - \overline{\Delta U(\infty)}}{\overline{\Delta U(0)} - \overline{\Delta U(\infty)}}. \tag{1.9}$$

Here, S_0 and S_1 refer to the ground and the first excited electronic states, respectively. The overbars in this equation denote the ensemble average, *i.e.* the average $\Delta U(t)$ each chromophore molecule in the sample has at time t after the electronic excitation occured.

In non-equilibrium MD simulations one can mirror the experimental situation by simulating the relaxation processes occurring in a solvent after an instantaneous change of the charge distribution of an embedded chromophore. The ensemble average in Eq. 1.9 is obtained by taking into account many independent simulations of the relaxation process. First, each of these replica simulations is in equilibrium for the S_0 state of the solute. At this point, the charge distribution of the solute is changed to correspond to the S_1 state and the simulations are continued until the new equilibrium for the S_1 state is reached. Each one of these independent replica simulations represents a different point in the S_0 phase space. A large number of simulations is necessary to get a reliable statistical average over all the different microscopic solvation states that the large number of chromophore molecules in an experimental measurement can experience at the time of the electronic excitation. As this method directly simulates the relaxation process of the solvent, it also provides immediate insight into its underlying molecular mechanics.

An approach available at less computational cost is to apply linear response theory, whereby one can approximate the TDSS from simulations of a molecular system in thermodynamic equilibrium for either the S_0 or the S_1 state. The formalism relates the TDSS to the time correlation function of the fluctuations of the solvation energy via

$$S(t) \approx C(t) = \frac{\langle \delta\Delta U(0)\delta\Delta U(t)\rangle}{\langle \delta\Delta U(0)^2\rangle}, \tag{1.10}$$

where

$$\delta\Delta U(t) = \Delta U(t) - \langle \Delta U\rangle \tag{1.11}$$

are the fluctuations of the solvation energy.

Chapter 3 consists of two studies of the TDSS in ionic liquids. In Sec. 3.2 the connection between the time-dependent Stokes shift and dielectric relaxation spectroscopy is explored. This connection is given by a reaction field continuum model well established for polar solvents. It is shown that in ionic liquids, electric conductivity is the main reason why the reaction field continuum model predicts too fast relaxation times. The manuscript presented in Sec. 3.3 explores how non-equilibrium simulations can be used to decompose the TDSS. In combination with a large number of replica simulations made possible by the usage of a coarse-grained model of the solvent, a fine-grained decomposition of contributions to the TDSS down to individual solute atoms can be realized.

2 Collective dipolar relaxation in water/AOT reverse micelles

2.1 Overview

Reverse micelles (RM) have very peculiar electrostatic properties. Each RM consists of a small droplet of water, which is surrounded by a monolayer of surfactant molecules. As a whole, such a RM has to blend in with the surrounding apolar medium. A collection of water molecules typically exhibits a collective dipole moment reflecting the molecular structural arrangement of the system.[46–48] This raises the question how the RM as a whole manages to minimize its polarity in spite of the strongly polar medium water it contains.

The publication presented in Sec. 2.2 investigates this question for the case of a water / AOT / isooctane RM. Additionally, the study elucidates how such a RM behaves upon inclusion of the polar protein ubiquitin, further adding to the complexity of the system. A detailed component analysis is performed, which allows for a deeper understanding of the peculiar composition of the collective electric dipole moment of a RM.

In Sec. 2.3 a manuscript recently submitted for publication is presented, which extends the analysis of the dielectric relaxation behaviour of RM to different amounts of water loading. This is measured by the $[H_2O]/[AOT]$ concentration ratio, which is usually called w_0. This parameter affects the average water content per RM, as well as the average total size of a RM. A comparative study of three RM systems at representative values of w_0 is presented, which includes a decomposition of dielectric relaxation and THz spectra by molecular species as well as water solvation shells. Furthermore, a mechanism to describe the rotational diffusion of a non-rigid body such as a RM is developed. A formalism is outlined, which allows for a disentangling of the two possible dipolar relaxation pathways: relaxation by micellar tumbling and relaxation by internal reorganization.

2.2 Dielectric depolarisation and concerted collective dynamics in AOT reverse micelles with and without ubiquitin

Phys. Chem. Chem. Phys., **18**, *3606 (2016)*

Michael Schmollngruber,[a] Daniel Braun,[a] Daniel Oser[a] and Othmar Steinhauser[a]

[a] *University of Vienna, Department of Computational Biological Chemistry, Währingerstrasse 17, A-1090 Vienna, Austria*

In this computational study we present molecular dynamics (MD) simulations of reverse micelles, *i.e.* nano-scale water pools encapsulated by sodium bis(2-ethylhexyl) sulfosuccinate (AOT) and dissolved in isooctane. Although consisting of highly polar components, such micro-emulsions exhibit surprisingly low dielectric permittivity, both static and frequency-dependent. This finding is well supported by experimental dielectric measurements. Furthermore, the computational dielectric spectra of reverse micelles with and without the polar protein ubiquitin are almost identical. A detailed component analysis of our simulated systems reveals the underlying mechanism of the observed dielectric depolarisation. While each component by itself would make a remarkable contribution to the static dielectric permittivity, mutual compensation leads to the observed marginal net result. This compensatory behavior is maintained for all but the highest frequencies. Dielectric model theory adapted to the peculiarities of reverse micelles provides an explanation: embedding a system in a cavity engulfed by a low dielectric medium automatically leads to depolarization. In this sense experiment, simulation and theory are in accordance.

2.2.1 Introduction

Reverse micelles are simple model systems to emulate the behavior of biomolecules in a confined environment resembling cellular structures. Such micro-emulsions composed of sodium bis(2-ethylhexyl) sulfosuccinate (AOT), water and an alkane (such as isooctane) create small nano-scale water pools that are enclosed by a membrane-like interface and dissolved in a low dielectric medium.

Several studies exist investigating the influence of confinement on biomolecules using reverse micelles as model systems. Confinement and molecular crowding have been compared.[49] Both have been shown to favour protein folding[5] as a consequence of excluded volume effects. Stabilizing effects on alpha-helical oligopeptides[50] and RNA oligomers[51] as well as increased rigidity of the backbone structure of ubiquitin[52] have been reported, too. Decreased hydration as a consequence of confinement in reverse micelles was found to be an additional driving force of biomolecular stability.[53–55] In contrast, deviations from the native structure of cytochrome c possibly leading to protein unfolding have also been reported.[56] Reverse micelles have also been used as a tool in developing novel protein NMR techniques.[57,58] NMR studies have shown that the structure of ubiquitin is faithfully conserved in AOT reverse micelles.[59,60] However, this is not generally the case, as AOT often acts as a denaturating agent on proteins.[61] As a consequence, novel surfactants were developed avoiding this deficiency.[6]

Another widely investigated subject is the influence of confinement within reverse micelles on molecular dynamics, and in particular on water dynamics. Beginning with the seminal work of Faeder and Ladanyi,[62] a series of simulation studies has been reported. Structure and dynamics have been studied starting from pre-aggregated reverse micelles.[9,62–67] The process of self-aggregation has also been investigated.[52,55,68–70] To cope with the large system sizes many of these studies used coarse-grained models.[9,62,64,65,67,69–71] The dynamics of reverse micelles has been studied by spectroscopic means both experimentally and computationally on a wide frequency range, including nuclear quadrupole relaxation[72], dielectric measurements[10–15,73], terahertz spectroscopy[8,9,15] and infrared spectroscopy.[74–76] These were supplemented by studies concerning the size, morphology and viscosity of reverse micelles.[69,70,77] As a common feature concerning single-molecule or high-frequency (THz) collective water dynamics within reverse micelles it was found that water molecules at the water/AOT interface are dynamically retarded.[9,62,72,74]

Reverse micelles are characterized by a complex interplay of hydrophobic and hydrophilic interactions. While the former are globally described by volume effects and a low dielectric permittivity, the latter are intrinsically connected to substantial electrostatic interactions and are associated with a high dielectric permittivity. Although such micro-emulsions contain significant amounts of polar solvents like water, the overall dielectric permittivity is surprisingly low,[10–14,73] indicating a substantial depolarisation. We now try to elucidate the mechanisms underlying this phenomenon by a series of molecular dynamics (MD) simulations interpreted both at the atomistic as well as at the mesoscopic dielectric level. In a second step, we try to analyze the additional influence of a biomolecule encapsulated within a reverse micelle,

System	# Replica	Length	Write freq.	Box length
RM/UBQ	10	450 ns	1 ps	112.7 Å
RM/UBQ	50	20 ps	0.2 fs	112.7 Å
RM	3	100 ns	50 fs	112.875 Å
RM	30	20 ps	0.2 fs	112.875 Å
H_2O/UBQ	5	100 ns	1 ps	110.9 Å
H_2O/UBQ	30	20 ps	0.2 fs	110.9 Å
H_2O	1	10 ns	2 fs	56.506 Å
H_2O	10	100 ps	0.2 fs	56.506 Å

System	ubiquitin	H_2O	NaCl	AOT	isooctane
RM/UBQ	1	1500	5	100	4500
RM	-	1800	6	100	4500
H_2O/UBQ	1	45000	150	-	-
H_2O	-	6000	20	-	-

Table 2.1 Overview of the simulations performed for this study. The upper part of the table lists the number of independent replica simulations, the length of the NVT simulations after equilibration, the write frequency in each trajectory and the respective box length. The lower part of the table outlines the composition of each system.

taking ubiquitin (UBQ) as an example. In our analysis we treat our reverse micelle as a super-molecule dissolved in a low dielectric medium and consisting of electrostatically neutral sub-components, namely water, ions and - if present - ubiquitin. This component analysis allows for a deeper understanding of the inherent depolarisation observed in the static as well as in the frequency-dependent dielectric permittivity.

The rest of the paper is organized as follows: we first present the methodological details of our computational study concerning the composition of our systems, the force fields employed and the software used. Results and discussion are subdivided into static and dynamic dielectric properties, which are compared to experimental results available and interpreted on the basis of dielectric model theory.

2.2.2 Methods

This work is based on Molecular Dynamics (MD) simulations of the following systems. We have simulated reverse micelles in isooctane using the surfactant sodium bis(2-ethylhexyl) sulfosuccinate, also known as Aerosol-OT (AOT). Simulations were made for reverse micelles both with and without the protein ubiquitin (UBQ) enclosed (abbreviated RM/UBQ and RM, respectively). Additionally, corresponding water systems without the confinement of a reverse micelle were studied as reference (abbreviated H_2O/UBQ and H_2O). Tab. 2.1 shows an overview of the simulations performed for this work. Instead of pure water we used an aquaeous NaCl solution both in the reverse micelle simulations as well as in the reference simulations without confinement. The ratio of the number of water molecules to the number of NaCl ion pairs (300:1, 0.185 M) was chosen to correspond roughly to physi-

ological osmolarity. The ratio of concentrations $w_0 = [H_2O]/[AOT]$ was chosen to be 15 for the RM/UBQ system. For the RM system ubiquitin was replaced by 300 water molecules to retain the size of the micelle, leading to $w_0 = 18$.

All simulations were carried out with DOMDEC CHARMM[18,78] using the following protocol. First the systems were assembled in cubic boxes using PACKMOL.[79] All replica simulations were prepared independently. The reverse micelles were already pre-assembled using PACKMOL. After an energy minimization and a 2 ns equilibration run in an NpT ensemble the box size was set to the average of all replica simulations for each system. Next followed equilibration runs of variable length in an NVT ensemble: RM/UBQ (50 ns), RM (15 ns), H_2O/UBQ (5 ns), H_2O (1 ns). The long equilibration of the RM/UBQ system was necessary because the ubiquitin molecule immediately began to move towards the water/AOT interface of the reverse micelle in all replica simulations. This behavior was reported in previous MD simulations.[52] The total simulation lengths after equilibration are given in Tab. 2.1. The short simulations with high write frequency were run from configurations sampled in the equilibrated long simulations. All simulations were performed with a time step of 2 fs using the leapfrog integrator and periodic boundary conditions. Consequently, electrostatics were calculated using the Particle Mesh Ewald (PME) method[80,81] using cubic splines of order 6 and a κ of 0.41 $Å^{-1}$ to ensure conducting boundary conditions. The PME grid size was adapted to fit the box size of each system: 128x128x128 (RM/UBQ, RM, H_2O/UBQ) and 64x64x64 (H_2O). Non-bonded interactions were calculated using a cut-off at 12Å. All bonds containing hydrogen atoms were kept at constant length using the SHAKE algorithm.[82]

Force field parameters were taken from the following sources: AOT head groups from Abel *et al.*[66]; the SPC/E water model from Berendsen *et al.*[83]; AOT tails and isooctane were modeled using the GROMOS96 united atom force field for aliphatic hydrocarbons in version 45A3;[84] UBQ parameters as well as NaCl parameters were taken from the CHARMM36 force field.[85–88] As a starting structure for the protein we used the 1UBQ structure[89] obtained from the RCSB Protein Data Bank.[90] We decided to use the SPC/E water model instead of TIP3P because recent studies[48,91] have shown that SPC/E is a superior model for the dielectric properties of water. It has been shown in a previous study that the SPC/E water model works well with the force field that we used to model the AOT head groups.[68]

All analyses were performed using a self-written program based on MDAnalysis.[92] Voronoi tessellations were calculated using the Voro++[93] library. It should be noted that for all analyses of the two reverse micelle systems the simulation box was centered to the center-of-mass of the reverse micelle to avoid problems with the periodic boundary conditions.

2.2.3 Results and discussion

Static properties

Collective polarization

The most global characterization of the sample is given by the static dielectric permittivity $\varepsilon(0)$ or susceptibility $\chi(0)$, which is related to the mean square fluctuations of the total dipole

RM/UBQ [a_1]

	H_2O	ions	UBQ	total
H_2O	1.445	-0.383	-1.073	-0.011
ions	-0.383	6.911	-6.420	0.108
UBQ	-1.073	-6.420	7.606	0.113
total	-0.011	0.108	0.113	0.210

RM/UBQ [a_2]

	H_2O	c+u	total
H_2O	1.445	-1.456	-0.011
c+u	-1.456	1.677	0.221
total	-0.011	0.221	0.210

RM [b]

	H_2O	ions	total
H_2O	1.679	-1.678	0.001
ions	-1.678	1.878	0.200
total	0.001	0.200	0.201

H_2O/UBQ [c]

	H_2O	UBQ	total
H_2O	66.5	0.8	67.3
UBQ	0.8	4.7	5.5
total	67.3	5.5	72.8

H_2O [d]

	H_2O
H_2O	64.8

Table 2.2 Table of dielectric susceptibility self- and cross-terms $4\pi\chi_{ij}(0) = \frac{4\pi}{3Vk_BT}\langle\vec{M}_i \cdot \vec{M}_j\rangle$ for all systems. The results are shown component-resolved and as projections onto the total dipole moment $\vec{M}_t$. Sub-tables a_1 and a_2 both show the RM/UBQ system. In the latter, c+u denotes the united component of ions and UBQ. In this way, the similarities between this united component and the ion component of the RM system shown in sub-table b become obvious.

moment $\vec{M}_t$ by

$$\varepsilon(0) - 1 = 4\pi\chi(0) = \frac{4\pi}{3Vk_BT}\langle\vec{M}_t^2\rangle. \tag{2.1}$$

Comparing the values of $\chi(0)$ - given in the lower-right corner of each subtable of Tab. 2.2 - for the reverse micelles with and without UBQ as well as for the respective aquaeous solutions without confinement, two striking features can be found. First, the confinement in a reverse micelle drastically diminishes $\varepsilon(0)$. Second, the additional enclosure of UBQ in the reverse micelle has practically no influence on $\varepsilon(0)$. For further investigation we decompose the total dipole moment

$$\vec{M}_t = \sum_i \vec{M}_i, \tag{2.2}$$

with the $\vec{M}_i$ being the dipole moments of the subsystems water ($\vec{M}_w$), the complete set of ions comprising AOT^-, Na^+ and Cl^- ($\vec{M}_c$) as well as ubiquitin, if present ($\vec{M}_u$). The contribution of the mobile NaCl ions in the unconfined systems H_2O/UBQ and H_2O is marginal and therefore is neglected. As a consequence the total susceptibility is split into pair contributions

$$4\pi\chi_{ij}(0) = \frac{4\pi}{3Vk_BT}\langle\vec{M}_i \cdot \vec{M}_j\rangle. \tag{2.3}$$

The resulting matrix of pair susceptibilities is given in Tab. 2.2. The sum of one row or column gives the net susceptibility of a component. The sum over all component net susceptibilities gives the total susceptibility $\chi(0)$. Comparing the results in Tab. 2.2 for the systems with and without confinement, the most obvious difference concerns the role of the cross-terms χ_{ij}, with $i \neq j$. In the unconfined system H_2O/UBQ the cross-term χ_{wu} makes a small, but positive contribution to the sum of the self-terms $\chi_{ww} + \chi_{uu}$. In confinement the situation changes completely. The cross terms are strictly negative and in magnitude comparable to the self terms. This results in an extremely low total permittivity.

Even more surprisingly, the inclusion of UBQ in the RM leaves the total permittivity almost unchanged. Nevertheless, the self-term χ_{uu} is quite formidable, even exceeding the respective value in the unconfined system. As can be seen from the residue-resolved contributions to the dipole moment of ubiquitin shown in Fig. 2.1, the flexible C-terminus of the protein is the main source of the difference in $\vec{M}_u$, whereas the rest of the protein is more or less structurally conserved. The ionic self-contribution χ_{cc} is of almost the same size as χ_{uu}. However, both self-terms are largely compensated by the respective cross-terms $2\chi_{cu}$. Indeed, the united component of UBQ and ions $\vec{M}_c + \vec{M}_u$ (c+u) shows very much the same behavior as the ions alone in the RM system (cf. Tabs. 2.2a$_2$ and b). Finally, the cross-terms with water further diminish the already small values in both systems. This reveals the extremely compensatory nature of collective dipolar correlations at the mesoscopic level in the confined space of a reverse micelle. In the following section we try to elucidate the mechanism leading to this quenching of the collective polarisation.

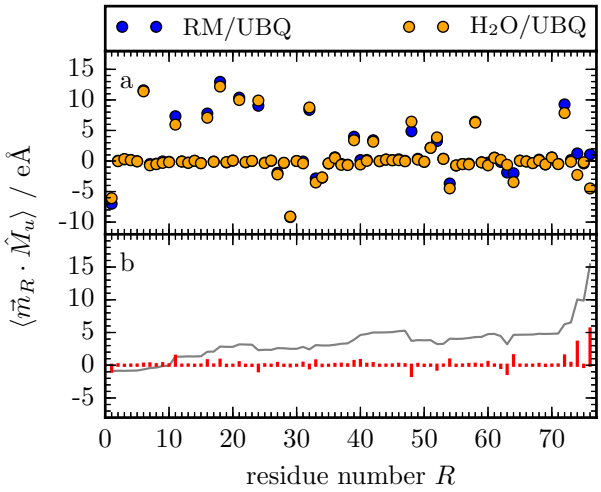

Figure 2.1 Residue-wise contributions to the total protein dipole moment for both the RM/UBQ and the H_2O/UBQ systems. The dipole moment $\vec{\mu}_R$ of each residue r is projected onto the normalized total dipole moment vector of ubiquitin $\hat{M}_u$. The vertical red lines show the differences between the RM/UBQ and the H_2O/UBQ system for each residue. The grey line shows the cumulative sum of the residue-wise dipole moments. The cumulative difference in the dipole moment amounts to about 5 eÅ for the first 71 residues of ubiquitin, while the last five residues raise the total difference to 15 eÅ. This highlights that the residues of the C-terminus make for about two thirds of the total difference.

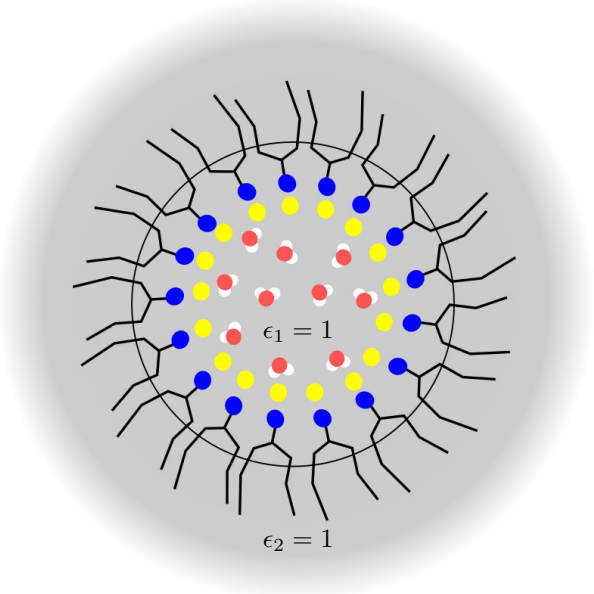

Figure 2.2 Schematic illustration of the dielectric continuum model used to explain our simulation results. The spherical core region contains all water molecules, all Na^+ and Cl^- ions as well as the AOT head groups. By considering the charge distribution within the cavity explicitly, the dielectric constant ε_1 describes only vacuum and is thus set to unity. The outer region is filled with a low dielectric medium described by ε_2. The coarse-grained model used in our simulations even leads to $\varepsilon_2 = 1$.

Theoretical interpretation

For a qualitative discussion of the global dielectric properties of a reverse micelle we start with Gauss' law. In its classical form it reads

$$\int_V div\vec{E}\, dV = \int_A \vec{E}\cdot d\vec{A}, \tag{2.4}$$

where A is the surface area of a closed volume V. As the electric field $\vec{E}$ satisfies the Poisson equation $div\vec{E} = 4\pi\rho(\vec{r})$ the surface integral is equal to the total charge enclosed in the volume. In this classical form Gauss' law says nothing about depolarisation. However, extending the Poisson equation to $div\vec{E} = 4\pi(\rho(\vec{r}) - div\vec{P})$ leads to

$$\int_A \vec{E}\cdot d\vec{A} = -4\pi \int_V div\vec{P}\, dV = -4\pi \int_A \vec{P}\cdot d\vec{A} \tag{2.5}$$

for a neutral charge distribution inside the volume. A reverse micelle, which fulfills this condition, is additionally surrounded by a low dielectric medium with almost no dielectric polarisation. Therefore, a surface that differs from that of the reverse micelle by an infinitesimal thickness δ would give $\int_A \vec{P}\cdot d\vec{A} \approx 0$, meaning that the polarisation on the outer surface of the reverse micelle almost disappears. As a consequence, the extended form of Gauss' law says that the integral over all sources and sinks of dielectric polarisation is minimized. Therefore, the overall compensation of polarisation is in principle predicted by Gauss' law, but only as a law of balance. As it refers to the net polarisation only, Gauss' law provides no information on the interaction mechanisms leading to depolarisation.

For a more detailed analysis we use a dielectric two-zone model describing a spherical cavity of dielectric permittivity ε_1 immersed in an outer dielectric of permittivity ε_2. As can be seen from the idealized view of our system as depicted in Fig. 2.2, the RM system naturally lends itself to such a description. The dielectric model describes the influence of the surroundings on the cavity by a reaction field (RF). In this context we separate the total electrostatic energy U_{tot} of the sample into two parts:

$$U_{tot} = \sum_i \sum_j \frac{q_i q_j}{r_{ij}} + U_{RF}. \tag{2.6}$$

Here, the first term is the pair Coulomb interaction describing the explicit interaction within the charged part of the micelle, *i.e.* inside the cavity, including water and all ions up to the AOT head groups; the implicit interactions with and within the surroundings, comprising the coarse-grained AOT tails and isooctane are given by U_{RF}. Inserting the expression describing the RF in our spherical two-zone model we arrive at

$$U_{tot} = \sum_i \sum_j q_i q_j \left(\frac{1}{r_{ij}} + \frac{1}{2}\, r_{ij}^2\, \frac{\Delta\varepsilon}{\varepsilon_1 + 2\varepsilon_2} \frac{1}{a^3} \right), \tag{2.7}$$

where a is the radius of the spherical cavity. A complete derivation of Eq. 2.7 can be found in the Appendix. It describes the influence of the surroundings on the polarization of the

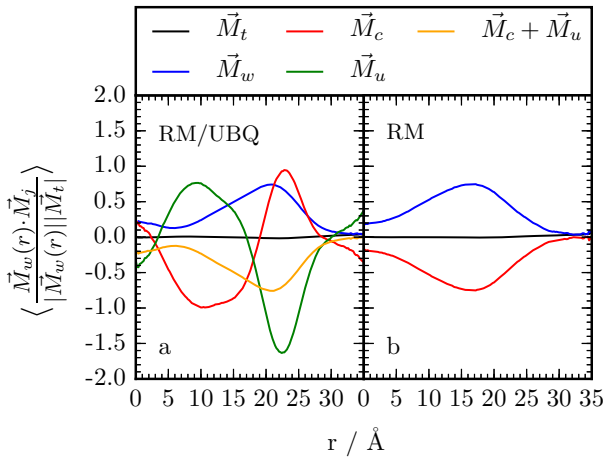

Figure 2.3 Projection of $\hat{M}_w(r)$ onto $\vec{M}_j/|\vec{M}_t|$. $\hat{M}_w(r) = \vec{M}_w(r)/|\vec{M}_w(r)|$ is the normalized sum dipole moment vector of all water molecules within a spherical shell of thickness 0.2Å referred to the center-of-mass of the reverse micelle. $\vec{M}_j/|\vec{M}_t|$ is the dipole moment vector of each component j normalized to the total dipole moment $\vec{M}_t$. The results are shown for both reverse micelle systems.

system by augmenting the pair Coulomb potential $1/r_{ij}$ by the reaction field term which has a distance dependence of $\Delta\varepsilon\, r_{ij}^2$, where $\Delta\varepsilon = \varepsilon_2 - \varepsilon_1$. Seen from the pair Coulomb interaction $(1/r_{ij})$ unlike charges i and j always minimize their distance r_{ij} in order to create the most favourable interaction, thereby reducing polarization. On the other hand, the influence of the surroundings $(\Delta\varepsilon\, r_{ij}^2)$ tries to maximize or minimize the distance between unlike charges depending on the sign of $\Delta\varepsilon$, thus increasing or decreasing polarization. Therefore, pair Coulomb interaction and the reaction field act like antagonists or agonists with respect to the polarization of the system. Treating the complete set of charges within the cavity explicitly corresponds to an inner dielectric permittivity $\varepsilon_1 = 1$. Usually, the outer region is filled by a high dielectric medium such as water and $\Delta\varepsilon \gg 0$. In that case the reaction field is a strong antagonist and counteracts the tendency of the Coulomb pair interaction to minimize polarization. In the case of a reverse micelle, the cavity is surrounded by a low dielectric medium and $\Delta\varepsilon \approx 1$. This means that there is only a small RF acting as an antagonist and the polarization of the cavity is expected to be marginal. In our simulation, the coarse-grained part of the system, *i.e.* the AOT tails and isooctane, entirely lacks charges and therefore we set $\varepsilon_2 = 1$. Consequently, $\Delta\varepsilon = 0$ and the steering influence of the surroundings vanishes completely, whereby the minimization of polarization in the cavity is unhindered. Therefore, this model provides an explanation of the different behavior of confined and unconfined systems as reflected in Tab. 2.2. In a sense the reverse micelle as a whole tries to mimic the hydrophobicity of its surroundings.

Spatial decomposition

The decomposition by species given above is now extended to a spatial decomposition. After confirming by spherical harmonics expansion[94] that our reverse micelles are indeed of almost spherical average shape (data not shown), a subdivison of the collective water dipole moment

into contributions from spherical shells of radius r - referred to the center-of-mass of the reverse micelle - is a natural choice. These $\vec{M}_w(r)$ are normalized to unit vectors. Each of these shell dipole moments is projected onto the net collective dipole moment of each species. The latter are again normalized, but with respect to the total dipole moment $\vec{M}_t$, which is the sum of all species dipole moments. This normalization maintains the additivity of the component projections. The resulting projections are shown in Fig. 2.3.

We first consider the RM system shown in Fig. 2.3b. The projection of the shell dipole moments $\vec{M}_w(r)$ onto the total dipole moment $\vec{M}_t$ (black curve) is almost zero for all r. This leaves two possibilities: either the two vectors are orthogonal for all r or the respective cosine is averaged to zero. The projections onto the component vectors of water and ions clarify this point. As both projections show a variation with r, a strict orthogonal orientation relative to the total dipole moment can be ruled out. Furthermore, as the water and ionic projections are of equal size, but strictly opposite sign, the water and the ion dipole moment vectors must be antiparallel and of almost the same magnitude. Thus, their sum becomes marginal and the orientational correlation with the shell dipole moment is averaged out. This almost perfect compensation of the component dipole moment vectors emphasizes the importance of the cross terms shown in Tab. 2.2b.

The three components of the RM/UBQ system are subject to the same contraint to minimize the total dipole moment. For three vectors this implies that each vector can be expressed by the other two. This is exactly what we see in Fig. 2.3a. Taking the sum of the projections onto ubiquitin and ions, we again get a curve of equal size, but different sign as the projection onto the water component. A constraint on the sum of three vectors already leaves some freedom for their mutual orientation. In fact, the respective projections of $\vec{M}_w(r)$ onto the individual components yields a strong variation as a function of r, including a change in sign.

Although the shell dipole moment $\vec{M}_w(r)$ is always in parallel alignment to its cumulative, asymptotic value $\vec{M}_w$, the degree of alignment drops markedly in the boundary region, *i.e.* at the water-AOT interface. As a result, the contribution of hydration shells closest to the water-AOT interface to the collective water dipole moment becomes marginal. As shown by Chowdhary and Ladanyi,[64] water molecules at the water/AOT interface participating in hydrogen bonds with the oxygen atoms of AOT are pointing away from the center of the reverse micelle. Combined with the average spherical shape of the micelle, a mutual compensation of oppositely oriented, hydrogen-bonded water dipoles would be an explanation of our observation.

In order to test this hypothesis, we now analyze the local water polarization representing the average orientation of a water dipole $\vec{\mu}_i$ with respective center-of-mass coordinates $\vec{r}_i^{\,cm}$ relative to the vector $\vec{r}_i^{\,0} = \vec{r}_i^{\,cm} - \vec{r}_{RM}^{\,cm}$ pointing from the center-of-mass of the reverse micelle to $\vec{r}_i^{\,cm}$. For this aim we use selected g-coefficients - adapted to our situation -

$$g^{000}(r) = \frac{\sum_i \langle \delta(r - r_i^0) \rangle}{4\pi r^2 dr} \frac{1}{\rho} \tag{2.8}$$

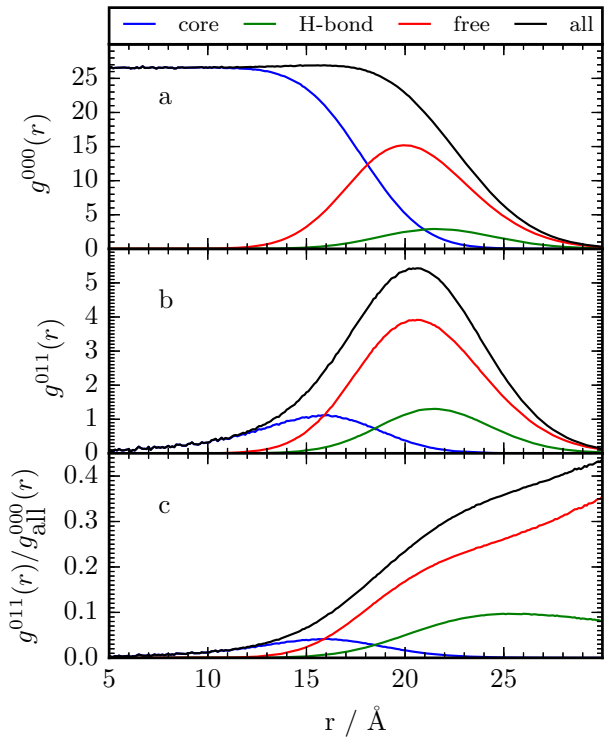

Figure 2.4 Single-particle structure of water in the RM system. Water molecules have been subdivided into three categories, namely core H-bond and free. Panel a shows the radial distribution function of water molecules around the center-of-mass of the reverse micelle. Panel b shows the orientational correlation function of between the dipole moment vector of a water molecule at distance r and the vector pointing from the center-of-mass of the reverse micelle to the center-of-mass of each molecule. Panel c shows the orientational correlation function of each water sub-component normalized to the radial distribution function of the complete set of water molecules.

and

$$g^{011}(r) = \frac{\sum_i \langle cos(\vec{r}_i^{\,0}, \vec{\mu}_i)\delta(r - r_i^0)\rangle}{4\pi r^2 dr}\frac{1}{\rho} \tag{2.9}$$

of the full orientational pair correlation function.[95] $g^{000}(r)$ is the radial distribution function of water molecules around the center-of-mass of the reverse micelle. It shows how the local water density changes as a function of the center-of-mass distance r. $g^{011}(r)$ is the radial distribution function weighted by the average cosine of the angle between the vectors $\vec{r}_i^{\,0}$ and $\vec{\mu}_i$, thereby revealing the average orientation of a water molecule with respect to the center of the reverse micelle. When computing $g^{000}(r)$ and $g^{011}(r)$ the complete set of water molecules was split into three subsets. The "core" subset contains all water molecules not residing in the outermost solvation shell. This shell is defined by Voronoi tessellation[96] as the set of those water molecules having a Delaunay distance of 1 to any AOT molecule. The shell molecules are further subdivided into those which have a hydrogen bond to any AOT oxygen ("H-bond") and those which do not ("free"). Hydrogen bonds are defined in this context as having an O-H distance of less than 2 Å and having an O-H-O bond angle wider than 162°, *i.e.* a cosine less than -0.95. Accordingly we have

$$g^{011}_{\text{all}}(r) = g^{011}_{\text{core}}(r) + g^{011}_{\text{H-bond}}(r) + g^{011}_{\text{free}}(r) \tag{2.10}$$

and an analogous expression for $g^{000}_{\text{all}}(r)$. These g-coefficients are shown in Fig. 2.4a and b for all subsets and are in accordance with similar previous findings of Pomata *et al.*[71]. The $g^{000}(r)$ coefficients shown in Fig. 2.4a provide insights into the shape of the reverse micelle. The broad radial distribution of the outermost shell ("H-bond" and "free" subsets) and their appreciable overlap with the "core" region is indicative of large fluctuations around the average spherical shape of the reverse micelle. Fig. 2.4b shows that the orientational correlation $g^{011}(r)$ is strictly positive in all regions of the reverse micelle with a strong tendency to increase in the outermost shell. Only when the population $g^{000}(r)$ in panel a decreases as a consequence of the finiteness of the reverse micelle, the orientational correlation $g^{011}(r)$ decreases as well. Panel c gives the ratios of all respective terms in Eq. 2.10 to $g^{000}_{\text{all}}(r)$. As can be seen from Eq. 2.9, $g^{011}(r)$ contains the average cosine of the angle between the two vectors multiplied by the population. Thus, the ratio $g^{011}_{\text{all}}(r)/g^{000}_{\text{all}}(r)$ gives the pure distance-dependent averaged cosine of the angle between the vectors $\vec{r}_i^{\,0}$ and $\vec{\mu}_i$. In order to split up the average cosine into contributions from the subsets while maintaining additivity, we compute the ratio of each term in Eq. 2.10 to $g^{000}_{\text{all}}(r)$.

Now, Fig. 2.4c shows a monotonic increase of the average cosine, which can be attributed mainly to the subset of "free" water molecules. This reveals a strong tendency of water dipoles to align parallel with the surface normal. For the "H-bond" waters this is not surprising, because the positively charged hydrogen atoms point towards the AOT oxygen atoms constituting the surface of the reverse micelle.[64] A possible explanation is a local depolarisation at the interface between the reverse micelle interior and the surrounding medium. In other words, interfacial water molecules have a strong tendency to counteract the strong inwards-oriented dipoles formed by negatively charged AOT head groups and Na^+ ions in

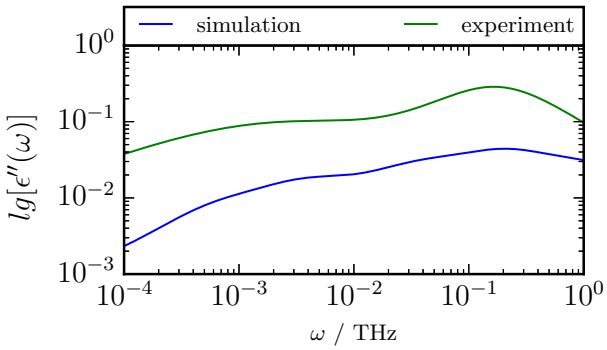

Figure 2.5 A direct comparison of the imaginary parts of experimental[14] and computational dielectric spectra of reverse micelles. Computational data are given for the RM system. As the experimental data shown here were measured for reverse micelles in cyclohexane instead of isooctane we corrected the frequency axis for the difference in viscosities. Data are only shown for the experimentally accessible frequency window.

the vicinity.

Altogether, the static properties discussed above reveal two kinds of collective depolarisation mechanisms in reverse micelles: an inter-species compensation of collective dipole moments as well as a loss of collective water polarisation in the boundary region close to the water/AOT interface.

2.2.4 Dynamics

Dielectric spectra

So far our focus was on the static polarization. Now we extend our analysis to the complete frequency domain ω, thereby analyzing the dynamics of the system on a mesoscopic level. The classic dielectric experiment measures the polarization $\vec{P}(\omega)$ induced in a sample by a frequency-dependent external electric field $\vec{E}_0(\omega)$. For moderately strong electric fields a linear relation holds:

$$\vec{P}(\omega) = \frac{\langle \vec{M}_t(\omega) \rangle}{V} = \chi(\omega)\vec{E}_0(\omega) \tag{2.11}$$

The actual value of the susceptibility $\chi(\omega)$ may depend on the boundary conditions, *i.e.* on the difference between the external field $\vec{E}_0(\omega)$ and the internal Maxwell field $\vec{E}(\omega)$. The constitutive relation

$$\vec{P}(\omega) = \frac{\varepsilon(\omega) - 1}{4\pi}\vec{E}(\omega) \tag{2.12}$$

postulates a unique material property, namely the frequency-dependent permittivity $\varepsilon(\omega)$. It has been shown[97] that for conducting Ewald boundary conditions $\vec{E}(\omega)$ and $\vec{E}_0(\omega)$ are identical leading to $\varepsilon(\omega) - 1 = 4\pi\chi(\omega)$. Applying linear response theory $\varepsilon(\omega)$ is given by

$$\begin{aligned} \varepsilon(\omega) - 1 &= 4\pi\chi(\omega) \\ &= \frac{4\pi}{3Vk_BT}\,\mathscr{L}[-\frac{d}{dt}\langle \vec{M}_{tot}(0)\cdot\vec{M}_{tot}(t)\rangle], \end{aligned} \tag{2.13}$$

where $\mathscr{L}$ denotes the Fourier-Laplace transform. The raw data for $\langle \vec{M}_{tot}(0) \cdot \vec{M}_{tot}(t) \rangle$ derived from simulation were converted to an analytic expression by calculating the best fit to the model function

$$\langle \vec{M}_{tot}(0) \cdot \vec{M}_{tot}(t) \rangle \approx \sum_p A_p e^{-t/\tau_p} + \sum_q A_q e^{-t/\tau_q} cos(\omega_q t + \delta_q). \tag{2.14}$$

To obtain the best fit the following combined approach turned out to be the most successful. The short-time behavior is calculated from short trajectories with a write frequency of 0.2 fs and the long-time behavior is calculated from trajectories with a write frequency of 1 ps (cf. Tab. 2.1). This approach allows us to calculate a detailed fit for the complete relaxation of the collective dipole moment and is applied to all further fit functions shown. As the model function chosen corresponds to an analytical Fourier transform[98] the dielectric spectrum is an analytical function as well. The correlation functions of the reverse micelle systems are quite complex, consisting of up to ten terms (cf. Eq. 2.14). It is due to this complexity that the resulting large number of fit parameters is not given.

Before entering the detailed discussion of our computational spectra we seek to confirm our findings by comparison to experimental data of a similar system. Dielectric measurements for AOT/water reverse micelles in different low dielectric media, namely carbon tetrachloride[10,13] and n-heptane[11,12] exist. Additionally, Balakrishnan[14] made measurements for AOT reverse micelles with the same $w_0 = 18$ as in our RM system and embedded in cyclohexane at a comparable concentration. The experimental spectra have been fitted by the expression

$$\varepsilon(\omega) = \varepsilon_\infty + \frac{\Delta\varepsilon_1}{1 + (i\omega\tau_1)^{1-\alpha}} + \frac{\Delta\varepsilon_2}{1 + i\omega\tau_2} \tag{2.15}$$

with $\varepsilon_\infty = 1.99$, $\Delta\varepsilon_1 = 0.37$, $\tau_1 = 0.41$ ns, $\alpha = 0.41$, $\Delta\varepsilon_2 = 0.53$ and $\tau_2 = 5.8$ ps. The respective viscosity of cyclohexane[99] differs from that of isooctane[100] roughly by a factor of 1:2. The viscosity of the isooctane in our RM system is obtained in the following way. First the rotational diffusion coefficient D_{rot} of the reverse micelle is derived from the angular velocity autocorrelation function. Then the reorientation time $\tau_{rot} = 1/2D_{rot}$ is converted to the viscosity η by the hydrodynamic relation $\tau_{rot} = \frac{3\eta V}{k_B T}$. Coarse-grained systems often show faster dynamics. In our case it was faster by a factor of three. Altogether the dynamics in our simulation is accelerated by a factor of six when compared to the experimental cyclohexane system.[14] This overall faster rotational dynamics of the reverse micelle is reflected in dipolar relaxation times as well. Fig. 2.5 shows a comparison of experimental and computational data after rescaling our frequency axis accordingly. The frequency window is confined to the experimentally accessible values. Although the amplitudes differ by a factor they are very low both in experiment as well as simulation. In fact, the respective static permittivities $\varepsilon(0)$ after subtracting the high-frequency limit ε_∞ are 0.9 and 0.2 (in the case of our non-polarizable simulations ε_∞ has to be set to 1).[101] Moreover, as the dielectric permittivity of the outside medium in experiment is slightly greater than 1, our dielectric theory (cf. Sec. 2.2.3) pre-

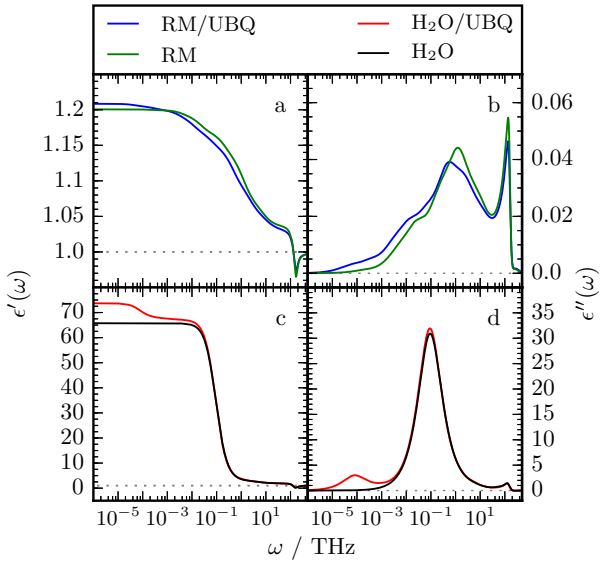

Figure 2.6 Real (left column) and imaginary (right column) parts of the dielectric response of all systems. Panels a and b show the RM and RM/UBQ systems, panels c and d show the H_2O and H_2O/UBQ systems. It should be noted that the THz region shows only those parts of the spectrum that are obtainable via classical MD simulation. The grey dotted line marks $\varepsilon_\infty = 1$ in the real part and zero in the imaginary part.

dicts a weak, but non-vanishing reaction field. As a consequence the depolarisation observed in experiment is not as strong as in our simulation. This comparison shows that the strong compensation of dipolar correlations causing the small computational values of the static dielectric permittivity (cf. Tab. 2.2) is confirmed by experiment. The shape of both spectra is rather similar, with peaks occuring at roughly the same frequencies. Thus, computational and experimental collective dynamics are in qualitative agreement.

The low dielectric properties of the confined RM system are in sharp contrast to the unconfined H_2O system over the whole frequency range accessible by classical MD simulations. This can be seen in Fig. 2.6, giving the real ($\varepsilon'(\omega)$) and imaginary parts ($\varepsilon''(\omega)$) for all simulated systems. It should be noted that in the H_2O/UBQ and H_2O systems the contribution of ion translation and ro-translational coupling to the dielectric spectrum is very small (data not shown) and is therefore omitted entirely in the spectra shown here. The spectrum of the H_2O system shows the dominant water peak at about 100 GHz typical for free water[48] as well as the water libration peak in the THz region. Classical MD simulations of a rigid, non-polarizable water model such as SPC/E can only reproduce the librational band of the experimental THz spectrum of water.[91] It has been shown that the SPC/E model is able to provide a qualitatively correct reproduction of the experimental librational band.[9,91,102,103] Both the GHz signal as well as the water librations prevail in the H_2O/UBQ system with the addition of the typical, concentration-dependent signal of ubiquitin[104] at about 100 MHz, in our case leading to an increment of $\varepsilon(0)$ by 8 (cf. Tab. 2.2). Under confinement, *i.e.* in the reverse micelle, the triadic pattern - the ubiquitin peak at $\approx$ 100 MHz, the dominant water peak at $\approx$ 100 GHz and the water libration THz peak - is changed fundamentally. In the RM system as well as in the RM/UBQ system a complex pattern of overlapping low-amplitude

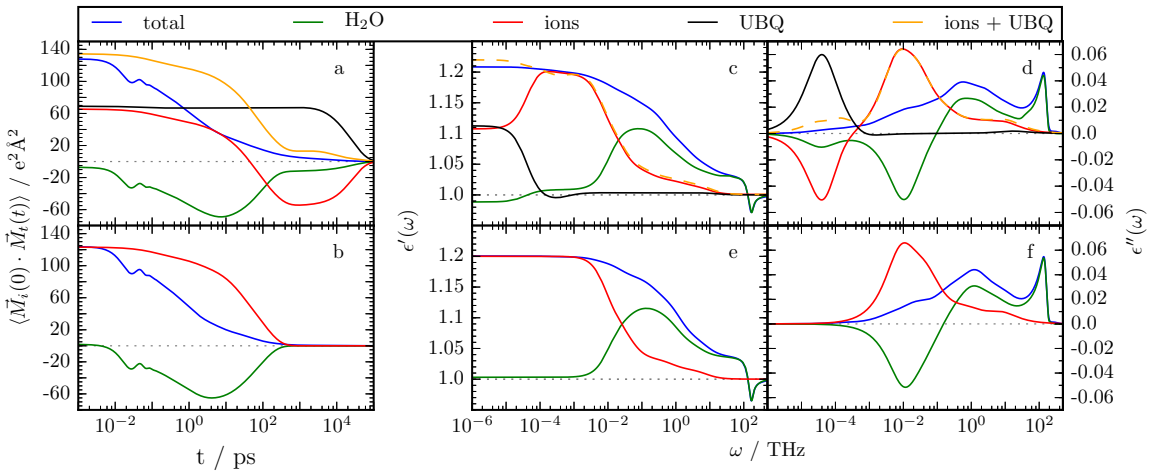

Figure 2.7 Components of the time correlation functions (left column) as well as the real part $\varepsilon'(\omega)$ (middle column) and the imaginary part $\varepsilon''(\omega)$ (right column) of the dielectric permittivity. Panels a, c and d show the RM/UBQ system, panels b, e and f show the RM system. The grey dotted line marks $\varepsilon_\infty = 1$ panels c and e and zero in panels a,b,d and f.

peaks replaces the dominant water peak, Strikingly, the ubiquitin signal of the H_2O/UBQ system seen in Fig. 2.6d is completely absent in the RM/UBQ system seen in Fig. 2.6b. The spectra of the RM and RM/UBQ systems seen in Figs. 2.6a and b are even almost coinciding. The THz region becomes a dominant feature in the dielectric spectrum of the reverse micelle systems. However, it needs a more detailed view and will be discussed in Sec. 2.2.4 after the subsequent component analysis.

Component analysis

From the static component analysis (cf. Tab. 2.2) we have learned that under confinement individual components of the reverse micelle still give remarkable contributions. However these are compensated by equally remarkable cross-terms, leaving only a marginal total result. In order to investigate whether this compensatory behavior is also present in the frequency-dependent permittivity we now decompose the total dipole moment as in Eq. 2.2 leading to component frequency-dependent susceptibilities

$$\chi_i(\omega) = \frac{1}{3Vk_BT}\,\mathscr{L}[-\frac{d}{dt}\langle\vec{M}_i(0)\cdot\vec{M}_t(t)\rangle] \tag{2.16}$$

adding up to the complete susceptibility

$$\chi(\omega) = \sum_i \chi_i(\omega). \tag{2.17}$$

The projection $\langle\vec{M}_i(0)\cdot\vec{M}_t(t)\rangle$ of a single component dipole moment $\vec{M}_i$ onto the total dipole moment $\vec{M}_t$ is in accordance with linear response theory and comprises the respective self-term as well as all cross-terms. The resulting projected correlation functions and the corresponding $\chi_i(\omega)$ spectra for the RM/UBQ and RM systems are shown in Fig. 2.7. The

component correlation functions show clearly that the initial sub-picosecond region, which corresponds to the THz regime in the spectrum, can be almost exclusively attributed to water libration and relaxation. Beyond, the time behavior of the components is highly compensatory, thus suppressing amplitudes in the GHz and MHz regimes. In the RM system the antagonists are water ($\vec{M}_w$) and ions ($\vec{M}_c$). The RM/UBQ system is characterized by a threefold compensation. Again it may be reduced to a two-component system by uniting ubiquitin and ions to a single component, which behaves strikingly similar to the pure ion component in the RM system. Indeed, the small remaining differences can be attributed to couplings between ubiquitin and water. The compensatory behavior in time described above is even more apparent in the imaginary part $\varepsilon''(\omega)$ shown in panels d and f of Fig. 2.7. In the MHz region of the RM/UBQ spectrum the ubiquitin signal is almost perfectly compensated by the ions assisted by water. In the GHz region the ion component dominates, but in its turn it is largely compensated by water. In the THz region the antagonistic behavior of the residual ion component and the water component vanishes leaving essentially the THz spectrum of free water. Since the component contributions beyond the MHz region are almost identical in the RM/UBQ and the RM systems and the ubiquitin signal is quenched, the complete spectra of the two systems are nearly coninciding. This highly compensatory behavior highlights that the dielectric behavior of a reverse micelle is governed by the driving force to minimize its polarization.

THz spectrum

Fig. 2.8a and b show an enlarged view of the real and imaginary parts of the dielectric permittivity, respectively. Owing to the rather different amplitudes the spectra of the systems with and without confinement are shown on separate scales. Not to miss any subtle detail by the fitting procedure the spectra shown in Fig. 2.8 have been calculated by taking the numerical Laplace transform of the respective time correlation functions. These were derived from sets of short simulations calculated with a time step of 0.2 fs (cf. Tab. 2.1). Subsequently, the spectra were smoothed by the Savitzky-Golay algorithm.[105] Apart from the difference in amplitudes, the two sets of spectra (confined and unconfined systems) show a fairly similar dependence on frequency. As we have shown in the previous section, the THz region of the dielectric spectra of the reverse micelles studied here is largely determined by water dynamics. The different amplitudes of confined and unconfined systems thus can be traced back to the difference in water concentrations. As shown previously,[91] pure SPC/E water is able to reproduce the onset of the so-called librational peak of water found in experimental dielectric measurements.[106,107] In the very high frequency THz range one usually measures the molar extinction coefficient $\varepsilon_m(\bar{\nu})$ (not to be confused with dielectric permittivity $\varepsilon(\omega) = \varepsilon'(\omega) + i\varepsilon''(\omega)$) instead of the dielectric spectrum.[8] It is given by $\varepsilon_m(\bar{\nu}) = \alpha(\bar{\nu})/[H_2O]$, with the absorption coefficient

$$\alpha(\omega) = \frac{2\omega}{c} k(\omega). \tag{2.18}$$

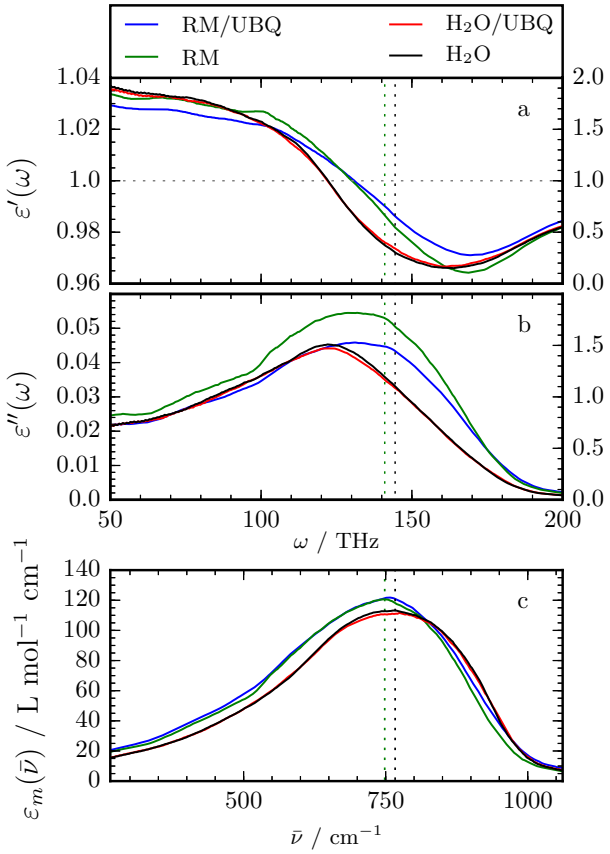

Figure 2.8 THz region. Panels a and b show the real and imaginary parts of the dielectric spectrum, respectively. Panel c shows the molar extinction coefficient in the same frequency window. The vertical dotted lines show the frequencies of the maxima of the molar extinction coefficients of the RM and H_2O systems. In panels a and b the systems RM/UBQ and RM refer to the left y scale, while the systems H_2O/UBQ and H_2O refer to the right y scale. In panel c all curves are on the same scale.

Here, c is the speed of light in vacuum and $k(\omega)$ is the imaginary part of the complex refractive index $\hat{n}(\omega) = n(\omega) + ik(\omega)$. The wave number $\bar{\nu}$ in units of cm^{-1} and the angular frequency ω in units of THz are related by $\bar{\nu} = \omega \frac{33.33}{2\pi}$. Following Wooten[108], $\hat{n}(\omega)$ is related to the dielectric spectrum by

$$k(\omega) = \frac{1}{\sqrt{2}} \sqrt{\sqrt{(\varepsilon'(\omega))^2 + (\varepsilon''(\omega))^2} - \varepsilon'(\omega)}. \tag{2.19}$$

The resulting molar extinction coefficients are shown in Fig. 2.8c. Indeed, calculating $\varepsilon_m(\bar{\nu})$ and thereby scaling the spectra with the respective water concentrations makes the amplitudes of all systems almost identical. In accordance with experimental and computational findings for reverse micelles with $w_0 = 20$ comparable to our RM simulation with $w_0 = 18$,[8,9] we can make the following observation. When comparing the water librations in a reverse micelle of that size to that of bulk water we find that the extinction coefficient is slightly higher for frequencies lower than that of the maximum. Beyond the maximum we observe the opposite. According to Rosenfeld and Schmuttenmaer[9] this retardation is attributed to the different, lower-frequency librational behaviour of water molecules bound to AOT. Fig. 2.8c also reveals that neither with nor without confinement does the presence of ubiquitin have a significant influence on the obtained extinction coefficient.

The observations made from the extinction coefficient seem to contradict those of the imaginary part of the dielectric permittivity, where the signal of confined water is observed at higher frequencies than that of unconfined water. This overlooks, however, that the peak of $\varepsilon''(\omega)$ shown in Fig. 2.8b cannot be traced back to a dynamic process characterized by a single relaxation time, as would be typical for a Lorentzian signal. Rather, it is a superposition of several processes of both oscillatory and relaxing behavior as found in our fitting procedure as well as in experiment.[106,107] Even more important, a direct comparison of the dielectric spectrum and the extinction coefficient is further complicated, as the latter is a mixture of both the real and the imaginary part of the dielectric spectrum (cf. Eq. 2.19). Investigations into the connection between the molecular processes described in terms of fit functions and the results obtained in computational THz spectra are currently underway.

2.2.5 Conclusion

Dielectric properties allow for a description of a molecular system at the mesoscopic level. In this study we analyzed the dielectric permittivity of reverse micelles with and without encapsulated ubiquitin immersed in a low dielectric medium. The most immediate feature, which was found to be in accordance with experiment, was the marginal dielectric constant of such systems, as compared to their unconfined analogues, *i.e.* ionic and protein aquaeous solutions. In order to better understand this depolarisation the dielectric constant was split into species-wise contributions from ions, water and the protein. In fact, the individual component dipole moments still were of remarkable size. However, strong anti-correlations between them diminished the net result.

Not surprisingly, the water/AOT interface plays an important role for the dielectric per-

mittivity. We showed that outside the water core region the natural tendency of water molecules to create large collective dipole moments is impeded by the interaction with AOT. The inwards-pointing dipoles formed by the negatively charged AOT head group and Na^+ induce a favourable outwards-pointing orientation of water dipoles. In combinatioon with the average spherical shape of the reverse micelle the collective water dipole moment of the outer water shell is quenched. In some sense, this quenching at the interface evens out the contrast of a high dielectric medium inside and a low dielectric medium outside the reverse micelle.

The highly compensatory nature of static dielectric properties was also found in the dielectric spectra, *i.e.* on the frequency or time scale. In analogy to the strong spatial coupling of the species-resolved dipole moments, dynamics, *i.e.* dipolar relaxation, of the components turned out to be almost perfectly anti-correlated. Contrary to an aquaeous ubiquitin solution, where the coupling of collective dipolar relaxation of ubiquitin and water was only moderately strong, the reverse micelle was found to enforce concerted collective dynamics of all components. This became visible in the component-resolved spectra, where each agonist found a perfect antagonist. In fact, the main antagonist of ubiquitin in the MHz regime was the ionic component. In turn, their antagonist in the GHz regime was the water component. The classically obtainable THz spectrum was essentially given by water librations, which were found not to have an antagonist. Furthermore, water librations in confinement were quite similar to those of free water for our case of $w_0 = 18$ and unaffected by the presence of ubiquitin.

Seen from the viewpoint of dielectric theory a reverse micelle is a collection of polar molecules embedded in a low dielectric medium. Subdividing any material into two zones automatically poses the question of their interaction. In dielectric theory this interaction is traditionally described by a reaction field. The strength of this reaction field is determined by the difference in dielectric permittivity of the media in the two zones. Adapting a spherical two-zone reaction field model to the case of a reverse micelle, the outer zone is filled by a low dielectric medium and thus creates only a marginal reaction field. In other words, the interaction between inner and outer zone is very weak, *i.e.* the inner zone is electrostatically isolated from its surroundings. In this case dielectric theory predicts a depolarization of the inner zone. Thus, experimental results, our simulations and theory are in accordance. Viewing reverse micelles as model systems for small membrane-enclosed biological systems, this principal finding could be of essential importance for understanding the effects of confinement in the cellular environment.

Acknowledgement

The authors would like to thank Christian Schröder for helpful discussions. Helpful comments from the referees are gratefully acknowledged. This work was funded by the Austrian Science Fund FWF in the context of Project No. P23494 and supported by the Cluster of Excellence RESOLV (EXC 1069) funded by the Deutsche Forschungsgemeinschaft.

2.2.6 Appendix

We consider a spherical cavity of radius a containing an explicit charge distribution $\rho(\vec{r})$ and/or a dielectric medium of permittivity ε_2 embedded in an infinite outer dielectric of permittivity ε_2. The approach used in the following derivations is in parts inspired by Fröhlich [109] and Böttcher. [110] According to the spherical geometry of the cavity, the electrostatic potentials

$$\Phi_1(\vec{r}) = \sum_{l,m}(A_m^l r^l + \frac{B_m^l}{r^{l+1}})Y_m^l(\theta,\phi) \tag{2.20}$$

$$\Phi_2(\vec{r}) = \sum_{l,m}\frac{C_m^l}{r^{l+1}}Y_m^l(\theta,\phi) \tag{2.21}$$

acting in both regions are expanded in spherical harmonics $Y_m^l(\theta,\phi)$. The expansion coefficients have the following meaning: B_m^l represent the multipole moments

$$B_m^l = \int \rho(\vec{r})r^l Y_m^l(\theta,\phi)d\vec{r}. \tag{2.22}$$

of the explicit charge distribution $\rho(\vec{r})$ in the cavity. C_m^l are the residual of the multipole moments B_m^l in the outer region as modified by the boundary conditions

$$\Phi_1(a) = \Phi_2(a) \tag{2.23}$$

$$\varepsilon_1\frac{\partial\Phi_1}{\partial r}(a) = \varepsilon_2\frac{\partial\Phi_2}{\partial r}(a). \tag{2.24}$$

A_m^l stand for the interaction of $\rho(\vec{r})$ with the surrounding outer medium and constitute the reaction potential

$$\Phi_{RF}(\vec{r}) = \sum_{l,m}A_m^l r^l Y_m^{l*}(\theta,\phi). \tag{2.25}$$

Solving the above equations for the expansion coefficients results in

$$A_m^l = -f^l B_m^l \tag{2.26}$$

with the reaction field factor

$$f^l = a^{-(2l+1)}\frac{(\varepsilon_2-\varepsilon_1)(l+1)}{\varepsilon_1 l + \varepsilon_2(l+1)}. \tag{2.27}$$

In the following we consider two special cases.

When taking the complete set of charges within the micelle (cf. Fig. 2.2a), the energy for the interaction of this charge distribution within the cavity and its surroundings is given by

$$U_{RF} = \frac{1}{2}\int \rho(\vec{r})\Phi_{RF}(\vec{r})d\vec{r}. \tag{2.28}$$

Combining Eq. 2.28 with Eqs. 2.25 and 2.26 we get

$$U_{RF} = -\frac{1}{2}\sum_{l,m} f^l B_m^l B_m^{l*}. \tag{2.29}$$

Since charge neutrality $\int \rho(\vec{r})d\vec{r} = 0$ holds for the micelle, the monopole $B_0^0 = 0$. Therefore, the series starts with the dipole moments $B_0^1 = M_{tot}^z$ and $B_{\pm 1}^1 = \frac{1}{\sqrt{2}}(M_{tot}^x \pm iM_{tot}^y)$ and the dominating term in U_s is given by

$$U_{RF} \approx -\frac{1}{2} f^1 \vec{M}_{tot}^2. \tag{2.30}$$

As the sign of $\Delta\varepsilon = \varepsilon_2 - \varepsilon_1$ determines the sign of f^1, U_{RF} becomes most favourable when $\vec{M}_{tot}^2$ is maximized ($\Delta\varepsilon > 0$) or minimized ($\Delta\varepsilon < 0$). Expressing M_{tot} in terms of atomic charges q_i and their positions $\vec{r}_i$, we get

$$M_{tot}^2 = -\frac{1}{2}\sum_i \sum_j q_i q_j (\vec{r}_i - \vec{r}_j)^2 \tag{2.31}$$

for a neutral system. Augmenting the explicit electrostatic interaction energy U_{tot} by the reaction field contribution U_{RF}, we get

$$U_{tot} = \sum_i \sum_j \frac{q_i q_j}{r_{ij}} + U_{RF}. \tag{2.32}$$

Combining Eqs. 2.27, 2.30, 2.31 and 2.32 we arrive at

$$U_{tot} = \sum_i \sum_j q_i q_j \left(\frac{1}{r_{ij}} + \frac{1}{2}\, r_{ij}^2\, \frac{\Delta\varepsilon}{\varepsilon_1 + 2\varepsilon_2} \frac{1}{a^3} \right), \tag{2.33}$$

where the first term is the pair Coulomb interaction, while the second term stems from the reaction field produced by the surroundings.

2.3 A computational component analysis of dielectric relaxation and THz spectra of water/AOT reverse micelles with different water loading

submitted to J. Chem. Phys. on 4 October, 2016

Michael Schmollngruber,[a] Daniel Braun,[a] and Othmar Steinhauser[a]

[a] *University of Vienna, Department of Computational Biological Chemistry, Währingerstrasse 17, A-1090 Vienna, Austria*

In this computational study we present molecular dynamics simulations of water / AOT / isooctane reverse micelles with different water loading. We compare these systems in terms of a detailed analysis of dielectric relaxation spectra and water librations in the THz region. The spectra are decomposed into contributions by molecular species, and contributions from individual water solvation shells. Additionally, micellar tumbling motion is shown to have a profound influence on the observed dielectric relaxation spectra, if relaxation by internal reorganization and micellar tumbling occur within similar time scales. A formalism to directly quantify the effect of micellar tumbling motion on a recorded dielectric spectrum is developed. Since micellar rotational diffusion obeys the laws of hydrodynamics, this method is applicable in an experimental context as well, only knowing the viscosity of the outside medium and the average volume of the reverse micelle.

2.3.1 Introduction

Reverse micelles (RM) are an interesting class of soft matter that serve as model systems of water confinement in a liquid environment. Mediated by the amphiphilic character of a surfactant, nano-scale water pools are enclosed within a hydrophobic medium. In this sense, RM are often treated as mimetics of membrane-enclosed biological systems.[49] Structural and dynamical properties of RM have been studied extensively both experimentally and computationally.[7,9,52,55,62–71,111,112] In particular, spectroscopic methods have been applied to study dynamial properties of RM, among them nuclear quadrupole relaxation[7,72], infrared spectroscopy.[74–76,112,113] and solvation dynamics.[15,114] In this work, we focus on dielectric relaxation spectroscopy (DRS) as well as THz spectroscopy, both of which measure relaxation processes of the collective dipole moment of a sample. In the case of a RM, the surrounding low dielectric medium only marginally contributes to the collective dipole moment. Thus, this technique allows for direct measurements of the dynamics of the RM itself. Only a few previous studies on dielectric properties of RM have been performed[10–15,111]. The same is true for THz spectroscopy.[8,9,15,111]

Of special interest are the peculiarities of the dynamics of confined water as compared to bulk water. It has been shown previously that dynamics is markedly retarded, in particular at the water-surfactant interface.[7,9,15,62,72,74,113] The degree of retardation certainly depends on the volume of the water pool relative to the area of the surface, which is usually quantified by the water/surfactant concentration ratio w_0. Previous experimental works studying the dependence of dielectric properties on water loading[10–13,15] have reported a likewise shift to lower frequencies. It has been shown previously by D'Angelo *et al.*[12] that in RM with low water loading individual AOT molecules can no longer move freely and will thus rotate only with the tumbling motion of the whole RM. The strength of this effect was shown to correlate well with the degree of hydration of individual AOT molecules, which in turn depends on w_0. Thus, at very low water loading an increasing fraction of AOT molecules was shown to relax by micellar tumbling motion, resulting in a frequency shift of the lowest-frequency band in the dielectric spectrum.

In our previous study on the dielectric properties of RM[111] we reported a significant compensation mechanism for a RM with $w_0 = 18$. We performed a decomposition of the total observed dielectric relaxation nto contributions from water and ions, *i.e.* AOT plus all mobile ions. This revealed strong individual contributions of opposite sign, which resulted in a marginal total signal. In fact, even the inclusion of the strongly dipolar protein ubiquitin left the observed spectrum unchanged, due to the near-complete compensation of its dipole moment by the other constituents of the RM.

In this present study we want to extend our analysis to RM with different degrees of water loading and present a comparison of three RM systems with representative values of w_0. Based on these, we perform a detailed decomposition of DRS and THz spectra in two ways: by molecular species and by water solvation shells. Similar to D'Angelo *et al.*[12], we additionally investigate the influence of micellar tumbling motion on the dielectric relaxation spectrum. To this end, we decompose the dielectric response of the RM with the least water

w_0	n(H_2O)	n(AOT)	# Rep.	Length	Box
3	96	32	2	200 ns	110.3 Å
7.5	525	70	2	200 ns	111.34 Å
18	1800	100	3	100 ns	112.9 Å

Table 2.3 Overview of all simulations used for this study. The number of water and AOT molecules for the w_0 = 3 and w_0 = 7.5 systems were taken from Rosenfeld and Schmuttenmaer[9]. The simulations of w_0 = 18 are the same as those used for previous studies.[7,111] Additionally listed are the number of replica simulations and the respective simulation length of each of those, as well as the size of the cubic simulation box.

content into two largely independent modes of motion: relaxation by internal reorganization and overall micellar tumbling. Thereby, we develop a tool to correct spectra for the effect of tumbling motion that can be applied to experimental results as well.

2.3.2 Methods

In this work we present Molecular Dynamics (MD) simulations of reverse micelles (RM) in isooctane. The RM consist of nano-scale water pools, enclosed by a single layer of the detergent sodium bis(2-ethylhexyl) sulfosuccinate, also known as Aerosol-OT (AOT). Our simulations compare RM with different amounts of water loading, a quantity usually given as the concentration ratio $w_0 = [H_2O]/[AOT]$. We compare RM systems with w_0 = 3, 7.5 and 18. Tab. 2.3 gives details about the simulated systems. The exact number of water and AOT molecules per RM, and thereby its size, is dependent on the value of w_0.[9,62,115] The RM with w_0 = 3 and w_0 = 7.5 have the same compositions as used previously by Rosenfeld and Schmuttenmaer[9]. It should be noted that the water core of the RM with w_0 = 18 contained NaCl at physiological concentration (0.185 M). This is because this system was also used as reference in two recent studies of protein solvation.[7,111]

All MD simulations were done with DOMDEC CHARMM.[18,78] For each simulation, a single RM of representative size was preassembled inside a cubic box using the program PACKMOL.[79] The AOT tail groups and isooctane were modeled using the GROMOS96 united atom force field in version 45A3.[84] The force field parameters for the AOT head groups were taken from Abel *et al.*[66]. The water model we used in all simulations is SPC/E.[83] For a detailed account of the simulation setup and the force field used here, please refer to another recent paper.[111]

Analysis of the simulations was done using a modified and extended version of MDAnalysis.[92] Voronoi tessellations of the atomic coordinates were calculated using the Voro++[93] library.

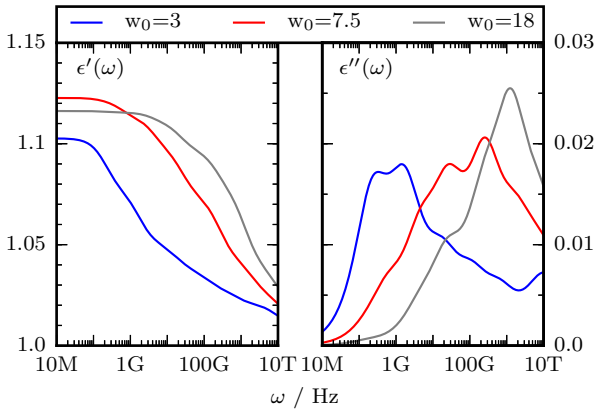

Figure 2.9 Comparison of the dielectric permittivity of RM systems with w_0 = 3 (blue), 7.5 (red) and 18 (grey). Left column: real part $\varepsilon'(\omega)$; right column: imaginary part $\varepsilon''(\omega)$. The spectra have all been normalized to correspond to a volume fraction $\Phi = 0.05$. The spectrum shown for w_0 = 18 has already been reported in a previous paper.[111]

2.3.3 Results and Discussion

Dielectric permittivity

In this section we present computational dielectric relaxation spectra of three RM systems with w_0 = 3, 7.5 and 18. Linear response theory[116] provides the means to calculate the frequency-dependent dielectric permittivity $\varepsilon(\omega)$ from the equilibrium time correlation function of the collective dipole moment via

$$\varepsilon(\omega) - 1 = \frac{4\pi}{3Vk_BT}\{\langle\vec{M}^2(0)\rangle_{eq} + i\omega\mathscr{L}[\langle\vec{M}(0)\cdot\vec{M}(t)\rangle_{eq}]\}, \tag{2.34}$$

where the collective dipole moment is given by

$$\vec{M}(t) = \sum_{\alpha} q_\alpha \, \vec{r}_\alpha(t). \tag{2.35}$$

Here, q_α and $\vec{r}_\alpha(t)$ are the atomic charges and positions, respectively, k_B is Boltzmann's constant, $\mathscr{L}[\ldots]$ denotes the Fourier-Laplace transform and the angular brackets represent the ensemble average. The equilibrium time correlation function $\langle\vec{M}(0)\vec{M}(t)\rangle_{eq}$ calculated from simulation data was characterized using a best fit to the model function

$$\langle\vec{M}(0)\vec{M}(t)\rangle_{eq} \approx \sum_{i=0}^{n} a_i \, e^{-t/\tau_i}. \tag{2.36}$$

This approach provides an expression of the dielectric spectrum in terms of analytical functions.[98]

Fig. 2.9 shows $\varepsilon(\omega)$ for the three RM systems. It should be noted that the spectra have been rescaled in such a way as to correspond to a volume fraction of the RM of 5% of the total solution. This represents a solution of non-interacting micelles[11] being implicitly assumed in our simulations. In this way, the respective values of the static dielectric permittivity $\varepsilon'(0)$

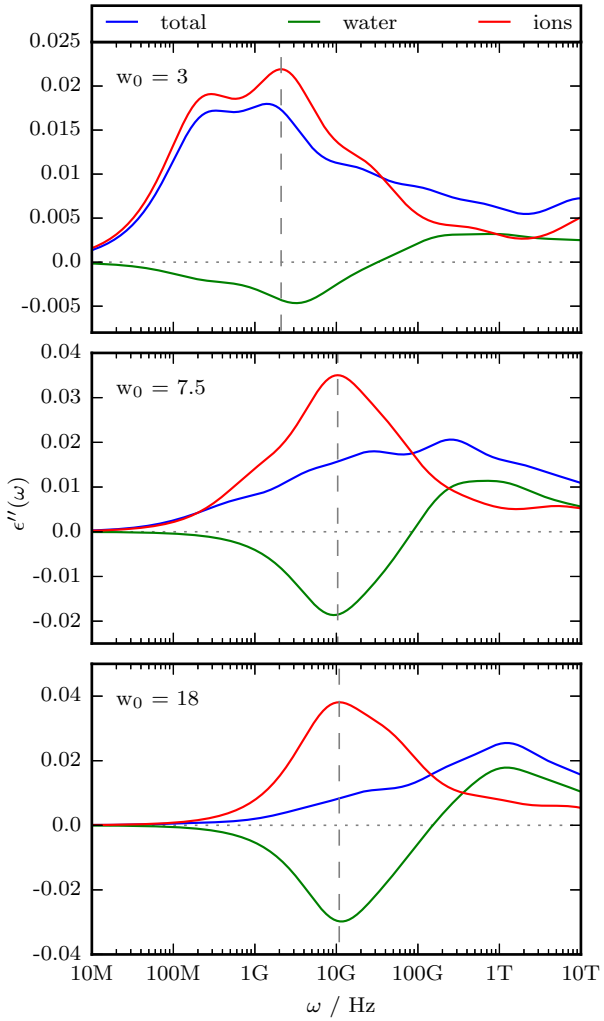

Figure 2.10 Species decomposition into ion (red) and water (green) of the total $\varepsilon''(\omega)$ (blue) of the different RM systems. The dashed grey lines highlight the respective position of the maximum of the ion component.

come very close to each other and are all slightly above 1.1. Bearing in mind, however, that ε_∞ is unity due to our non-polarizable simulations,[101] the offset of 0.1 is marginal, indeed. This shows that the depolarisation already described for w_0 =18 in our previous study[111] is valid for the other two RM as well. A comparison of the DRS of w_0 = 18 and bulk water can be found elsewhere.[111]

In accordance with experimental data,[10–12] the frequency-dependent dielectric permittivity $\varepsilon(\omega)$ in fact shows a clear dependence on w_0. With decreasing w_0 the main peak shifts to lower frequencies, indicating a retardation of collective dynamics. A first way to elucidate the mechanism behind this retardation is a decomposition of the dielectric response into contributions from the ions, *i.e.* AOT and mobile ions, and the water component according to Eq. 2.38. We note that uniting all ions in a single set forms a charge-neutral group with a well-defined dipole moment.

w_0	s1	s2	s3	s4+
3	96	-	-	-
7.5	439	86	-	-
18	949	513	253	85

Table 2.4 Average number of water molecules per solvation shell as defined by Voronoi tessellation.[96]

Separating the total dipole moment vector into various contributions i, one obtains

$$\vec{M}(t) = \sum_i \vec{M}_i(t). \tag{2.37}$$

This allows for a decomposition of $\varepsilon(\omega)$ following

$$\varepsilon(\omega) - 1 = \frac{4\pi}{3Vk_BT} \sum_i \{\langle \vec{M}(0) \cdot \vec{M}_i(0) \rangle_{eq} + i\omega \mathscr{L}[\langle \vec{M}(0) \cdot \vec{M}_i(t) \rangle_{eq}]\}. \tag{2.38}$$

In this way, each component dipole moment vector $\vec{M}_i$ is projected onto the total experimental observable $\vec{M}$. This projection represents the contribution of each component to the total observed spectrum. Such an approach goes along with the concepts of linear response theory.

Fig. 2.10 shows a decomposition by molecules species for the three RM systems studied here. A direct comparison of the already known results[111] for $w_0 = 18$ with those for $w_0 = 7.5$ shows that the component functions of the two systems are quite similar in shape as well as frequency. Indeed, for $w_0 = 7.5$ we find the same compensation mechanism[111] between ion and water components already reported for $w_0 = 18$. However, less water loading in the $w_0 = 7.5$ system means that the amplitude of the water contribution is significantly smaller relative to the ion contribution as compared to $w_0 = 18$. This leads to a reduction of the total signal in the frequency range ≈ 1 THz as well as a partial mitigation of the compensatory effect between the two components at ≈ 10 GHz. As a result, the complete spectrum appears to be shifted to lower frequencies due to a change of relative weighting between the two components, while there actually is only marginal change in component dynamics.

Component analysis reveals that for the RM with $w_0 = 3$ the situation is quite different. Not only the total spectral range, but also the individual component functions are shifted to lower frequencies. This is accompanied by a near-complete breakdown of the compensation mechanism between the ion and water components brought about by a marginalization of the water contribution. In other words, the low-frequency part of the total spectrum is largely congruent with the ion component spectrum.

Another way of decomposition is to further dissect the water component according to inwards counted solvation shells following Eqs. 2.37 and 2.38. Tab. 2.4 gives an overview of the respective number of solvation shells as defined by Voronoi tessellation[96] for the three RM systems as well as their average population. For $w_0 = 18$, we find the existence of four solvation shells, where half of all water molecules are located in the outermost shell in direct contact with AOT. The second and third shells each contain about half the number

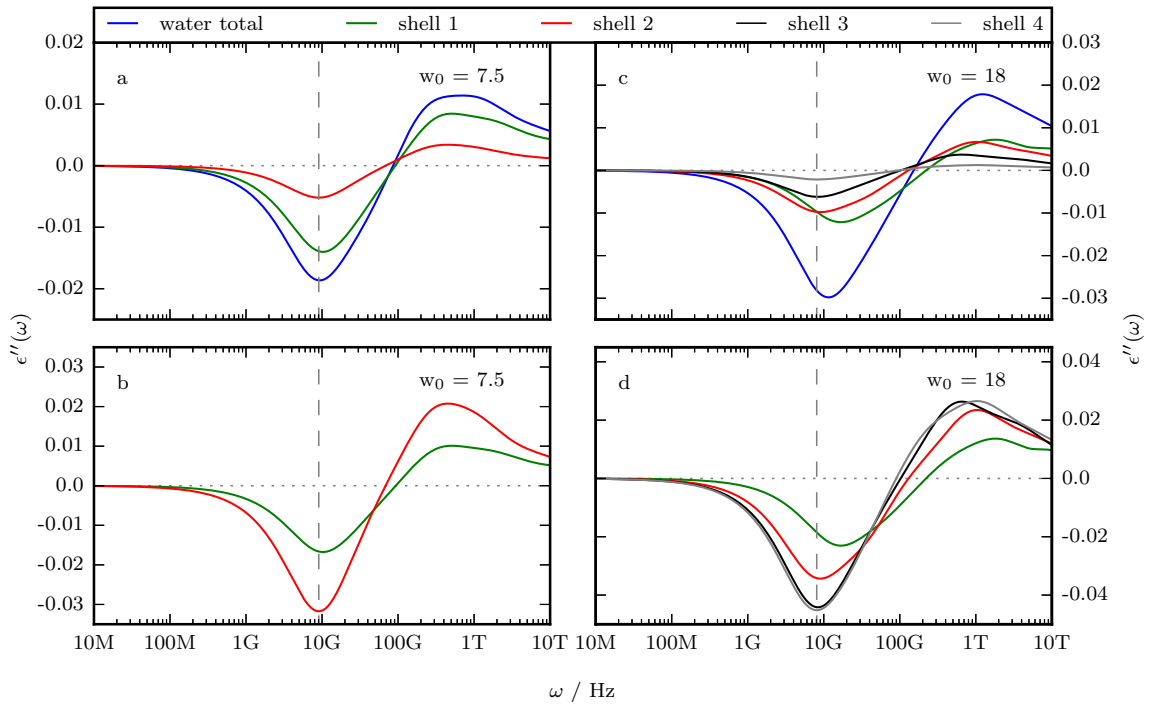

Figure 2.11 Solvation shell resolution of the imaginary part of the DRS, $\varepsilon''(\omega)$, shown for w_0 = 7.5 (a and b) and w_0 = 18 (c and d) RM systems. The plots a and c show how much each water shell contributes to the whole water signal. The plots b and d show each shell normalized to the number of waters in it (cf. Tab. 2.4). In this way, the amplitudes of the different shells are comparable. The grey dashed lines mark the position of the minimum of the respective innermost shell.

of water molecules of the preceding shell. For $w_0 = 7.5$ we find that five out of six water molecules are in direct contact with AOT, while in the RM with $w_0 = 3$ all water molecules are in the first solvation shell, prohibiting further decomposition. Panels a and c of Fig. 2.11 show the contributions of each solvation shell to the total water component of the dielectric spectrum for $w_0 = 7.5$ and 18. These absolute contributions are furthermore normalized with respect to their population number. The results are given in panels b and d of Fig. 2.11. The normalization by population number reveals the progressive decrease of relative amplitudes in the outermost solvation shells. This shows clearly that the inherent structural depolarisation previously reported[111] for $w_0 = 18$ is observed for $w_0 = 7.5$ in much the same way.

Furthermore, decomposition into solvation shells reveals dynamical heterogeneity within the water droplet. The contribution of the outermost shell is found to be of higher frequency as compared to the inner ones, as shown in Fig. 2.11. The effect is visible in both systems, but significantly more prevalent in $w_0 = 18$. We want to emphasize again that in our component analysis each $\vec{M}_i$ is projected onto the total dipole moment. As such, our observation means that only the contribution of the first shell to the total spectrum is accelerated, which reflects only part of the total intrinsic dynamics of the first shell itself. The most intuitive way to obtain a complete description of a solvation shell would be to calculate a self-correlation function of its collective dipole moment. However, this automatically leads to the question

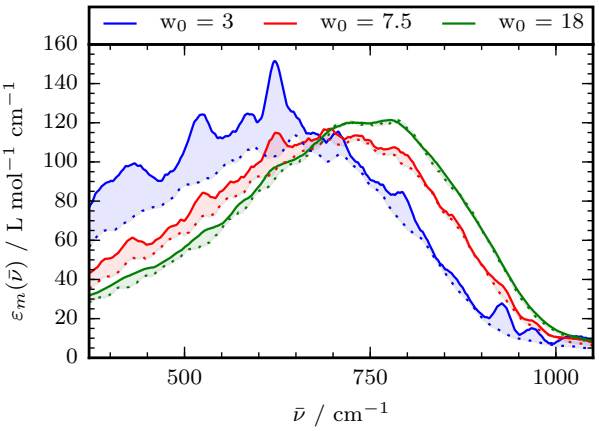

Figure 2.12 Molar extinction coefficients $\varepsilon_m(\bar{\nu})$ shown for the different RM systems. The total spectra are shown as thick lines, the dotted lines give the respective water contribution, and the shaded areas highlight the contributions of the ion components to the respective total spectrum. $\varepsilon_m(\bar{\nu})$ was calculated from the THz region of the dielectric spectrum and normalized to the respective water concentration. Our simulation results are in good agreement with experimental spectra (cf. Fig. 1 by Venables *et al.*[8]).

of how to deal with migration of water molecules between solvation shells. In preliminary studies, the results of which are not shown here, we have compared two ways of dealing with migration: one method[7] defines shell membership only at the beginning of a time series. Alternatively, shell membership is assigned instantaneously at the actual point in time. We have found that self and cross-terms calculated with one or the other method differed significantly, thereby complicating interpretation. However, the sum of self and cross-terms for a specific shell is found to be invariant between both methods. Therefore, projecting a shell onto the total dipole moment also is invariant and thus free of migration artifacts.

THz spectra

The high-frequency part of the dielectric permittivity is reported in the form of the molar extinction coefficient $\varepsilon_m(\bar{\nu})$, normalized by the molar concentration of water in each respective RM system. The connection between the molar extinction coefficient $\varepsilon_m(\bar{\nu})$ and the dielectric permittivity $\varepsilon(\omega)$ is given following Sega and Schröder[91], Rosenfeld and Schmuttenmaer[9] and Wooten[108] as described previously.[111] In this frequency range, classical MD simulations can only reproduce the peak stemming from water librations at ≈ 600 cm^{-1}.[15] We note, however, that the water model SPC/E used in this work is able to reproduce water librations with satisfying agreement with experiment.[91] Molar extinction coefficients for the three RM systems used here, including decomposition into water and ion contributions, are shown in Fig. 2.12. The spectra have been calculated by numerically solving the Fourier-Laplace transformations in Eqs. 2.34 and 2.38 and applying subsequent smoothing using the Savitzky-Golay algorithm.[105] A direct comparison between our computational spectrum for $w_0 = 18$ and bulk water can be found in our previous study.[111]

Considering the dependence of the molar extinction coefficient on water loading w_0, we

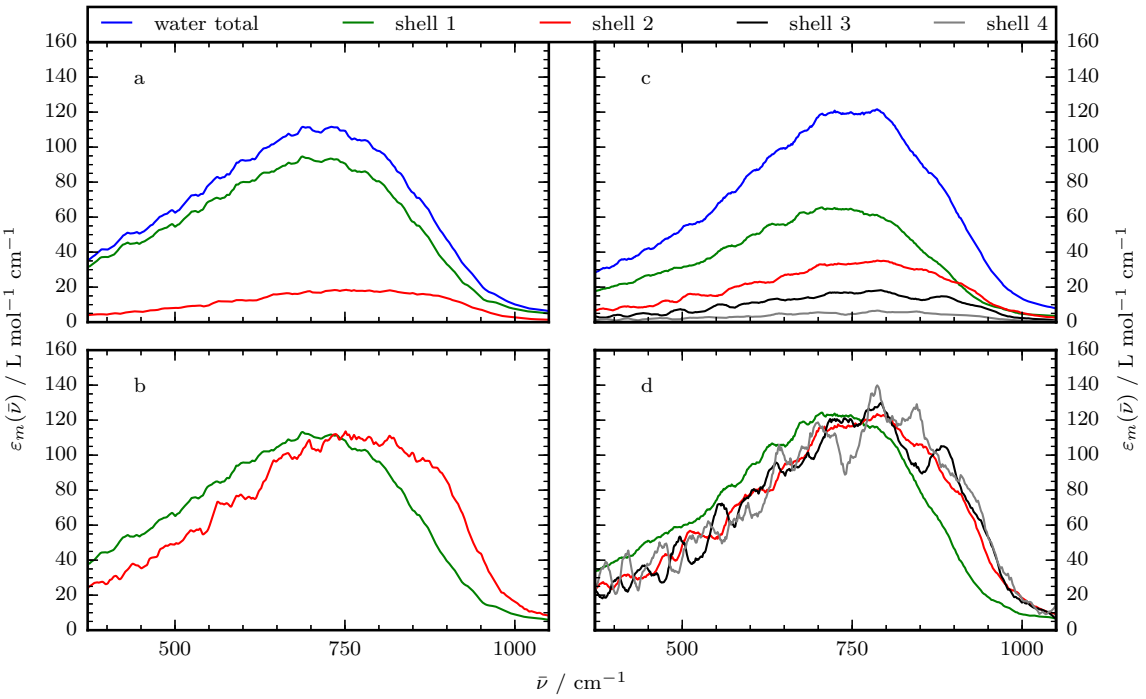

Figure 2.13 Solvation shell resolution of the molar extinction coefficients $\varepsilon_m(\bar{\nu})$ shown for w_0 = 7.5 (a and b) and w_0 = 18 (c and d) RM systems. The plots a and c show how much each water shell contributes to the whole water signal. The plots b and d show each shell normalized to the number of waters in it (cf. Tab. 2.4). In this way, the amplitudes of the different shells are comparable.

find very good qualitative agreement with experiment.[8,15] The two essential features are reproduced. First, a shift of the peak maximum from ≈ 700 cm^{-1} for $w_0 = 18$ to ≈ 600 cm^{-1} for $w_0 = 3$. Second, the increasing "ruggedness" of the spectrum with decreasing w_0, meaning the emergence of well-structured sub-peaks attributed to AOT modes, as already proposed by Venables *et al.*[8]. In fact, our results are a substantial improvement over previous simulation results.[9] This previous study was employing a simplified model of RM, where the outside medium isooctane was described by a continuum model and the RM were kept in spherical shape constrained by a wall potential.[62] The explicit simulation of the outside medium as well as the release of a shape contraint appear to be necessary for bringing simulation results closer to experiment.

A decomposition of the molar extinction coefficient into contributions from ions and water confirms[8] that the increasing "ruggedness" in the spectra is caused solely by the ion component. As can be seen in Fig. 2.12, the water component remains rather smooth even for $w_0 = 3$, but it is shifted to lower frequencies. Consequently, the increased emergence of sub-peaks appears to reflect collective modes of motion of AOT.

Fig. 2.13 shows a decomposition of the total water component of $\varepsilon_m(\bar{\nu})$ into contributions from individual solvation shells. The shell resolution was already introduced in the dielectric permittivity as described in Eq. 2.38. The so-decomposed dielectric permittivity was then converted to $\varepsilon_m(\bar{\nu})$ as described above. The net contribution of each solvation shell to the molar extinction coefficient for $w_0 = 7.5$ and 18 is shown in panels a and c, respectively. The

situation becomes clearer when again normalizing each shell contribution by its respective population number as given in Tab. 2.4. As shown in panels b and d of Fig. 2.13, this normalization makes the results for the two systems quite similar. The outermost solvation shell is shifted to a lower wave number as compared to the subsequent inner shells. In fact, for $w_0 = 18$, all three inner shells have the same dynamical behaviour.

The impact of micellar tumbling on the dielectric spectrum

In this section we will analyze the impact of overall micellar tumbling motion on the observed frequency-dependent dielectric permittivity. In principle, the collective dipole moment of a structure such as a reverse micelle has two major pathways of relaxation: internal reorganization and overall rotation. If the two processes occur on similar time scales, micellar rotational diffusion will have a significant impact on the observed DRS. We develop a method to observe the RM in a rotating frame that altogether excludes micellar tumbling. This allows for a decomposition of the observed relaxation into the two aforementioned pathways.

Overall micellar rotation is calculated using the Horn algorithm[117] in the following way. This algorithm calculates a rotation matrix describing a best fit alignment of two sets of points, e.g. two sets of coordinates of a semi-rigid body at two distinct points in time. As RM are non-rigid bodies exhibiting fluctuations in their overall shape as well as internal reorganization by means of diffusion, the Horn algorithm is not suited to superimpose two coordinate sets of the same RM taken at distant times. Thus, we calculate best-fit rotation matrices only from one time step to the next, thereby avoiding the aforementioned problems. We have chosen the centers-of-mass of all AOT head groups as reference points for this calculation. In this way, we define the micellar coordinates in a rotating frame (RF), in which the overall rotation of the RM as a whole has been removed, in addition to the usual laboratory frame (LF), which includes overall rotation.

The Horn matrix $B(t)$ gives the best-fit rotation connecting two consecutive frames in the simulation. This can be written as

$$\vec{r}_{\mathrm{RF}}(t) \approx B(t) \cdot \vec{r}_{\mathrm{RF}}(t - \Delta t), \tag{2.39}$$

where Δt is the discrete time step of the simulation. Recursively inserting Eq. 2.39 into itself for n prior frames leads back to a starting position, which then forms the (arbitrarily chosen) reference frame for the RF:

$$\begin{aligned}
\vec{r}_{\mathrm{RF}}(t) &\approx B(t) \cdot B(t - \Delta t) \cdot \vec{r}_{\mathrm{RF}}(t - 2\Delta t) && (2.40)\\
&\approx B(t) \cdot B(t - \Delta t) \ldots B(\Delta t) \cdot \vec{r}_{\mathrm{RF}}(t - n\Delta t) && (2.41)\\
&\approx \underbrace{\left(\prod_{i=0}^{n-1} B(t - i\Delta t) \right)}_{=R(t)} \cdot \vec{r}_{\mathrm{RF}}(t - n\Delta t) && (2.42)
\end{aligned}$$

The matrix $R(t)$ is the result of the product of all previous incremental rotation matrices and

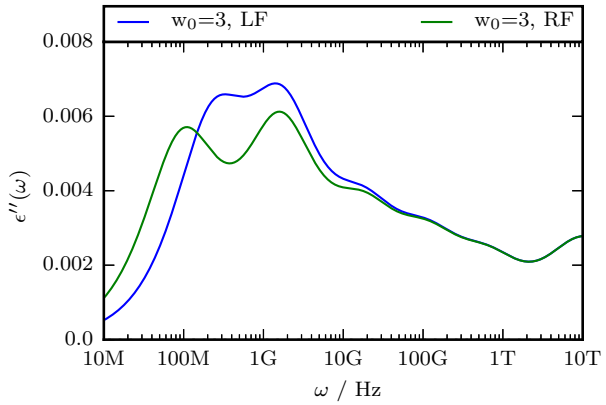

Figure 2.14 Comparison of $\varepsilon''(\omega)$ in the two reference frames, namely the laboratory frame (LF) and the rotating frame (RF). The RF spectrum shows only the internal relaxation behaviour, while the LF spectrum includes micellar tumbling motion as an additional relaxation mechanism. Relaxation times that are different: τ_1^{LF} = 4570 ps vs. τ_1^{RF} = 10500 ps and τ_2^{LF} = 573 ps vs. τ_2^{RF} = 616 ps.

thus forms the connection between LF and RF:

$$\vec{r}_{\mathrm{RF}}(t) \approx R(t) \cdot \vec{r}_{\mathrm{LF}}(t) \tag{2.43}$$

In other words, the matrix $R(t)$ describes the overall rotation of the RM over the course of the simulation. The mean tumbling time $\langle \tau_{\mathrm{rot}} \rangle$ can be calculated as the asymptotic value of the integral of the averaged correlation functions of the three column vectors of $R(t)$, which can be written as

$$\langle \tau_{\mathrm{rot}} \rangle \approx \lim_{\beta \to \infty} \int_0^{\beta} \langle \frac{1}{3} \mathrm{Tr}(R(t) \cdot R^T(0)) \rangle dt. \tag{2.44}$$

The mean micellar rotation time $\langle \tau_{\mathrm{rot}} \rangle$ can then be used to calculate the influence of overall micellar rotation on the dielectric spectrum. Assuming that overall rotation and internal dipolar relaxation are independent processes, one can approximate the relationship between the dipolar correlation functions in the two reference frames as the product

$$\langle \vec{M}(0)\vec{M}(t) \rangle_{\mathrm{RF}} \, e^{-t/\langle \tau_{\mathrm{rot}} \rangle} \approx \langle \vec{M}(0)\vec{M}(t) \rangle_{\mathrm{LF}}. \tag{2.45}$$

Further quantification of the influence of overall rotation can be achieved by representing the time correlation functions through multi-exponential fit functions as shown in Eq. 2.36. This way, Eq. 2.45 can be rewritten as

$$\underbrace{\sum_{i=1}^{n} a_i \, e^{-t/\tau_i^{\mathrm{RF}}}}_{\approx \langle \vec{M}(0)\vec{M}(t) \rangle_{\mathrm{RF}}} e^{-t/\langle \tau_{\mathrm{rot}} \rangle} \approx \underbrace{\sum_{i=1}^{n} a_i \, e^{-t/\tau_i^{\mathrm{LF}}}}_{\approx \langle \vec{M}(0)\vec{M}(t) \rangle_{\mathrm{LF}}}, \tag{2.46}$$

resulting in the relationship

$$\frac{1}{\tau_i^{\mathrm{RF}}} + \frac{1}{\langle \tau_{\mathrm{rot}} \rangle} \approx \frac{1}{\tau_i^{\mathrm{LF}}}. \tag{2.47}$$

Eq. 2.46 shows that only the relaxation times of the individual exponential functions are

w_0	$\langle\tau_{rot}\rangle$ [ps]	$\langle V_{voro}\rangle$ [Å^3]	η [mPa s]
18	32100	124500	0.26
7.5	16900	64900	0.26
3	6650	25700	0.26

Table 2.5 The average tumbling time $\langle\tau_{rot}\rangle$ was calculated following Eq. 2.44. The mean volume of the RM is given as the time average of the sum of the volumina of all atomic Voronoi cells consituting the RM. These two quantities are used to calculate the viscosity η of the outside medium following Eq. 2.50.

modified by overall micellar rotation, while their relative weighting coefficients a_i remain the same. The consequence of the relationship between τ_i^{RF} and $\langle\tau_{rot}\rangle$ in Eq. 2.47 is that if one of the two is much smaller than the other, it will determine the observed relaxation time τ_i^{LF}. If micellar tumbling is much slower than internal relaxation, then the collective dipole moment will have relaxed long before any significant tumbling motion has happened, as is the case for our RM with $w_0 = 7.5$ and 18. Alternatively, if τ_i^{RF} and $\langle\tau_{rot}\rangle$ are of comparable size, the observed τ_i^{LF} will actually reflect neither of the two competing relaxation pathways alone. In fact, the observed relaxation time will be a mixture of both.

For our $w_0 = 3$ system we find such a phenomenon. Fig. 2.14 shows a direct comparison of the dielectric spectrum of this system as observed in respect to the two reference frames LF and RF. The slowest process visible in the spectrum corresponds to $\tau_1^{RF} = 10500$ ps, which is of comparable size to $\langle\tau_{rot}\rangle = 6650$ ps, as shown in Tab. 2.5. The corresponding signal in the LF spectrum is recorded with a $\tau_1^{LF} = 4570$ ps. The relationship between these times is well approximated by Eq. 2.47. The subsequent signal in the spectrum is recorded at $\tau_1^{RF} = 616$ ps, which is already one order of magnitude faster than micellar tumbling. Accordingly, the respective time in the LF spectrum of 573 ps shows that the observed times are quite similar for RF and LF. The higher frequency part of the two spectra are almost identical, with individual internal relaxation processes being much faster than micellar tumbling.

In order to apply this formalism in an experimental situation, we now utilize the calculated $\langle\tau_{rot}\rangle$ in a different context. Hydrodynamic theory provides a link between the average micellar tumbling time, the volume of the RM and the viscosity of the outside medium via the Debye-Stokes formula:

$$\langle\tau_{rot}\rangle = \frac{4\pi a^3}{k_B T}\eta \tag{2.48}$$

$$= \langle V_{voro}\rangle \frac{3\eta}{k_B T}. \tag{2.49}$$

Here, we equate the Voronoi volume $\langle V_{voro}\rangle$, *i.e.* the sum of the volumes of all atomic Voronoi cells constituting the RM, with $4\pi a^3/3$, where a is the hydrodynamic radius of the RM. Reforming this last equation, the viscosity η can be calculated following

$$\eta = \frac{\langle\tau_{rot}\rangle}{\langle V_{voro}\rangle}\frac{k_B T}{3}. \tag{2.50}$$

As shown in Tab. 2.5, inserting $\langle\tau_{\mathrm{rot}}\rangle$ obtained from the rotational relaxation function (cf. Eq. 2.44) and the Voronoi volume into the above equation, all three RM systems give the very same viscosity. Thus, the application of hydrodynamics to describe the tumbling motion of AOT reverse micelles appears to be valid. This also means that one can calculate the tumbling time of a reverse micelle using Eq. 2.49, once the viscosity of the outside medium and the volume of the RM are known.

Our observations show that the obtained dielectric spectrum may depend on the choice of the outside solvent alone, even if internal dynamics of the RM remain the same. Even more important, the applicability of the Debye-Stokes formula to describe micellar tumbling has far-reaching consequences. Once the viscosity of the outside medium as well as the hydrodynamic radius of the RM are known, $\langle\tau_{\mathrm{rot}}\rangle$ can be calculated using Eq. 2.49. The so-obtained $\langle\tau_{\mathrm{rot}}\rangle$ can then be inserted into Eq. 2.47 to check for and eventually eliminate the influence of micellar tumbling in an experimental situation as well.

2.3.4 Conclusion

In this computational study we present and analyze the dielectric and THz spectra of three water/AOT/isooctane reverse micelles with $w_0 = 3$, 7.5 and 18. We show that the frequency-dependent dielectric permittivity is shifted to lower frequencies with decreasing water loading w_0, which is in accordance with experiment. A decomposition of the dielectric spectrum into contributions from water and ions reveals two things: first, the shift between $w_0 = 18$ and 7.5 is brought about by a change in the interplay of these two components, whose individual dynamical properties are quite the same for the two systems. The shift in the total spectrum comes from a reduction of the relative weight of the water component. For $w_0 = 3$, the total spectrum as well as the individual components are shifted to lower frequencies and the low-frequency range of the total spectrum is largely dominated by the ion contribution. In the THz region, the dielectric permittivity was converted to the molar extinction coefficient. For the dependence of the latter on w_0, we find very good agreement with experimental results. Furthermore, a decomposition into water and ion contributions reveals that for lower w_0 the ion contribution becomes ever more significant and creates characteristic sub-peaks also seen in experiment.

A resolution of both, the dielectric permittivity as well as the molar extinction coefficient, into contributions from individual water shells leads to seemingly contradicting results. In the dielectric spectrum, the first shell yields higher-frequency contributions than the inner shells, while in the molar extinction coefficient the first shell is shifted to lower frequencies. We emphasize that both computational spectra are computed from the very same time correlation function. However, each experimental technique selects specific time windows, which are affected in different ways. The picture is further complicated, when considering the strong retardation observed in single-particle dynamics of water molecules near AOT, even if calculated from the very same simulation (cf. Braun *et al.*[7]). It seems clear that for heterogeneous systems such as RM, simple correlations[46–48] between collective and single-particle dynamics no longer are valid. Further investigation into this subject is necessary to obtain a

more thorough understanding.

In addition to the aforementioned spatial decompositions by molecular species and solvation shells we also present a decomposition of the total observed dipolar relaxation into largely independent modes of motion: relaxation by internal reorganization and by overall tumbling motion. We show that if both processes occur within a similar time scale the observed dielectric spectrum is modulated and is not solely due to internal relaxation within the RM. We observe this phenomenon for our $w_0 = 3$ system, where the low-frequency part of the dielectric spectrum is modulated. Our analysis shows that micellar tumbling obeys the laws of hydrodynamics, which allows for a computation of the mean tumbling time solely from the viscosity of the outside medium and the volume of the RM. Furthermore, we show that these two parameters suffice to correct the dielectric spectrum for the effects of micellar tumbling. In this way, this correction can be applied to experimental spectra as well.

Acknowledgement

We thankfully acknowledge financial support for this research by the Austrian Science Fund (FWF) in the course of project P23494.

3 Solvation Dynamics of coumarin 153 in Ionic Liquids

3.1 Overview

Ionic liquids (IL) have shown remarkable properties as solvents, e.g. as highly effective extraction solvents or as reaction media with catalytic abilities. In this context, it is of special importance to learn more about solute-solvent interactions in IL. The time-dependent Stokes shift (TDSS) offers a possibility to study solvation dynamics by measuring the time-resolved capacity of solvent molecules to relax around a solute after a change in its electrostatic properties.

In principle, this method is similar to dielectric relaxation spectroscopy, where a solvent's susceptibility to an externally applied electric field is measured. Similarly, the TDSS can be seen to observe how susceptible a solvent is to a change in the electric field exerted by the solute as a local probe of its environment. Indeed, good results can be obtained for polar solvents by employing a model representing the solute as an electric dipole in a cavity and describing the solvent as a dielectric continuum characterized by its frequency-dependent dielectric permittivity. In this way, the TDSS can be calculated from a dielectric relaxation spectrum. The publication presented in Sec. 3.2 investigates why such a reaction field continuum model predicts too fast TDSS relaxation times in IL.

Sec. 3.3 contains a manuscript recently submitted for publication, where non-equilibrium simulations of the chromophore coumarin 153 in a coarse-grained IL model are utilized to obtain a detailed decomposition of the TDSS. Contributions to the total signal are separated in terms of ionic species and solvation shells. Additionally, the high number of 4000 independent replica simulations of the TDSS allows for a decomposition of the total effect down to individual atoms of the solute.

3.2 Dielectric spectra of ionic liquids and their conversion to solvation dynamics: A detailed computational analysis of polarizable systems

Phys. Chem. Chem. Phys., ***16***, *10999 (2014)*

Michael Schmollngruber,[a] Christian Schröder[a] and Othmar Steinhauser[a]

[a] *University of Vienna, Department of Computational Biological Chemistry, Währingerstrasse 17, A-1090 Vienna, Austria*

For the three molecular ionic liquids 1-ethyl-3-methylimidazolium tetrafluoroborate, 1-ethyl-3-methylimidazolium trifluoromethanesulfonate and 1-butyl-3-methylimidazolium tetrafluoroborate, dielectric spectra were calculated from molecular dynamics simulations based on polarizable force fields. Using the reaction field continuum model the dielectric spectra were converted to the solvation dynamics of Coumarin 153. It is shown in detail that the inclusion of the static conductivity in this model is essential. When simplifying the dielectric spectrum to the static conductivity hyperbola, the solvation response function becomes mono-exponential. Taking into account the frequency dependence of the conductivity, the typical two time-regimes of the solvation response function in ionic liquids are already obtained. However, the mean relaxation time remains the same. When converting the complete dielectric spectrum, i.e. also including frequency-dependent dielectric permittivity, quantitative changes are observed, but the qualitative shape is conserved. In accordance with previous experimental studies, solvation dynamics in ionic liquids predicted by the reaction field continuum model is too fast for longer times. This correlates with the suppression of the fine structure of the dielectric spectrum at low frequencies by the static conductivity hyperbola. By scaling down the static conductivity this effect can be partially amended. In addition to the impact of the solvent dielectric spectrum on solvation dynamics, also solute-specific effects, i.e. anisotropy in shape and charge distribution as well as polarizability, were studied.

3.2.1 Introduction

Ionic liquids are characterized by an anisotropy in charge distribution and shape. This combination makes them a challenging class of soft matter when dealing with their electrostatic or dielectric properties, as they unite the properties of polar liquids and ionic melts. At the molecular level, they have a net charge and a dipole moment and as opposed to ionic solutions, both reside on the very same molecule. At the dielectric or mesoscopic level these properties correspond to the dielectric conductivity $\vartheta(\omega)$ and the dielectric permittivity $\varepsilon(\omega)$, respectively.[98,118,119] While the former stands for collective translation, the latter is representative of collective rotation. In any case, it is the response to an applied external electric field, as measured in dielectric spectroscopy. An alternative method is to detect the internal Maxwell field exerted on a solute used as a probe, being Coumarin 153 in most cases.[120–125] In this case, the solute is excited to its electronic S_1 state and it is the accompanying change in the dipole moment that is coupling to the Maxwell field. The relaxation of the surrounding solvent after the excitation of the solute is recorded via time-resolved fluorescence spectroscopy, yielding what is commonly known as the solvation response function or solvation dynamics. This method has a long tradition for polar solvents[126–132]. In recent years, it was also applied to ionic liquids.[45,121–124,133–148]

As both methods, dielectric spectroscopy and solvation dynamics, operate with electric fields, either as a perturbation or as a response, investigations into their mutual relation exist in the literature. In most of these studies the focus was on experimental data.[45,122–124,146,149] In this study we operate with computational methods, calculating the dielectric spectrum and the solvation response function from the very same simulation. For the conversion of the former into the latter we use the reaction field continuum model (RFCM), because it does not need data from another source than the dielectric spectrum. In previous studies based on experimental dielectric spectra, the RFCM worked very well for polar liquids, but faced problems for charged dipolar systems, i.e. ionic liquids. A computational approach allows to study how parts of the dielectric spectrum - when considered separately - influence the solvation response function. In this way we hope to elucidate the peculiar problems encountered[122–124,146] when applying the RFCM to ionic liquids.

Recently, there have also been other attempts beyond those based on a simple continuum model to predict the solvation response function of ionic liquids, either employing a semi-molecular approach[144,145] or an extended Debye-Hückel model[121].

This paper is organized as follows: In the theory section a short overview of the development of the RFCM and its application to ionic liquids is given. Special attention was paid to anisotropic features of the solute C153. The results and discussion section starts with the presentation of the computational dielectric spectra. Subsequently, the solvation response function is characterized within the framework of the RFCM. Fundamental analytic results are collected in the appendix and background information concerning the calculation of the dielectric spectra is given in the supplementary material.

3.2.2 Theory

Calculation of the solvation response function from the frequency-dependent generalized dielectric constant

The normalized time-dependent solvation response function is given by

$$S(t) = \frac{\Delta U(t) - \Delta U(\infty)}{\Delta U(0) - \Delta U(\infty)}, \tag{3.1}$$

where $U(t)$ is the solvation energy. At time $t = 0$ the charge distribution of a chromophore molecule embedded in a solvent is changed due to photoexcitation. The relaxation of the solvent molecules in response to this change of the charge distribution $\Delta\rho(\vec{r},t)$ of the solute results in a transient shift of the solvation energy

$$\Delta U(t) = \frac{1}{2}\int \Delta\rho(\vec{r},t)\Phi(\vec{r},t)d\vec{r}, \tag{3.2}$$

where $\Phi(\vec{r},t)$ is the total electrostatic potential exerted by the solvent. A first approximation of this potential is given by enclosing the charge distribution of the solute $\Delta\rho(\vec{r},t)$ in a spherical cavity of radius a and describing the solvent outside by a dielectric continuum with a static dielectric constant ε:

$$\Phi(\vec{r}) = \sum_{l=0}^{\infty}\sum_{m=-l}^{+l} -\frac{\varepsilon - \varepsilon_c}{\varepsilon + \varepsilon_c \frac{l}{l+1}} \frac{q_m^l}{a^{2l+1}} r^l Y_m^l(\theta,\phi). \tag{3.3}$$

Furthermore, it is assumed that the cavity is filled with a dielectric medium characterized by the constant ε_c. The spatial variation of the potential within the cavity is described by the solid spherical harmonics $r^l Y_m^l(\theta,\phi)$. The anisotropy of the charge distribution of the solute is characterized by its multipole moments

$$q_m^l = \int \Delta\rho(\vec{r}) r^l Y_m^l(\theta,\phi)d\vec{r}. \tag{3.4}$$

Inserting the static potential $\Phi(\vec{r})$ into Eq. 3.2 one gets the temporal average of the solvation energy

$$\langle\Delta U\rangle = -\frac{1}{2}\sum_{l=0}^{\infty} \frac{\varepsilon - \varepsilon_c}{\varepsilon + \varepsilon_c \frac{l}{l+1}} \frac{1}{a^{2l+1}} \sum_{m=-l}^{+l} q_m^l q_m^{l*}. \tag{3.5}$$

For the special case $l = 1$, i.e. for a single dipole $\vec{\mu}$ enclosed in the cavity this reduces to the original formula of Boettcher and Bordewijk[116]

$$\langle\Delta U_\mu\rangle = -\frac{1}{2}\frac{\Delta\vec{\mu}^2}{a^3}\frac{\varepsilon - \varepsilon_c}{\varepsilon + \frac{\varepsilon_c}{2}} = -\frac{1}{2}\Delta\vec{\mu}\cdot\vec{E}_{RF}, \tag{3.6}$$

where in the second step we have introduced the reaction field

$$\vec{E}_{RF} = \frac{\Delta\vec{\mu}}{a^3}\frac{\varepsilon - \varepsilon_c}{\varepsilon + \frac{\varepsilon_c}{2}}. \tag{3.7}$$

The factor $\Delta\vec{\mu}^2/a^3$ in Eq. 3.6 is a dipolar energy representative of the solute. The dimensionless co-factor involving the dielectric constant stands for the solvation properties of the solvent. Maroncelli and Fleming[150] realized that Eq. 3.7 gives an incorrect limit for $\varepsilon = 1$, i.e. the reaction field does not vanish in the absence of a solvent, but gives a value dependent on ε_c. In fact, this represents a spurious self-interaction of the solute dipole with its own cavity. This can be amended by the method of Mazurenko[151] as recommended by Maroncelli and Fleming.[150] This method augments the permanent dipole moment $\Delta\vec{\mu}$ by an induced contribution $\Delta\vec{\mu}_{ind} = \alpha\vec{E}_{RF}$

$$\vec{E}_{RF} = \frac{\Delta\vec{\mu} + \alpha\vec{E}_{RF}}{a^3}\frac{\varepsilon - 1}{\varepsilon + \frac{1}{2}}, \tag{3.8}$$

where α is the molecular polarizability of the solute. Consequently, ε_c was set to unity. However, it re-enters via the Clausius-Mosotti equation

$$\frac{\alpha}{a^3} = \frac{\varepsilon_c - 1}{\varepsilon_c + 2}, \tag{3.9}$$

yielding

$$\vec{E}_{RF} = \frac{\Delta\vec{\mu}}{a^3}\frac{\varepsilon_c + 2}{3}\frac{\varepsilon - 1}{\varepsilon + \frac{\varepsilon_c}{2}}. \tag{3.10}$$

So far, the reaction field is only a temporal average as it includes only the static dielectric constant. To introduce the time dependence we start from the constitutive relation in the frequency domain

$$\vec{P}(\vec{r},\omega) = \frac{\varepsilon(\omega) - 1}{4\pi}\vec{E}(\vec{r},\omega), \tag{3.11}$$

giving the dielectric polarization $\vec{P}(\vec{r},\omega)$ for systems composed of neutral dipolar molecules. Both, $\vec{P}(\vec{r},\omega)$ and $\vec{E}(\vec{r},\omega)$ can be combined to the dielectric displacement

$$\vec{D}(\vec{r},\omega) = \vec{E}(\vec{r},\omega) + 4\pi\vec{P}(\vec{r},\omega) = \varepsilon(\omega)\vec{E}(\vec{r},\omega). \tag{3.12}$$

The static reaction field (Eq. 3.7) was obtained as a solution of the Laplace equation under the boundary conditions that the parallel component of $\vec{E}(\vec{r})$ and the normal component of $\vec{D}(\vec{r})$ are continuous at the spherical surface. Again applying these boundary conditions, but now to the general frequency-dependent electric field and dielectric displacement (Eq. 3.12), yields[152]

$$\vec{E}_{RF}(\omega) = \frac{\Delta\vec{\mu}}{a^3}\frac{\varepsilon_c + 2}{3}\frac{\varepsilon(\omega) - 1}{\varepsilon(\omega) + \frac{\varepsilon_c}{2}}. \tag{3.13}$$

Here, ε_c as a constant value describes the fixed geometry of the solute, whereas $\varepsilon(\omega)$ stands for the relaxation of the solvent. As an ionic liquid is composed of charged, dipolar molecules, its dielectric properties have to be described by the generalized permittivity[98]

$$\Sigma(\omega) = \varepsilon(\omega) - 1 + \frac{4\pi i\sigma(\omega)}{\omega}, \tag{3.14}$$

where the dielectric conductivity $4\pi i\sigma(\omega)/\omega$ describes the creation of collective dipole moments by the mutual translational motion of charged species. This generalizes the constitutive

relation to

$$\vec{P}(\vec{r},\omega) = \frac{\Sigma(\omega)}{4\pi}\vec{E}(\vec{r},\omega) \tag{3.15}$$

and the dielectric displacement to

$$\vec{D}(\vec{r},\omega) = \vec{E}(\vec{r},\omega) + 4\pi\vec{P}(\vec{r},\omega) = (\Sigma(\omega)+1)\vec{E}(\vec{r},\omega). \tag{3.16}$$

In other words, for charged dipolar systems $\Sigma(\omega)+1$ replaces $\varepsilon(\omega)$ in Eq. 3.12 in case of neutral dipolar systems. Applying the same boundary conditions as above the reaction field can be generalized to

$$\vec{E}_{RF}(\omega) = \frac{\Delta\vec{\mu}}{a^3}\frac{\varepsilon_c+2}{3}\frac{\Sigma(\omega)}{\Sigma(\omega)+1+\frac{\varepsilon_c}{2}}. \tag{3.17}$$

Generalizing the theory developed by Hsu *et al.*[152] for neutral dipolar solvents to the case of ionic liquids by replacing Eq. 3.13 with Eq. 3.17 we get the analogous expression for the solvation energy

$$\Delta U_\Sigma(t) = \frac{2}{\pi}\int_0^\infty \frac{cos(\omega t)}{\omega} Im\left[\frac{\Sigma(\omega)}{\Sigma(\omega)+1+\frac{\varepsilon_c}{2}}\right] d\omega. \tag{3.18}$$

Strictly speaking, the above equation should contain the dipolar energy $-(\Delta\vec{\mu}^2/a^3)((\varepsilon_c+2)/3)$ as a prefactor. However, when substituting $\Delta U(t)$ into Eq. 3.1, giving the solvation response function, the dipolar energy cancels out. Therefore, it is omitted in the above and following equations, where only the dimensionless part is retained.

Analytical calculation of the mean relaxation time of $S_\Sigma(t)$

At the global level, the most important property of the solvation response function $S_\Sigma(t)$ is its mean relaxation time

$$\tau_\Sigma = \int_0^\infty S_\Sigma(t)dt. \tag{3.19}$$

According to Eq. 3.1, $S_\Sigma(t)$ is calculated from the solvation energy ΔU_Σ at times t, zero and infinity. As the asymptotic value of $\Delta U_\Sigma(t)$ approaches values close to zero (data not shown), its asymptotic value is omitted in order to simplify $S_\Sigma(t)$ to

$$S_\Sigma(t) \simeq \frac{\Delta U_\Sigma(t)}{\Delta U_\Sigma(0)}. \tag{3.20}$$

Consequently, the mean relaxation time is given by

$$\tau_\Sigma = \frac{T}{\Delta U_\Sigma(0)}, \tag{3.21}$$

where

$$T = \int_0^\infty \Delta U_\Sigma(t)dt = \tag{3.22}$$

$$= \lim_{\omega\to 0} \frac{1}{\omega} Im\left[\frac{\Sigma(\omega)}{\Sigma(\omega)+1+\frac{\varepsilon_c}{2}}\right] = \tag{3.23}$$

$$= \lim_{\omega\to 0} \frac{1}{\omega} \frac{(1+\frac{\varepsilon_c}{2})\Sigma''(\omega)}{(\Sigma'(\omega)+1+\frac{\varepsilon_c}{2})^2+(\Sigma''(\omega))^2}. \tag{3.24}$$

With

$$\Sigma(\omega) = \varepsilon(\omega) - 1 + \frac{4\pi i\sigma(\omega)}{\omega} \tag{3.25}$$

$$\Sigma(\omega) = \Sigma'(\omega) + i\Sigma''(\omega) \tag{3.26}$$

$$\varepsilon(\omega) = \varepsilon'(\omega) + i\varepsilon''(\omega) \tag{3.27}$$

$$\sigma(\omega) = \sigma'(\omega) + i\sigma''(\omega). \tag{3.28}$$

Eq. 3.24 can be rewritten upon substitution as

$$T = \lim_{\omega\to 0} \frac{1}{\omega} Im\left[\frac{\Sigma(\omega)}{\Sigma(\omega)+1+\frac{\varepsilon_c}{2}}\right] = \tag{3.29}$$

$$= \lim_{\omega\to 0} \frac{(1+\frac{\varepsilon_c}{2})(\varepsilon''(\omega)\omega + 4\pi\sigma'(\omega))}{(\omega(\varepsilon'(\omega)+\frac{\varepsilon_c}{2}) - 4\pi\sigma''(\omega))^2 + (\omega\varepsilon''(\omega)+4\pi\sigma'(\omega))^2} \tag{3.30}$$

$$= \lim_{\omega\to 0} \frac{(1+\frac{\varepsilon_c}{2})4\pi\sigma'(\omega)}{(-4\pi\sigma''(\omega))^2 + (4\pi\sigma'(\omega))^2} \tag{3.31}$$

$$= \lim_{\omega\to 0} (1+\frac{\varepsilon_c}{2}) \frac{1}{4\pi\sigma'(\omega)} \tag{3.32}$$

$$= (1+\frac{\varepsilon_c}{2}) \frac{1}{4\pi\sigma_0}. \tag{3.33}$$

When proceeding from Eq. 3.30 to 3.31 we have omitted all terms involving $\varepsilon'(\omega)$ and $\varepsilon''(\omega)$ as they are multiplied by ω and thus vanish in the zero-frequency limit. Furthermore, $\lim_{\omega\to 0}\sigma''(\omega) = 0$.

As can be seen from Eq. 3.21, the calculation of the mean relaxation time needs both, the time integral (see. Eq. 3.22) and the amplitude $\Delta U_\Sigma(0)$. For $t = 0$ Eq. 3.18 becomes

$$\Delta U_\Sigma(0) = \frac{2}{\pi} \int_0^\infty \frac{1}{\omega} Im\left[\frac{\Sigma(\omega)}{\Sigma(\omega)+1+\frac{\varepsilon_c}{2}}\right] d\omega. \tag{3.34}$$

Following the elegant formalism described by Rips *et al.* [153], we get

$$\Delta U_\Sigma(0) = \lim_{\omega\to 0}\left[\frac{\Sigma(\omega)}{\Sigma(\omega)+1+\frac{\varepsilon_c}{2}}\right] - \lim_{\omega\to\infty}\left[\frac{\Sigma(\omega)}{\Sigma(\omega)+1+\frac{\varepsilon_c}{2}}\right] \tag{3.35}$$

Using Eqs. 3.25-3.28, the infinite-frequency limit above gives

$$\lim_{\omega\to\infty}\left[\frac{\Sigma(\omega)}{\Sigma(\omega)+1+\frac{\varepsilon_c}{2}}\right]=\frac{2(\varepsilon_\infty-1)}{2(\varepsilon_\infty-1)+\varepsilon_c+2}, \tag{3.36}$$

while the zero-frequency limit gives unity. Altogether, the amplitude becomes

$$\Delta U_\Sigma(0)=\frac{\varepsilon_c+2}{\varepsilon_c+2\varepsilon_\infty}. \tag{3.37}$$

Combining Eqs. 3.33 and 3.37 we get the mean relaxation time

$$\tau_\Sigma=\frac{T}{\Delta U_\Sigma(0)}=\frac{\varepsilon_c+2\varepsilon_\infty}{2}\frac{1}{4\pi\sigma_0}. \tag{3.38}$$

This shows that τ_Σ is determined only by three parameters, namely ε_c, σ_0 and ε_∞. ε_c characterizes the polarizability of the solute, σ_0 stands for the translational mobility of the solvent environment and ε_∞ describes the polarizability of the solvent. Although the above derivation differs in parts, we get the same analytical result for the mean relaxation time as Zhang *et al.*[122]

Using components of the dielectric spectrum to calculate the solvation response function

While experiments always yield the dielectric spectrum as an inseparable entity, except for the static conductivity σ_0, which is also accessible from other experimental methods, simulation studies offer the possibility to analyze how different components of the computational spectrum determine the shape of the solvation response function $S(t)$. For conducting systems, the hyperbola $4\pi i\sigma_0/\omega$ dominates the imaginary part of the generalized dielectric permittivity $\Sigma(\omega)$. Therefore, it is usually subtracted:

$$\Sigma_0(\omega)=\Sigma(\omega)-\frac{4\pi i\sigma_0}{\omega} \tag{3.39}$$

$$=\varepsilon(\omega)-1+\frac{4\pi i(\sigma(\omega)-\sigma_0)}{\omega}. \tag{3.40}$$

The complement $\Sigma_0(\omega)$ of the conductivity hyperbola $4\pi i\sigma_0/\omega$ is representative of the fine structure of the spectrum. Its role can be highlighted by reducing Eq. 3.18 to

$$\Delta U_{\Sigma_0}(t)=\frac{2}{\pi}\int_0^\infty\frac{cos(\omega t)}{\omega}Im\left[\frac{\Sigma_0(\omega)}{\Sigma_0(\omega)+1+\frac{\varepsilon_c}{2}}\right]d\omega. \tag{3.41}$$

The subtraction of $4\pi i\sigma_0/\omega$ corresponds to the replacement of $\sigma'(\omega)$ with $(\sigma'(\omega)-\sigma_0)$ in Eq. 3.32:

$$\int_0^\infty\Delta U_{\Sigma_0}(t)dt=\lim_{\omega\to0}(1+\frac{\varepsilon_c}{2})\frac{1}{4\pi(\sigma'(\omega)-\sigma_0)}. \tag{3.42}$$

Unfortunately, this integral diverges. In other words, the inclusion of the conductivity hyperbola is essential for this model theory.[123] Because of its fundamental role, it makes sense to

study the influence of $4\pi i\sigma_0/\omega$ separately, simplifying Eq. 3.18 to

$$\Delta U_{\sigma_0}(t) = \frac{2}{\pi}\int_0^\infty \frac{cos(\omega t)}{\omega} Im\left[\frac{\frac{4\pi i\sigma_0}{\omega}}{\frac{4\pi i\sigma_0}{\omega}+1+\frac{\varepsilon_c}{2}}\right] d\omega \tag{3.43}$$

$$= \frac{2}{\pi}\int_0^\infty cos(\omega t)\frac{T}{1+(\omega T)^2} d\omega \tag{3.44}$$

$$= e^{-t/T} \tag{3.45}$$

with the relaxation time

$$T = (1+\frac{\varepsilon_c}{2})\frac{1}{4\pi\sigma_0}. \tag{3.46}$$

In other words, the conductivity hyperbola - when taken solely - leads to a mono-exponential function. To get a more realistic $S(t)$, the logical next step is to replace the static conductivity σ_0 by its frequency-dependent analogue $\sigma(\omega)$, yielding

$$\Delta U_{\sigma}(t) = \frac{2}{\pi}\int_0^\infty \frac{cos(\omega t)}{\omega} Im\left[\frac{\frac{4\pi i\sigma(\omega)}{\omega}}{\frac{4\pi i\sigma(\omega)}{\omega}+1+\frac{\varepsilon_c}{2}}\right] d\omega, \tag{3.47}$$

representing the complete translational contribution. Referring to Eq. 3.31 it is clear that this replacement does not affect T. Thus we have shown that T is universal for all three cases discussed. The amplitudes, however, differ. Repeating the calculation in Eq. 3.35 for $4\pi i\sigma_0/\omega$ or $4\pi i\sigma(\omega)/\omega$ instead of $\Sigma(\omega)$ we get $\Delta U_{\sigma_0}(0) = \Delta U_{\sigma}(0) = 1$. Hence, the mean relaxation time for these two cases is $\tau_{\sigma_0} = \tau_{\sigma} = T$ as opposed to Eq. 3.38. We anticipate from the results shown later, that time dependence of $S_{\sigma_0}(t)$ and $S_{\sigma}(t)$ is rather different, although the respective mean relaxation times are identical.

Describing the solute using an ellipsoidal cavity

All previous expressions are based on a spherical cavity containing the solute. As the studied solute Coumarin 153 is rather anisotropic in shape it seems prudent to make the cavity anisotropic as well. Following previous works using reaction field methods with an ellipsoidal solute cavity in polar liquids,[152,154–156] we applied this approach to ionic liquids. The response function in this case is given by

$$F(\omega) = \begin{pmatrix} f_a(\omega) & 0 & 0 \\ 0 & f_b(\omega) & 0 \\ 0 & 0 & f_c(\omega) \end{pmatrix}, \tag{3.48}$$

where

$$f_i = \frac{3A_i(1-A_i)\Sigma(\omega)}{1+\Sigma(\omega)(1-A_i)},\ i = a,b,c \tag{3.49}$$

describe the response function along the three axes of the ellipsoid and A_i are ellipsoidal shape factor integrals.[154] The solvation energy is then given by

$$\Delta U(t) = -\frac{\varepsilon_c+2}{3abc}\Delta\mu\cdot\frac{2}{\pi}\int_0^\infty \frac{cos(\omega t)}{\omega} Im[F(\omega)]d\omega\cdot\Delta\mu. \tag{3.50}$$

3.2.3 Methods

The results presented here were gathered from polarizable molecular dynamics simulations of three different ionic liquids, 1-ethyl-3-methylimidazolum tetrafluoroborate ($EMIM^+BF_4^-$), 1-ethyl-3-methylimidazolum trifluoromethanesulfonate ($EMIM^+TfO^-$) and 1-butyl-3-methylimidazolum tetrafluoroborate ($BMIM^+BF_4^-$), each containing 1000 ion pairs and a single coumarin 153 (C153) molecule with a charge distribution reflecting its electronic ground state. All simulations were run at a temperature of 300K in cubic boxes with respective box lengths of 64.4Å for $EMIM^+BF_4^-$, 67.9Å for $EMIM^+TfO^-$and 68.65Å for $BMIM^+BF_4^-$using a time step of 0.5 fs. Non-bonded interactions were calculated using the Lennard-Jones potential with a switch function between 11 and 12Å and the PME method[80,81] with a real-space cut-off of 12Å and a κ of 0.41 $Å^{-1}$. The lengths of all bonds involving a hydrogen atom were held fixed by the SHAKE algorithm.[82] The charge distribution of the solvent molecules was made polarizable by adding Drude particles to all non-hydrogen atoms.[24] These simulations are the same as in Schmollngruber *et al.*[125], where more detailed information on the computational setup is given. For each system, 60 ns of trajectory data containing only coordinates and additional 15 ns of trajectory data also containing velocities were produced using the molecular dynamics package CHARMM[18]. For a quantification of the various solvation response functions we fitted them to the function

$$S(t) \approx ae^{-t/\tau_1} + (1-a)e^{-(t/\tau_2)^\beta}, \tag{3.51}$$

consisting of an exponential and a Kohlrausch-William-Watts (KWW) function.[125,127,139,149] The set of parameters is collected in Table 3.1.

3.2.4 Results and discussion

Dielectric spectra

The dielectric relaxation data shown in Fig. 3.1 was calculated from molecular dynamics simulation data following the approach used in previous work.[98] The time correlation functions of the total rotational dipole moment ($\langle \vec{M}_D(0) \cdot \vec{M}_D(t) \rangle$), the total current ($\langle \vec{J}(0) \cdot \vec{J}(t) \rangle$) and their cross-correlation function ($\langle \vec{M}_D(0) \cdot \vec{J}(t) \rangle$) were fitted using fit functions of the form

$$f(t) \approx \sum_j A_j \cdot e^{-t/\tau_j} + \sum_k A_k cos(\omega_k t + \delta_k) \cdot e^{-t/\tau_k}, \tag{3.52}$$

where $f(t)$ denotes the respective time correlation function. In order to achieve a more reliable value for the longest time constant of $\langle \vec{J}(0) \cdot \vec{J}(t) \rangle$,[98] the relationship

$$\frac{d^2}{dt^2} \langle (\Delta \vec{M}_J(t))^2 \rangle = 2 \langle \vec{J}(0) \cdot \vec{J}(t) \rangle \tag{3.53}$$

described in Schröder[157] was practically applied. As $\langle (\Delta \vec{M}_J(t))^2 \rangle$ could be calculated from the much longer coordinate trajectory, $\langle \vec{J}(0) \cdot \vec{J}(t) \rangle$ gained by calculating the second derivative using the Savitzky-Golay algorithm[105] proved to be consistent with the directly calculated

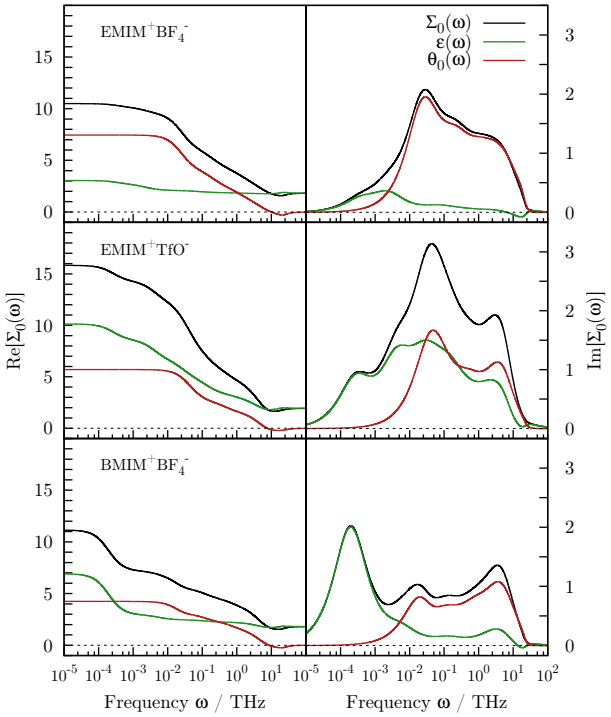

Figure 3.1 Dielectric relaxation functions (cf. Eq. 3.39) generated from MD simulation data, real (left column) and imaginary parts (right column).

correlation function (cf. Fig. S1 provided in the Supplementary Material). This provided another source for the above-mentioned longest time constant. Tables S1, S2 and S3 in the Supplementary Material list all the fit parameters used here.

Characterization of the solvation response function within the reaction field continuum model

The time dependence

As we have already learned in Eq. 3.42, the static conductivity σ_0 is of central importance when applying the reaction field continuum model (RFCM) to conducting systems. Therefore, we study its properties first. The values calculated for the three systems studied here are 0.402 S/m, 0.279 S/m and 0.069 S/m for $EMIM^+BF_4^-$, $EMIM^+TfO^-$and $BMIM^+BF_4^-$, respectively. $S_{\sigma_0}(t)$ is a mono-exponential function (see Eq. 3.45 and Fig. 3.2). This, however, does not reflect the typical two time regimes of the solvation response function in ionic liquids.

The next logical step is the full frequency-dependent conductivity $\sigma(\omega)$. In fact, this extension already generates two time regimes in the solvation response function, as can be seen in Fig. 3.2 and Table 3.1. When compared to the mono-exponential function typical for the static conductivity, $S_\sigma(t)$ already has a shape that can be modeled by the fit function Eq. 3.51. As the actual amplitudes derived from the fit are almost equal, we are facing a one-to-one mixture of an exponential and a KWW function.

With the above description, the essentials of translational motion are represented within

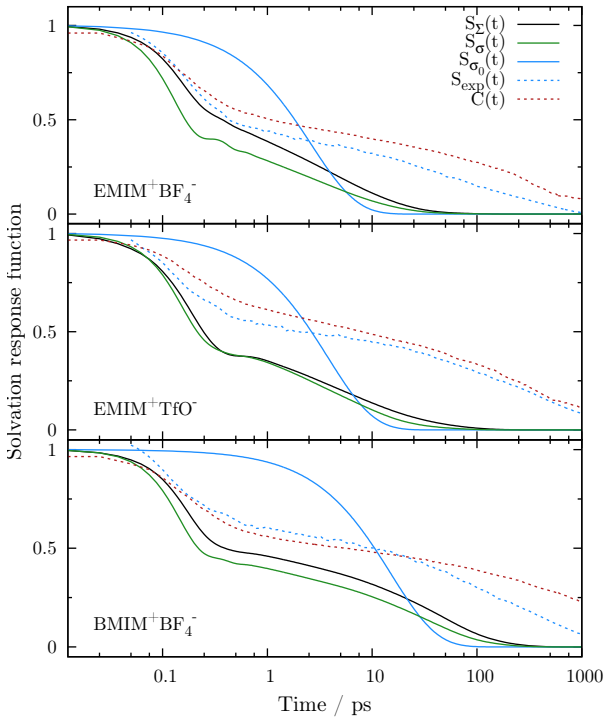

Figure 3.2 Comparison of $S_\Sigma(t)$ (black, cf. Eq. 3.18), $S_\sigma(t)$ (green, cf. Eq. 3.47), $S_{\sigma_0}(t)$ (blue, cf. Eq. 3.45), $C(t)$ (dotted red, cf. Eq. 3.58) and experimental data[123] (dotted light blue). While $S_{\sigma_0}(t)$ is a simple mono-exponential curve, $S_\sigma(t)$ already shows the typical differentiation into two distinct time domains. The addition of rotational motion in $S_\Sigma(t)$, i.e. taking whole $\Sigma(\omega)$, changes the curve only slightly. Comparison to $S_{exp}(t)$ (cf. Zhang *et al.*[123]) and $C(t)$ shows, that the solvation response function predicted by the RFCM decays too fast.

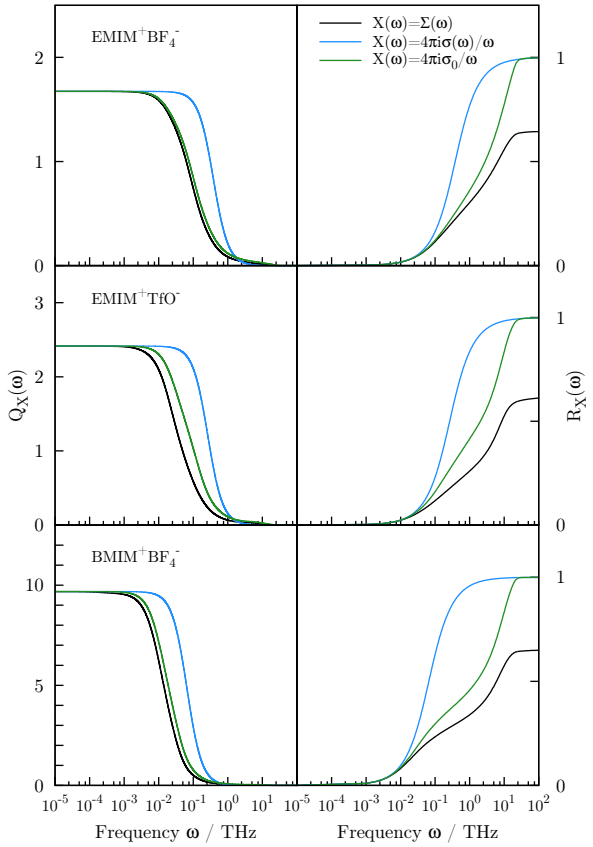

Figure 3.3 The left column shows the integrands $Q_X(\omega)$ with $X(\omega) = \{\Sigma(\omega), 4\pi i\sigma(\omega)/\omega, 4\pi i\sigma_0/\omega\}$ (cf. Eq. 3.54). The zero-frequency limit corresponds to the time integral T (see Eq. 3.22). The right column shows the running integral $R_X(\omega)$ of the corresponding curves in the left column (see Eq. 3.55). The last values of these integrals correspond to $\Delta U_X(0)$ and are the amplitudes in Eq. 3.21.

the RFCM. In order to include rotational motion, we replace $4\pi i\sigma(\omega)/\omega$ by $\Sigma(\omega)$ and use Eq. 3.18. This changes $S(t)$ quantitatively, but not qualitatively, as can be seen in Fig. 3.2 and Table 3.1. The inclusion of $\varepsilon(\omega) - 1$, i.e. the change from $S_\sigma(t)$ to $S_\Sigma(t)$, changes the fit parameters (cf. Eq. 3.51) only to a minor degree, except for the change in β in the case of $EMIM^+TfO^-$. This shows in a compact way the importance of $\varepsilon(\omega)$ for $EMIM^+TfO^-$, which is evident from its spectrum in Fig. 3.1.

The mean relaxation time

The qualitative description of the time dependence of $S(t)$ given above is now accompanied by a quantification in terms of the mean relaxation time τ (cf. Eqs. 3.21, 3.22 and 3.34). Thus, for the calculation of τ one needs the time integral of $\Delta U(t)$, which corresponds to the zero-frequency limit in Eq. 3.23, as well as the amplitude $\Delta U(0)$, given by the integral in the frequency domain (see Eq. 3.34). The respective integrand

$$Q_X(\omega) = \frac{1}{\omega}\frac{X(\omega)}{X(\omega) + 1 + \frac{\varepsilon_c}{2}} \tag{3.54}$$

and its running integral

$$R_X(\omega) = \int_0^\omega Q_X(\omega')d\omega' \tag{3.55}$$

are shown in Fig. 3.3 for the three cases $X(\omega) = \{\Sigma(\omega), 4\pi i\sigma(\omega)/\omega, 4\pi i\sigma_0/\omega\}$. The integrands in the left column of Fig. 3.3 are different, but their zero-frequency limit, i.e. the time integral T, is the same. This confirms numerically the analytical results found in Secs. 3.2.2 and 3.2.2. The running integrals $R_X(\omega)$ are shown on the right side of Fig. 3.3. Their asymptotic limits give the amplitudes $\Delta U_X(0)$. In accordance with Sec. 3.2.2, $\Delta U_{\sigma_0}(0)$ and $\Delta U_\sigma(0)$ both are unity and $\Delta U_\Sigma(0)$ can be calculated from Eq. 3.37, which can be rewritten as

$$\frac{1}{\Delta U_\Sigma(0)} = \frac{\varepsilon_c + 2\varepsilon_\infty}{\varepsilon_c + 2} = \tag{3.56}$$

$$= 1 + \frac{2(\varepsilon_\infty - 1)}{\varepsilon_c + 2}. \tag{3.57}$$

In a system consisting of non-polarizable molecules, i.e. $\varepsilon_\infty = 1$, the amplitude also becomes $1/\Delta U_\Sigma(0) = 1$. Consequently, at all three levels of complexity the mean relaxation time becomes the very same. In the present case, though, the simulations were performed with a polarizable force field characterized by the following optical dielectric constants ε_∞: 1.749 ($EMIM^+BF_4^-$), 1.906 ($EMIM^+TfO^-$) and 1.742 ($BMIM^+BF_4^-$). This leads to amplitudes lower than 1 (see Fig. 3.3) and thus enhances the mean relaxation times by about 40-50% . Inspecting Eq. 3.57 shows that only the asymptotic value of $\varepsilon(\omega)$ enters the amplitude. Thus, the complete spectrum $\varepsilon(\omega)$ is diminished by the dielectric conductivity $4\pi i\sigma(\omega)/\omega$, when considering the mean relaxation time.

The mean relaxation times of $S_{\sigma_0}(t)$ and $S_\sigma(t)$ are identical, as both, the time integral T as well as the amplitudes are equal (see Fig. 3.3). In other words, the static conductivity describes $S_\sigma(t)$ exactly on the average, but not in detail.

Comparison to simulated and experimental solvation response functions

So far, our considerations of the solvation response function were limited to the framework of the reaction field continuum theory. Now, we contrast these results with experiment[123] and simulation. In the latter case, we do not refer to the non-equilibrium simulation, but we have calculated[125] the solvation response function from equilibrium molecular dynamics (MD) simulation data as the time correlation function

$$C(t) = \frac{\langle \delta\Delta U(0)\delta\Delta U(t)\rangle}{\langle \delta\Delta U(0)^2\rangle}, \tag{3.58}$$

where $\delta\Delta U(t)$ describes the fluctuations of the solvation energy difference between the two electronic states of the solute. The results are shown in Fig. 3.2 in comparison to the triple of continuum-based functions and experimental data.[123] The pair of the directly calculated functions $C(t)$ (see Eq. 3.58) and those computed indirectly via inserting simulated dielectric spectra into the reaction field continuum model behaves much like their experimental analogues (cf. Fig. 9 of Zhang *et al.*[123]): The simple continuum model gives a solvation re-

		ε_c	σ_0/σ_0^{eff}	a	τ_1 / ps	τ_2 / ps	β	τ_X / ps
EMIM$^+$BF$_4^-$	$S_{\sigma_0}(t)$	1	σ_0	1.0	2.63	-	-	2.63
	$S_{\sigma}(t)$	1	σ_0	0.55	0.138	3.41	0.58	2.63
	$S_{\Sigma}(t)$	1	σ_0	0.42	0.189	4.27	0.58	4.08
	$S_{\Sigma}(t)$	2	σ_0	0.37	0.209	4.95	0.60	4.95
	$S_{\Sigma}(t)$	3	σ_0	0.33	0.225	5.69	0.61	5.83
	$S_{\Sigma}(t)$	1	σ_0^{eff}	0.45	0.206	9.88	0.54	9.75
	$S_{\Sigma}(t)$	2	σ_0^{eff}	0.40	0.232	11.8	0.55	11.8
	$S_{\Sigma}(t)$	3	σ_0^{eff}	0.37	0.256	13.8	0.57	13.9
	$C(t)$ [125]	-	-	0.45	0.238	217	0.40	397
	$S_{exp}(t)$ [123]	-	-	0.55	0.269	87.2	0.52	73.3
	$S_{ell}(t)$	1	σ_0	0.46	0.177	3.94	0.58	3.58
	$S_{ell}^a(t)$	1	σ_0	0.46	0.176	3.93	0.58	3.58
	$S_{ell}^b(t)$	1	σ_0	0.43	0.186	4.19	0.58	3.95
	$S_{ell}^c(t)$	1	σ_0	0.36	0.212	5.08	0.60	5.11
EMIM$^+$TfO$^-$	$S_{\sigma_0}(t)$	1	σ_0	1.0	3.79	-	-	3.79
	$S_{\sigma}(t)$	1	σ_0	0.50	0.147	4.53	0.58	3.79
	$S_{\Sigma}(t)$	1	σ_0	0.48	0.169	5.81	0.50	6.18
	$S_{\Sigma}(t)$	2	σ_0	0.43	0.187	6.59	0.51	7.44
	$S_{\Sigma}(t)$	3	σ_0	0.39	0.201	7.48	0.52	8.70
	$S_{\Sigma}(t)$	1	σ_0^{eff}	0.55	0.193	15.7	0.48	14.7
	$S_{\Sigma}(t)$	2	σ_0^{eff}	0.51	0.223	18.7	0.50	17.7
	$S_{\Sigma}(t)$	3	σ_0^{eff}	0.48	0.252	21.8	0.51	20.7
	$C(t)$ [125]	-	-	0.32	0.285	227	0.37	646
	$S_{exp}(t)$ [123]	-	-	0.45	0.233	277	0.49	317
	$S_{ell}(t)$	1	σ_0	0.52	0.158	5.44	0.49	5.48
	$S_{ell}^a(t)$	1	σ_0	0.52	0.158	5.43	0.49	5.46
	$S_{ell}^b(t)$	1	σ_0	0.49	0.167	5.71	0.50	6.00
	$S_{ell}^c(t)$	1	σ_0	0.42	0.189	6.74	0.51	7.67
BMIM$^+$BF$_4^-$	$S_{\sigma_0}(t)$	1	σ_0	1.0	15.2	-	-	15.2
	$S_{\sigma}(t)$	1	σ_0	0.58	0.161	27.6	0.68	15.2
	$S_{\Sigma}(t)$	1	σ_0	0.53	0.196	38.5	0.70	23.2
	$S_{\Sigma}(t)$	2	σ_0	0.48	0.222	43.7	0.72	28.2
	$S_{\Sigma}(t)$	3	σ_0	0.44	0.245	48.9	0.73	33.2
	$S_{\Sigma}(t)$	1	σ_0^{eff}	0.56	0.233	99.7	0.71	52.6
	$S_{\Sigma}(t)$	2	σ_0^{eff}	0.52	0.275	113	0.73	63.5
	$S_{\Sigma}(t)$	3	σ_0^{eff}	0.49	0.319	127	0.76	74.0
	$C(t)$ [125]	-	-	0.40	0.245	1260	0.31	6070
	$S_{exp}(t)$ [123]	-	-	0.38	0.266	202	0.52	233.7
	$S_{ell}(t)$	1	σ_0	0.56	0.181	35.7	0.69	20.4
	$S_{ell}^a(t)$	1	σ_0	0.56	0.181	35.6	0.69	20.3
	$S_{ell}^b(t)$	1	σ_0	0.53	0.192	37.8	0.70	22.5
	$S_{ell}^c(t)$	1	σ_0	0.47	0.226	44.7	0.72	29.1

Table 3.1 A list of all fit parameters used to describe the different variants of $S_X(t)$, $S_{exp}(t)$ and $C(t)$. The value of ε_c describes the polarizability of C153 within the RFCM (see Eq. 3.9). $\sigma_0^{eff} = \sigma_0/2.4$ denotes an effective, empirically determined[122,124,146] static conductivity. Graphical representations of the functions listed here can be found in Figs. 3.2, 3.4 and 3.6.

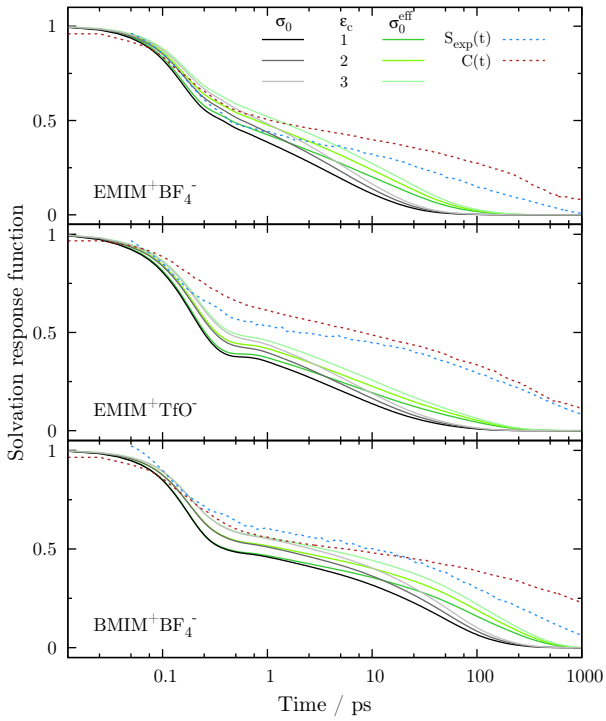

Figure 3.4 Variation of ε_c from 1 to 3 in combination with σ_0 (black curves) or $\sigma_0^{eff} = \sigma_0/2.4$ (green curves, for the factor 2.4 cf. Zhang *et al.*[122], Zhang *et al.*[146] and Liang *et al.*[124]) in comparison to results from simulation[125] (red dotted line) and experiment[123] (blue dotted line). Increasing ε_c lifts the curves mainly for short and medium times, while using σ_0^{eff} instead of σ_0 slows down the decay in the long-time domain.

sponse function with the characteristic separation into two time regimes. The fast-decaying sub-picosecond regime of the solvation response is modeled rather well for $EMIM^+BF_4^-$and $BMIM^+BF_4^-$, but not for $EMIM^+TfO^-$, while the long-time regime is decaying much too fast in all three liquids. The striking similarity of curves derived from either the experimental or computational spectra demonstrates that deviations are almost independent of the source of the dielectric spectrum, but rather show up the limitations of the reaction field continuum model. Table 3.1 lists the fit parameters used to describe the various solvation response functions calculated from the continuum model in comparison to the linear response time correlation function used in Schmollngruber *et al.*[125] and experimental data.[123]

Retarding relaxation within the framework of RFCM

Both in simulation and experiment[123,146], RFCM correctly models the dualistic shape of the solvation response function in a qualitative way. However, at the quantitative level clear deficiencies of the model theory are visible. In particular, in the long-time regime the solvation response function decays too fast. Eqs. 3.33 and 3.46 offer a possibility for retardation. The time integral T_X represents the area under the curve $\Delta U_X(t)$ and is thus proportional to the mean relaxation time. For a monotonic time function, any enhancement of its integral automatically elevates the whole curve. Therefore, the parameters ε_c and σ_0 entering T_X are a

direct route to manipulate $S(t)$ both in its shape and its integral properties. At the experimental side an effective conductivity $\sigma_0^{eff} = \frac{\sigma_0}{2.4}$ was determined for a series of ionic liquids.[122,146] In order to be consistent with these findings, we use the same scaling factor here. The results are shown in Fig. 3.4 (green curves). A further deficiency of the RFCM is the fact that structural and electrostatic properties of the solute do not enter at all, if $\varepsilon_c = 1$, meaning that the solute is not polarizable. An increase in ε_c corresponds to enhancing the polarizability of the solute. Assembling the molecular polarizability of C153 from its atomic polarizabilities according to Bica *et al.*[158] and converting it to ε_c via the Clausius-Mosotti equation we get a tentative value of $\varepsilon_c = 3$. Therefore, Fig. 3.4 shows curves for the triple $\varepsilon_c = 1,2,3$. The value $\varepsilon_c = 2$ was included, because it was used in experimental studies.[122–124,146]

As can be seen in Fig. 3.4, both, a higher ε_c as well as using σ_0^{eff} instead of σ_0 leads to an elevation of $S(t)$. However, the influence of ε_c is focused on short and medium times, while σ_0^{eff} mainly affects the long-time domain. Thus, simultaneously increasing ε_c and using σ_0^{eff} allows to manipulate $S(t)$ on the whole time scale. The best example is $BMIM^+BF_4^-$, where σ_0^{eff} combined with $\varepsilon_c = 3$ gives reasonable agreement with experimental curves. A similarly good agreement is found in the case of $EMIM^+BF_4^-$, while for $EMIM^+TfO^-$the improvement is largely confined to the initial region of $S(t)$.

Table 3.1 lists the fit parameters and mean relaxation times τ_X (last column) for $S_\Sigma(t)$ as a function of ε_c and σ_0. A stringent feature across the three liquids studied here is that the variation in ε_c and/or σ_0 primarily affects τ_2, while β and the amplitude a stays almost constant and τ_1 shows only modest change. Although numerically evaluated the mean relaxation times τ_X exactly follow Eq. 3.38. Approximately, τ_2 also follows this relation. However, this comes from the special values of parameters β and a. For the KWW part of the fit function the contribution to the mean relaxation time is given by $\langle\tau\rangle = ((1-a)/\beta)\Gamma(1/\beta)\tau_2$. If β and a are close to 0.5, as is the case for $EMIM^+BF_4^-$and $EMIM^+TfO^-$, $\tau_X \approx \tau_2$.

Linking the time behaviour of $S(t)$ with the imaginary part of the dielectric spectrum

Although usually substracted, the conductivity hyperbola $4\pi i\sigma_0/\omega$ is an essential feature of the imaginary part of the dielectric spectrum of conducting systems. Within the framework of RFCM, we have learned above in Eq. 3.42 that the conductivity hyperbola has to be included to avoid divergence of the time integral. As can be seen in Fig. 3.5 this has dramatic consequences for $Im[\Sigma(\omega)] = \Sigma''(\omega)$: In the low-frequency region of the spectrum the intrinsic part $\Sigma_0(\omega)$ is completely swamped by the hyperbola, as its values exceed those of $\Sigma_0(\omega)$ by many orders of magnitude. The effect that the peaks at low frequencies do not significantly contribute to the RFCM can also be observed in Fig. 3.3, where the integrands in the left column begin to differ only beyond a certain frequency threshold and the zero-frequency limit is determined only by the static conductivity (cf. Eqs. 3.29-3.33 and 3.46). In contrast, this is not the case in the high-frequency region of the spectrum, which is the same for $\Sigma_0(\omega)$ and $\Sigma(\omega)$. Here, the characteristic feature of the spectra of all three systems is a peak at ≈ 4 THz. In the time domain this corresponds to a relaxation time of ≈ 0.25 ps. This value is close to the τ_1 values in Table 3.1, which shows only modest variation across systems and model

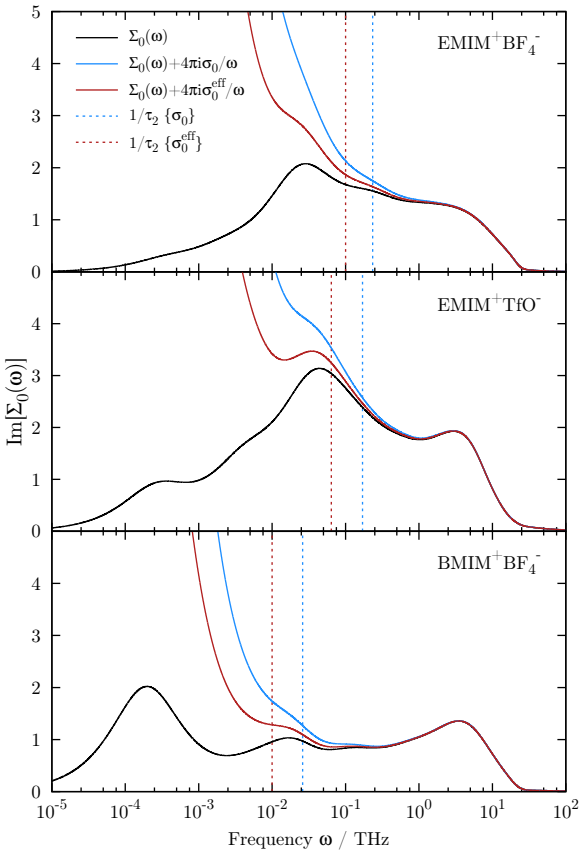

Figure 3.5 The imaginary part of $\Sigma_0(\omega)$ by itself (black curve) and after addition of the conductivity hyperbola using either the unscaled σ_0 (blue curve) or the scaled $\sigma_0^eff = \sigma_0/2.4$ (red curve). The two curves including the static conductivity diverge quickly as ω becomes smaller. The fine structure of the peaks at low frequencies ($\omega < 10^{-2}$ THz) is quickly diminished by the hyperbola, especially as this graph is plotted on a semilog scale. The vertical dotted lines mark $\omega_2 = 1/\tau_2$, when either using the unscaled conductivity σ_0 (dashed blue line) or the scaled σ_0^eff (dashed red line).

parameters.

As illustrated by Fig. 3.5 a threefold partitioning of the frequency range is possible: $\Sigma(\omega) \gg \Sigma_0(\omega)$, $\Sigma(\omega) \approx \Sigma_0(\omega)$ and $\Sigma(\omega) = \Sigma_0(\omega)$, classified low, medium and high in the following. In this medium region, the fine structure of $\Sigma_0(\omega)$ emerges to an extent depending on the value of the static conductivity. Using σ_0^{eff} instead of σ_0 shifts the medium region towards lower frequencies. Consequently, characteristic features of $\Sigma_0(\omega)$ become noticeable in $\Sigma(\omega)$. This goes along with the retardation of $S(t)$ (cf. Fig. 3.4) , which can be focused on τ_2, as we have learned above (cf. Table 3.1). We emphasize that τ_2 and (the almost constant) β from the KWW part of the fit function describe a stretched exponential representing the superposition of many exponentials. The corresponding frequency $\omega_2 = 1/\tau_2$ is given as a vertical dotted bar in Fig. 3.5 for σ_0 and σ_0^{eff} with $\varepsilon_c = 1$. In fact, ω_2 marks the beginning of the high-frequency region, where the differences between $\Sigma_0(\omega)$ and $\Sigma(\omega)$ have disappeared. When using σ_0^{eff} instead of σ_0, ω_2 shifts downwards synchronously with the conductivity hyperbola.

Taking the arguments above together, one understands why the RFCM produces reasonably good agreement in the short-time regime, while decaying too fast for longer times. In particular in the case of $EMIM^+TfO^-$, $\Sigma(\omega)$ lacks spectral information of $\Sigma_0(\omega)$ across a wide frequency range, which cannot be repaired sufficiently by rescaling σ_0. As the latter is considerably lower for $BMIM^+BF_4^-$when compared to the other two systems, a wider range of the spectrum is covered by $\Sigma(\omega)$. Therefore, in this case RFCM agrees much better with simulation and experiment.

Anisotropy in charge distribution and shape

All above considerations refer to dipolar solute enclosed in a spherical cavity. Within the RFCM the dipole moment and the radius of the sphere are, except for ε_c, the only parameters describing the solute. As they both enter as prefactors, they cancel out upon normalization. In order to include more detailed features of the solute, we modified RFCM in two ways. First, the steric anisotropy of the solute was modeled by replacing the spherical cavity with an ellipsoid,[152,156] resulting in Eq. 3.50. The principal axes of the solute were aligned with the coordinate system and a bounding box parallel to these axes was erected. This gave the relative lengths of the axes a, b and c of the ellipsoid. Subsequently, a, b and c were rescaled so that the volume of the ellipsoid equals the Voronoi volume of C153, yielding a=7.00 Å, b=4.66 Å and c=2.85 Å. The corresponding ellipsoidal shape factor integrals[154] are A_a=0.18, A_b=0.30, A_c=0.52. The change in dipole moment upon excitation $\Delta\vec{\mu}$ of the solute was projected onto the principal axes, giving the components $\Delta\mu_a$=-1.24 eÅ, $\Delta\mu_b$=0.12 eÅ, $\Delta\mu_c$=-0.02 eÅ. Since $\Delta\mu_a$ exceeds $\Delta\mu_b$ by an order of magnitude and $\Delta\mu_c$ by another one, the dipolar energy is essentially given by the prefactor $\frac{\Delta\mu_a^2}{abc}$. The only difference to the spherical cavity comes from $A_a \neq \frac{1}{3}$. As can be seen in Fig. 3.6 and Table 3.1, the deviations from the spherical model are marginal. Table 3.1 rationalizes that the a-axis of the ellipsoid essentially determines the time dependence as a whole. This comes from the fact that the a-axis and $\Delta\vec{\mu}$ are almost collinear. Thus, the solute behaves as if it were spherical.

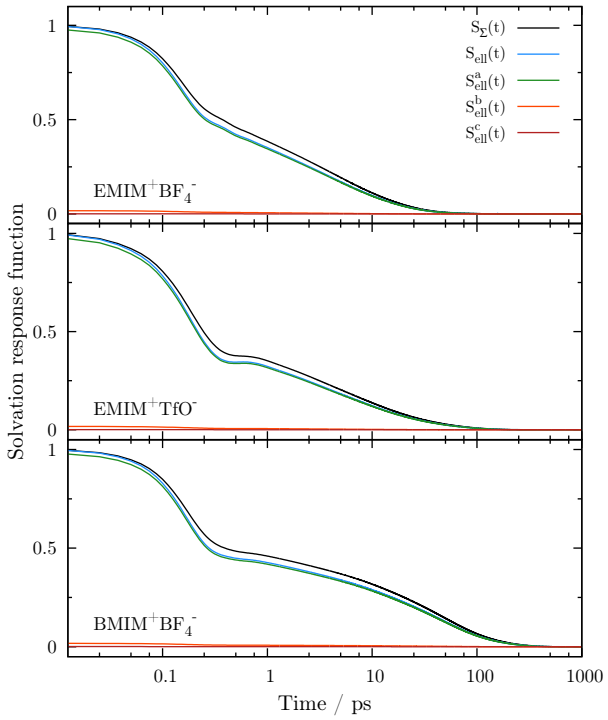

Figure 3.6 Solvation response function using the model with an ellipsoidal cavity. The black curve shows the response using a spherical cavity. The total response with an ellipsoidal cavity in blue, the contribution of principal component a in green, the contribution of principal component b in orange and the contribution of principal component c in red.

A second possibility to include anisotropic features of C153 is the inclusion of higher multipole moments of the solute in the RFCM, see Eq. 3.3. We have included the quadrupole moment, however changes were marginal as well (data not shown).

3.2.5 Conclusion

The basis of our investigations are the simulated spectra of three selected ionic liquids, $EMIM^+BF_4^-$, $EMIM^+TfO^-$and $BMIM^+BF_4^-$, differing in the relative weighting of translation (dielectric conductivity) and rotation (dielectric permittivity). As we used a polarizable force field, the behaviour at optical frequencies could be extrapolated. The simulated spectra were converted to the solvation response function $S(t)$ within the framework of the reaction field continuum model. While experiments cannot separate the contributions from translation and rotation, simulated spectra allow for a detailed analysis in this regard.

Our findings can be summarized as follows. If one would use the dielectric spectra in the usual way, i.e. without the conductivity hyperbola, the formalism of the RFCM diverges, which was shown in particular for the mean relaxation time. Therefore, inclusion of the static conductivity is essential. Taken alone, it would give a mono-exponential solvation response function. Proceeding from the static to the frequency-dependent conductivity already gives a qualitatively correct shape of $S(t)$. Taking the whole $\Sigma(\omega)$, which also includes rotation, only marginally changes the shape of the function. This shows very clearly the dominant role of the conductivity, i.e. of translational motion, a feature already encountered in previous studies.[122,123,125,146,148]

In accordance with experimental studies,[122–124,146] our simulations confirm that the RFCM predicts a too fast decay of $S(t)$ at longer times. We found that this can be traced back to a fundamental property of the dielectric bahaviour of conducting systems. In the low-frequency region of the imaginary part of $\Sigma(\omega)$ the conductivity hyperbola $4\pi i\sigma_0/\omega$ suppresses the fine structure of all other contributions represented by $\Sigma_0(\omega)$. Generally, we used a fit function comprised of a mono-exponential describing the short-time regime and a KWW function representing the long-time behaviour. The inverse $1/\tau_2$ of the KWW relaxation time marks the onset of the region of divergence between $\Sigma(\omega)$ and $\Sigma_0(\omega)$.

For non-polarizable systems, where $\varepsilon_\infty = 1$, the mean relaxation time of $S(t)$ is the very same, irrespective of the level of complexity, $4\pi i\sigma_0/\omega$, $4\pi i\sigma(\omega)/\omega$ or $\Sigma(\omega)$. It is exclusively determined by the inverse of σ_0 as well as by the value of the cavity dielectric constant ε_c. Adapting these parameters, the resulting $S(t)$ can be improved not only in its integral properties, but also in its functional shape. However, this remedy is only partially successful and depends on the system under consideration. We suggest that the extent of improvement depends on the size of that portion of the imaginary part of $\Sigma_0(\omega)$ that is suppressed by the conductivity hyperbola. In fact, for $EMIM^+TfO^-$the deviations are the lergest.

In the RFCM all parameters except for ε_c characterizing the solute cancel out upon normalization. We have tried to introduce more solute-specific features by considering the anisotropy of the solute in shape and charge distribution. The spherical cavity was replaced by an ellipsoid and the dipole moment was augmented by the quadrupole moment. However,

within the RFCM anisotropic features of the solute do not create substantial changes in $S(t)$.

Acknowledgment

Although the experimental data of M. Maroncelli and N.P. Ernsting have been published meanwhile,[123] we still gratefully acknowledge to have had them at hand prior to publication. We would like to thank the Vienna Scientific Cluster (http://www.zid.tuwien.ac.at/vsc) for the generous allocation of computer time. We are also grateful to the Austrian Science Fund FWF for funding this work in the context of Project No. P23494.

3.2.6 Supporting Information

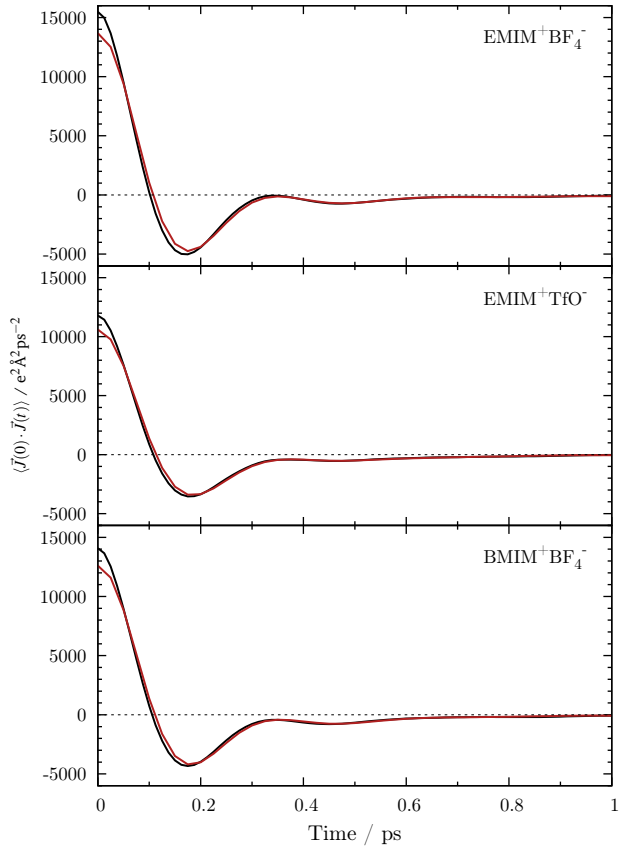

Figure 3.7 Comparison of $\langle J(0)J(t)\rangle$ (black) and $\frac{1}{2}\frac{d^2}{dt^2}\langle(\Delta M_J(t))^2\rangle$ (red). This relationship has already been shown in previous work.[44,157]

$\langle \vec{M}_D(0) \cdot \vec{M}_D(t) \rangle$	A_k	τ_k/ps	ω_k/THz	δ_k
$A_1 e^{-t/\tau_1}$	42.40	2730	–	–
$A_2 e^{-t/\tau_2}$	67.64	421	–	–
$A_3 e^{-t/\tau_3}$	8.951	21.1	–	–
$A_4 e^{-t/\tau_4}$	5.344	2.52	–	–
$A_5 e^{-t/\tau_5}$	5.332	0.400	–	–
$A_6 e^{-t/\tau_6}$	7.323	0.0660	–	–

$\langle \vec{J}(0) \cdot \vec{J}(t) \rangle$	A_k	τ_k/ps	ω_k/THz	δ_k
$A_1 cos(\omega_1 t + \delta_1) \cdot e^{-t/\tau_1}$	14200	0.121	20.159	-0.9027
$A_2 cos(\omega_2 t + \delta_2) \cdot e^{-t/\tau_2}$	406.6	0.0957	34.892	-1.890
$A_3 e^{-t/\tau_3}$	-5358	0.153	–	–
$A_4 e^{-t/\tau_4}$	-816.7	0.311	–	–
$A_5 e^{-t/\tau_5}$	11330	0.0546	–	–
$A_6 e^{-t/\tau_6}$	-139.7	0.904	–	–
$A_7 e^{-t/\tau_7}$	-8.866	4.47	–	–
$A_8 e^{-t/\tau_8}$	-0.2366	40.6	–	–

$\langle \vec{M}_D(0) \cdot \vec{J}(t) \rangle$	A_k	τ_k/ps	ω_k/THz	δ_k
$A_1 cos(\omega_1 t + \delta_1) \cdot e^{-t/\tau_1}$	359.1	0.0969	19.446	-2.375
$A_2 cos(\omega_2 t + \delta_2) \cdot e^{-t/\tau_2}$	798.1	0.0235	11.331	-1.223
$A_3 e^{-t/\tau_3}$	-1.362	10.1	–	–
$A_4 e^{-t/\tau_4}$	-12.83	0.340	–	–

Table 3.2 Table listing all fit parameters used to describe the time correlation functions underlying the dielectric relaxation data of $EMIM^+BF_4^-$.

$\langle \vec{M}_D(0) \cdot \vec{M}_D(t) \rangle$	A_k	τ_k/ps	ω_k/THz	δ_k
$A_1 e^{-t/\tau_1}$	208.6	3750	–	–
$A_2 e^{-t/\tau_2}$	220.7	36.3	–	–
$A_3 e^{-t/\tau_3}$	128.0	0.416	–	–
$A_4 e^{-t/\tau_4}$	263.2	241	–	–
$A_5 e^{-t/\tau_5}$	181.4	5.87	–	–

$\langle \vec{J}(0) \cdot \vec{J}(t) \rangle$	A_k	τ_k/ps	ω_k/THz	δ_k
$A_1 cos(\omega_1 t + \delta_1) \cdot e^{-t/\tau_1}$	7953	0.123	20.066	-0.6724
$A_2 cos(\omega_2 t + \delta_2) \cdot e^{-t/\tau_2}$	8461	0.102	11.452	-0.2029
$A_3 e^{-t/\tau_3}$	-2666	0.260	–	–
$A_4 e^{-t/\tau_4}$	-22.00	2.37	–	–
$A_5 e^{-t/\tau_5}$	-0.6411	23.8	–	–

$\langle \vec{M}_D(0) \cdot \vec{J}(t) \rangle$	A_k	τ_k/ps	ω_k/THz	δ_k
$A_1 cos(\omega_1 t + \delta_1) \cdot e^{-t/\tau_1}$	288.9	0.105	19.191	-2.486
$A_2 cos(\omega_2 t + \delta_2) \cdot e^{-t/\tau_2}$	724.6	0.184	4.0888	1.217
$A_3 cos(\omega_3 t + \delta_3) \cdot e^{-t/\tau_3}$	13.29	2.59	0.24729	-2.533
$A_4 e^{-t/\tau_4}$	-4.008	14.5	–	–

Table 3.3 Table listing all fit parameters used to describe the time correlation functions underlying the dielectric relaxation data of $EMIM^+TfO^-$.

$\langle \vec{M}_D(0) \cdot \vec{M}_D(t) \rangle$	A_k	τ_k/ps	ω_k/THz	δ_k
$A_1 e^{-t/\tau_1}$	47.52	0.316	–	–
$A_2 e^{-t/\tau_2}$	67.53	179	–	–
$A_3 e^{-t/\tau_3}$	31.53	7.51	–	–
$A_4 e^{-t/\tau_4}$	551.2	5140	–	–

$\langle \vec{J}(0) \cdot \vec{J}(t) \rangle$	A_k	τ_k/ps	ω_k/THz	δ_k
$A_1 cos(\omega_1 t + \delta_1) \cdot e^{-t/\tau_1}$	12950	0.115	20.419	-1.015
$A_2 cos(\omega_2 t + \delta_2) \cdot e^{-t/\tau_2}$	99.08	0.119	38.372	-1.937
$A_3 e^{-t/\tau_3}$	-5175	0.213	–	–
$A_4 e^{-t/\tau_4}$	-61.76	1.35	–	–
$A_5 e^{-t/\tau_5}$	11040	0.0563	–	–
$A_6 e^{-t/\tau_6}$	-1.439	9.58	–	–
$A_7 e^{-t/\tau_7}$	-0.3051	41.2	–	–
$A_8 e^{-t/\tau_8}$	0.3995	30.8	–	–

$\langle \vec{M}_D(0) \cdot \vec{J}(t) \rangle$	A_k	τ_k/ps	ω_k/THz	δ_k
$A_1 cos(\omega_1 t + \delta_1) \cdot e^{-t/\tau_1}$	236.9	0.120	19.494	-2.189
$A_2 cos(\omega_2 t + \delta_2) \cdot e^{-t/\tau_2}$	919.9	0.146	1.9590	1.420

Table 3.4 Table listing all fit parameters used to describe the time correlation functions underlying the dielectric relaxation data of $BMIM^+BF_4^-$.

3.3 Combining non-equilibrium simulations and coarse-grained modelling allows for a fine-grained decomposition of solvation dynamics

submitted to Phys. Chem. Chem. Phys. on 12 September, 2016

Michael Schmollngruber,[a] Daniel Braun[a] and Othmar Steinhauser[a]

[a] *University of Vienna, Department of Computational Biological Chemistry, Währingerstrasse 17, A-1090 Vienna, Austria*

In this work we present 4000 independent non-equilibrium molecular dynamics simulations of the time-dependent Stokes shift observed for the chromophor coumarin 153 in the ionic liquid 1-ethyl-3-methylimidazolium trifluoromethanesulfonate. The solvent is simulated using a coarse-grained model, which radically reduces computation demand, while maintaining the anisotropy of shape and charge distribution typical for ionic liquids. Using both, the high number of simulations obtainable with a coarse-grained model as well as the linearity of the non-equilibrium observable, we can study in great detail the origins of the time-dependent Stokes shift in this idealized ionic liquid system. We confirm the previously reported dominant role of the anions and show that the time scales of the relaxation processes for cations and anions are quite different. Additionally, decomposition into contributions from solvation shells defined by Voronoi tessellation shows clearly that only the first two solvation shells contribute to the total effect, while contributions from the bulk solvent almost perfectly compensate and vanish. Furthermore, this decomposition by solvation shells shows clearly that the sub-picosecond relaxation stems almost entirely from the first shell. Owing to the high statistical accuracy, the total Stokes shift can be resolved into contributions from individual solute atoms. This reveals that only 9 out of 36 atoms of coumarin 153 yield significant individual contributions. Even more, two atoms comprise 90% of the total signal.

3.3.1 Introduction

The study of solvation phenomena has attracted increased interest in recent years. Gaining a deeper understanding of the intricate interactions between a solute and a solvent, and how the two influence each other, is of paramount importance in many fields of research. In the course of this renewed flare of interest, ionic liquids (IL),[1,2] a novel class of solvents, have risen to prominence. These solvents consist of ionic organic molecules and are liquid at room temperature. Due to their favorable properties,[1,2] they lend themselves as solvents to a wide array of applications. A more thorough understanding of the solvation properties of IL can further still improve our capability to design solvents for specific tasks.

The dynamical capacity of a solvent can be measured in various ways. One that is often used is the time-dependent Stokes shift (TDSS), which is observed as the time evolution of the fluorescence peak after electronic excitation of a solute. This shift in frequency is brought about by a reorganization of the solvent molecules surrounding the solute. In this way, the solute chromophor acts as a local probe to measure solvent properties. An often used chromophor used in studies of the TDSS is coumarin 153 (C153).[45,101,120–125,142,159]

Several studies of the TDSS in ionic liquids, experimental as well as computational, have been performed.[45,121–124,133–136,138–148,160] Most of the computational studies are based on equilibrium simulations, from which the TDSS can be deduced in the spirit of linear response theory.[130]

Non-equilibrium MD simulations of solvation dynamics directly model how the solvent molecules around the chromophor probe react after an electronic excitation of the chromophor. Within the limits of classical MD simulations, the electronic excitation of the chromophor is modeled by a sudden change in the partial charge distribution of the chromophor molecule. As this technique allows for an immediate monitoring of the dynamical processes in the solution without the need to resort to linear response theory, it can be used to study the molecular mechanics behind the observed solvation dynamics directly. However, it comes with the downside of a more complicated simulation setup and usually also with the need to perform many independent replica simulations of the relaxation process in order to achieve the necessary statistical accuracy. This explains why only a few non-equilibrium simulations of the TDSS in ionic liquids exist.[138,140,160] One way to cope with the high computational demands associated with non-equilibrium simulations is to use coarse-grained (CG) modelling, *i.e.* the simplification of a fully atomistic model by uniting groups of atoms or even higher-scale features. To our knowledge, there has so far been only one study of non-equilibrium simulations of the TDSS using a coarse-grained model of an ionic liquid solvent.[160]

In this work we present a computational study of the TDSS, based on 4000 independent non-equilibrium simulations in a united-atom CG model of the ionic liquid 1-ethyl-3-methylimidazolium trifluoromethanesulfonate ($EMIM^+$ OTf^-). The self-developed CG model used here[161] was designed to preserve the anisotropy in shape and charge distribution, which is constitutive for ionic liquids. By exploiting the linearity of Coulombic solvation energies as well as of the non-equilibrium scheme as such, we can decompose the total observed TDSS in various ways, concerning both the solvent and the solute.

3.3.2 Methods

In this work we present 4000 independent MD simulations of coumarin 153 (C153) solvated in 1000 ion pairs of $EMIM^+$ OTf^-. The force fields of C153 [101,125,159] as well as the coarse-grained (CG) force field of $EMIM^+$ OTf^- [161] were already used in previous studies. This particular CG model follows a united-atom approach (cf. Fig. 1 in Braun and Steinhauser [161]), resulting in a radically reduced number of atoms, while still retaining the essential characteristics of the original fully atomistic model. This reduced computational effort allowed for the simulation of 4000 independent replica systems within a reasonable time frame. As ionic liquids are often more viscous than conventional polar solvents (cf. Tab. 1.1), typical relaxation times of solvation dynamics lie in the range of nanoseconds. This combined demand to perform a large number of independent simulations, each of which needs to reach a sufficiently long simulated time, makes the choice of a coarse-grained model for the solvent particularly efficient.

The non-equilibrium simulations have been conducted using the following protocol. First, each independent starting configuration was assembled using the program PACKMOL[79], followed by a steepest descent energy minimization using the molecular dynamics simulation program CHARMM,[18] which was used for all simulations presented here. After a 1 ns equilibration run using an NpT ensemble each system was set to the same average box size and further equilibrated for 2 ns in an NVT ensemble. Up to this point, the partial charge distribution of C153 corresponded to the S_0 state. The electronic excitation of C153 was simulated by abruptly changing the partial charge distribution to correspond to the first excited state S_1. After this change, each simulation was continued from the last configuration of the corresponding equilibration run for another 2 ns in an NVT ensemble. It should be noted that the temperature was held fixed at 300 K using the Nosé-Hoover thermostat [162–164] during the complete simulation time. The systems were simulated with period boundary conditions in a cubic box. Electrostatic interactions were calculated using the particle mesh Ewald algorithm [80,81] with splines of order 6, a grid spacing of about 1 Å and a κ of 0.41 $Å^{-1}$. All bond lengths were kept at constant length using the SHAKE algorithm.[82] All trajectory analysis was done using a modified version of MDAnalysis.[92] Solvation shell decomposition was done by Voronoi tessellation with the Voro++ library.[93]

In experiment, solvation dynamics is characterized by the normalized time-dependent Stokes shift

$$S(t) = \frac{\nu(t) - \nu(\infty)}{\nu(0) - \nu(\infty)} \tag{3.59}$$

of the transient peak frequency $\nu(t)$ of the fluorescence signal. The observed frequency corresponds to an energy difference

$$\Delta E(t) = h\nu(t) \approx h\nu_{\mathrm{vac}} + \Delta U(t), \tag{3.60}$$

where h is the Planck constant, $h\nu_{\mathrm{vac}}$ is the energy difference of the ground and excited electronic states of the solute in vacuum - which can be approximated as being constant by omitting internal relaxation mechanisms - and $\Delta U(t)$ is the difference in the solvation

energies of the two states. Combining Eqs. 3.59 and 3.60, one can describe the Stokes shift via the relaxation of $\Delta U(t)$

$$S(t) = \frac{\overline{\Delta U(t)} - \overline{\Delta U(\infty)}}{\overline{\Delta U(0)} - \overline{\Delta U(\infty)}}. \tag{3.61}$$

Here, the overlines indicate the ensemble average, which in the case of non-equilibrium simulations is achieved by averaging over replica. Usually, $\Delta U(t)$ is approximated as the change in electrostatic interaction of solute and solvent

$$\Delta U(t) = \sum_{i\alpha}\sum_{j\beta} \Delta U_{i\alpha,j\beta}(t) = \sum_{i\alpha}\sum_{j\beta} \frac{\Delta q_{i\alpha} \cdot q_{j\beta}}{\mid \vec{r}_{i\alpha}(t) - \vec{r}_{j\beta}(t) \mid}. \tag{3.62}$$

Here, $\vec{r}_{i\alpha}(t)$ and $\vec{r}_{j\beta}(t)$ are the positions of the atom α within a solute molecule i and of the atom β within a solvent molecule j, respectively. Accordingly, $\Delta q_{i\alpha}$ is the change in atomic partial charges between ground and excited electronic state and the $q_{j\beta}$ are the partial charges of the solvent atoms. Combining Eqs. 3.61 and 3.62, $S(t)$ can be rewritten as a sum of contributions from individual atom pairs

$$S(t) = \sum_{i\alpha}\sum_{j\beta} \frac{\overline{\Delta U_{i\alpha,j\beta}(t)} - \overline{\Delta U_{i\alpha,j\beta}(\infty)}}{\overline{\Delta U(0)} - \overline{\Delta U(\infty)}}, \tag{3.63}$$

thereby leaving the denominator unresolved to preserve additivity.

We now exploit this additivity to group atom pairs in various ways to decompose $S(t)$ and thus facilitate interpretation. The most intuitive decomposition in an ionic liquid is to group solvent molecules into cations and ions and taking the solute as a whole, giving

$$S(t) = S^{+}(t) + S^{-}(t). \tag{3.64}$$

Alternatively, solvent molecules may be grouped in solvation shells defined by Voronoi tessellation,[96] leading to a decomposition

$$S(t) = S^{1}(t) + S^{2}(t) + S^{\text{bulk}}(t). \tag{3.65}$$

Finally, we explore the fully atomistic resolution of the solute, giving

$$S(t) = \sum_{\alpha} S_{\alpha}(t). \tag{3.66}$$

Inherent to all the above ways of decomposing $S(t)$ is that the amplitude of each component function gives its relative weight, since all component weights add up to 1. The dynamical behaviour of the component functions is characterized by a fit to the model function

$$S(t) \approx a_G\, e^{-(t/\tau_G)^2} + a_K\, e^{-(t/\tau_K)^{\beta}}, \tag{3.67}$$

which is comprised of a Gaussian describing the inertial short-time behaviour and a Kohlrausch-William-Watts (KWW) function describing the stretched exponential long-time relax-

Function	$S^*(0)$	a_G	τ_G [ps]	a_K	τ_K [ps]	β	$\langle\tau_K\rangle$ [ps]
$S(t)$	1.0	0.55	0.14	0.45	77.9	0.45	192
$S^+(t)$	0.26	0.14	0.09	0.12	39.7	0.45	96.8
$S^-(t)$	0.74	0.42	0.17	0.32	106	0.48	228
$S^1(t)$	0.87	0.51	0.14	0.36	47.3	0.42	138
$S^2(t)$	0.13	0	-	0.13	189	0.57	305
$S^{\text{bulk}}(t)$	-0.002	0.028	0.12	-0.030	42.4	0.37	183

Table 3.5 Fit parameters for the total TDSS and its various solvent-wise decompositions according to Eq. 3.67. The second column marked with $S^*(0)$ shows the initial value of each respective component function, *i.e.* the relative contribution of that component to the total solvation energy difference.

ation.[122] The sum of the amplitudes is kept fixed during the fitting process so that $a_G + a_K = S(0)$. An average relaxation time $\langle\tau_K\rangle$ for the KWW part can be calculated by

$$\langle\tau_K\rangle = \frac{\tau_K}{\beta}\Gamma\left(\frac{1}{\beta}\right), \tag{3.68}$$

where $\Gamma(\dots)$ is the gamma function.

Instead of grouping solvent molecules as described above, one can also radially resolve $S(t)$ as

$$S(t) = \lim_{R\to\infty} S(R,t) \tag{3.69}$$

$$S(R,t) = \int_0^R S(r,t)dr, \tag{3.70}$$

where

$$S(r,t) = \frac{\overline{\Delta U(r,t)} - \overline{\Delta U(r,\infty)}}{\overline{\Delta U(0)} - \overline{\Delta U(\infty)}}. \tag{3.71}$$

Here, the distance r is the atomic pair-wise distance entering the denominator in Eq. 3.62. As such, $S(r,t)$ shows the radial resolution of the difference in solvation energies between time t and the fully relaxed steady state.

3.3.3 Results and Discussion

Prior to the component analysis described above, we compare our computational total $S(t)$ to experimental data[122] (see Fig. 3.8). We find satisfying qualitative agreement in that our model correctly reproduces the double time regime of the relaxation process, comprising the fast sub-picosecond decay attributed to inertial motion as well as the stretched exponential long time behaviour.[122] Despite of using a CG model naturally lacking details, the quantitative deviation from experiment is in the order of one magnitude, which is in line with previous studies.[125] Therefore, our subsequent component analysis seems to be well-based.

A first way of decomposing $S(t)$ is to separate contributions from cations and anions following Eqs. 3.64 and 3.63. The respective component functions are shown in Fig. 3.8.

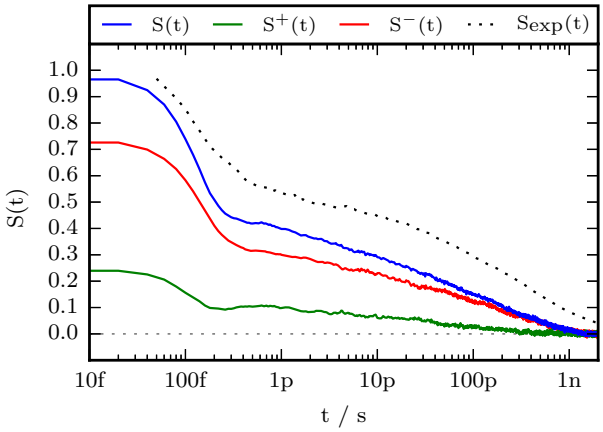

Figure 3.8 A comparison of the complete computational $S(t)$ (blue) to experimental data[122] (black dotted line). Additionally, the green and red lines show the decomposition of the total $S(t)$ into contributions from cations and anions, respectively.

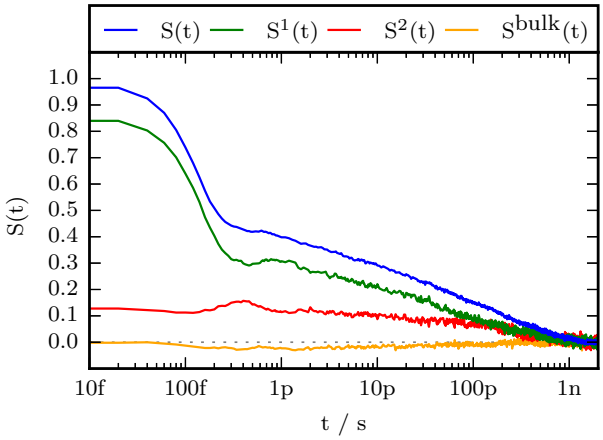

Figure 3.9 The total $S(t)$ (blue) is decomposed according to solvation shells defined by Voronoi tessellation. Shown are contributions from the first (green) and second (red) shells as well as the bulk solvent (yellow).

The contribution of the anions is thrice that of the cations, with the exact values being shown in Tab. 3.5. This is in accordance with the dominant role of the anions reported in the literature.[138,148,160] The relaxation behaviour of these functions can be represented by fitting to the model function in Eq. 3.67. The resulting parameters are shown in Tab. 3.5. We first compare the amplitudes a_G and a_K of the two relaxation mechanisms. For both, a_G as well as a_K, the ratio of anions to cations is approximately three to one. This means that $S^+(t)$ and $S^-(t)$ are composed of inertial decay and long-time relaxation in equal parts. However, the relaxation times of cations and anions are quite different, with the relaxation time of the anions being more than double that of the cations.

Grouping the solvent molecules into solvation shells around C153 defined by Voronoi tessellation we can decompose $S(t)$ into contributions from the first two solvation shells and the bulk according to Eqs. 3.65 and 3.63. The resulting component functions are shown in Fig. 3.9 and the corresponding fit parameters to Eq. 3.67 are given in Tab. 3.5. The

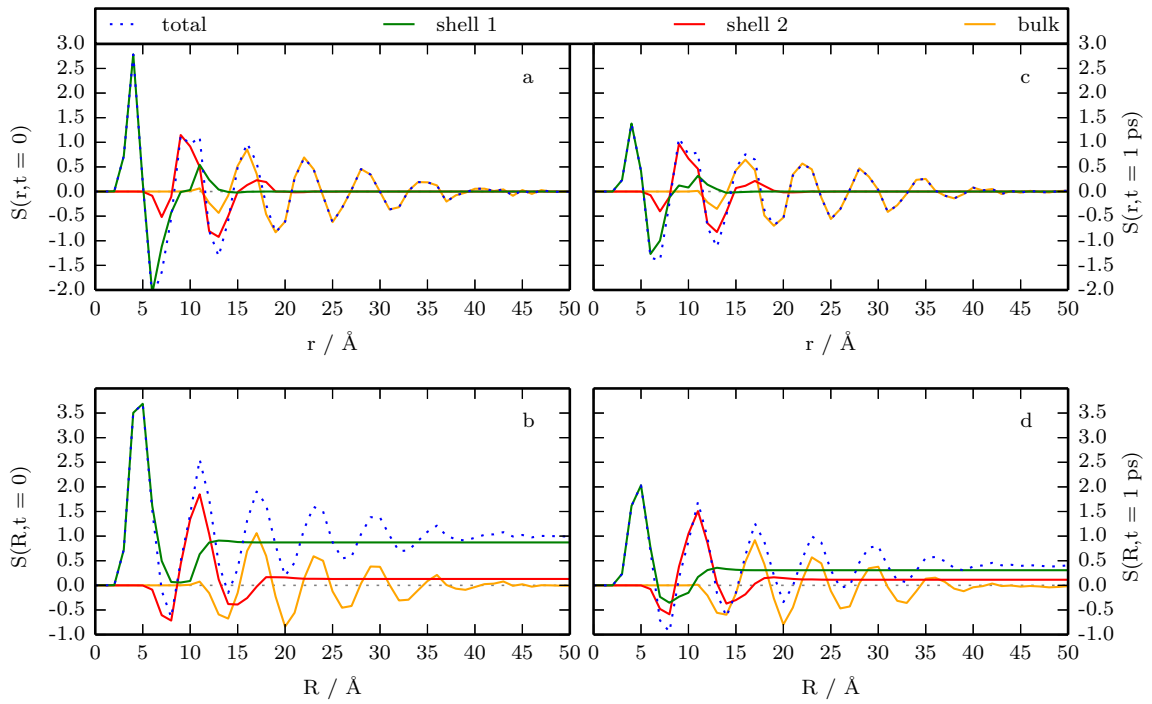

Figure 3.10 The full radial resolution of the TDSS following Eqs. 3.69 - 3.71 is shown for the two times t = 0 (panel a) and t = 1 ps (panel c). The latter time was chosen, as it shows the radial distribution of contributions to the TDSS after the sub-picosecond relaxation processes are over. Shown in panels b and d are the respective integral properties $S(R,t)$ for times t = 0 and t = 1 ps, respectively, which shows the radial convergence to the final contribution. The total function is shown as a dotted blue line. Additionally, contributions from the first (green) and second (red) solvation shells as well as the bulk solvent (yellow) as defined by Voronoi tessellation are shown.

respective amplitudes of $S^1(t)$ and $S^2(t)$ are 0.87 and 0.13, while the bulk contribution is completely marginal. The net contribution of the first shell of 0.87 can be further split into 0.51 for the short-time regime a_G and 0.36 for the long-time regime a_K. In stark contrast, the second shell completely lacks the short-time regime and is described solely by long-time relaxation. This shows in a clear and unambiguous way the almost exclusively short-range nature of the short time regime, that has been proposed previously.[143,160] Additionally, the relaxation time of $S^2(t)$ is substantially longer then that of $S^1(t)$. Taking both facts together, there appears to be a time delay in the relaxation of the second shell.

A natural spatial resolution of the TDSS into spherical shells is accomplished following Eqs. 3.69 - 3.71. The resulting $S(r,t)$ and its running integral $S(R,t)$ are shown in Fig. 3.10 at two different times $t = 0$ and $t = 1$ ps. This latter time was chosen, because then the initial fast time regime is over. We emphasize that $S(r,t)$ shows the spatial origins of the energy differences that contribute to the Stokes shift. Furthermore, Fig. 3.10 shows a decomposition of $S(r,t)$ and $S(R,t)$ into solvation shells around C153. The asymptotic limits of $S(R,t = 0)$ for the total function as well as the components from the first and second solvation shell and the bulk solvent correspond to the respective contributions to $S(t = 0)$ as shown in Tab. 3.5.

Panels a and b of Fig. 3.10 show the maximum radially resolved excess value of the solvation energy, which is found at time t=0. Panel a shows that relaxation processes extend far

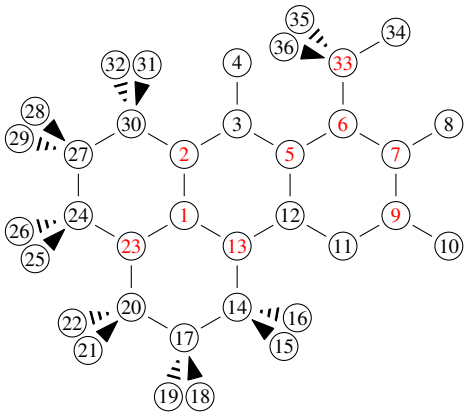

Figure 3.11 A schematic drawing of C153 with numbered atoms. The atoms marked in red are those with significant individual contributions to the Stokes shift as listed in Tab. 3.6.

Atom	Δq_α	$S_\alpha(0)$	$a_{G,\alpha}$	$\tau_{G,\alpha}$ [ps]	$a_{K,\alpha}$	$\tau_{K,\alpha}$ [ps]	β_α	$\langle\tau_{K,\alpha}\rangle$ [ps]
C1	-0.14	-0.18	-0.092	0.15	-0.090	136	0.54	240
C2	0.11	0.097	0.047	0.14	0.050	145	0.55	249
C5	0.29	-0.21	-0.11	0.17	-0.10	17.9	0.31	139
C6	-0.28	0.50	0.27	0.15	0.23	67.6	0.42	201
C7	-0.094	0.21	0.11	0.14	0.094	72.3	0.42	210
C9	-0.053	0.091	0.050	0.13	0.041	62.8	0.40	214
C13	0.067	0.050	0.025	0.15	0.025	182	0.63	257
N23	0.22	0.40	0.22	0.14	0.18	83.1	0.48	178
C33	0.037	-0.062	-0.036	0.14	-0.026	72.9	0.44	189

Table 3.6 Atom-resolved contributions to the Stokes shift $S(t)$. Shown here are only the atoms, which contribute more than five percent to the complete Stokes shift, taken in absolute numbers. Please see Fig. 3.11 for a schematic drawing of C153 with numbered atoms, where the atoms listed here are marked in red. The partial charge differences Δq_α of C153 shown here are taken from Hongping *et al.*[159].

into the solvent. However, panel b shows that only the first two solvation shells contribute to the observed Stokes shift. The reason for this is that the solvent molecules beyond the second solvation shell are structured in such a way that the radially resolved excess value cancels almost exactly upon integration, leading to $S^{\text{bulk}}(0) \approx 0$. In other words, not the relaxation processes are short-ranged, but their net contribution to the Stokes shift is. It is a well-known feature of Coulomb sums that their convergence depends on the way of summation.[165] While a simple radial resolution faces a sequence of charge layers of alternating sign, a subsummation of particles into relatively broad Voronoi shells mitigates this convergence problem by mixing charge layers of different sign.

Panels c and d of Fig. 3.10 illustrate that the reduction of the excess value in time happens non-uniformly: after 1 ps of relaxation, the excess value in the first solvation shell has reduced dramatically, while the other shells remain largely unchanged. This reduction in the first shell corresponds to the 51% of the total Stokes shift that stem from the short-time regime (cf. Fig. 3.9 and Tab. 3.5). This clearly demonstrates the short-range nature of the short-time regime.

Having focused so far on the decomposition of solvent contributions in various ways, we

now turn to an atomic resolution of the solute itself. In order to facilitate interpretation, we have selected only those nine solute atoms that contribute at least 5% to the Stokes shift, taken in absolute numbers. They are labelled in red in Fig. 3.11. We note that this set of solute atoms is also characterized by a significant Δq_α. Corresponding atom-resolved component functions of the Stokes shift are represented by a fit to Eq. 3.67, with the parameters being shown in Tab. 3.6. The contributions of individual atoms are quite diverse. Following Eq. 3.62 the contribution to the Stokes shift depends on both, the partial charge difference Δq_α as well as its environment. Thus it is not surprising that Δq_α and $S_\alpha(0)$ are not strictly correlated. Nevertheless, an atom with a marginal Δq_α cannot contribute to $S(t)$ at all. This leads to a grouping of solute atoms into three sets: the two dominating atoms C6 and N23, together comprising 90% of the total Stokes shift; the remaining seven atoms with significant contributions and the remaining atoms with very little individual contributions, which nevertheless sum up to 10%. The contributions from the atoms in the second set, though significant, add up to zero. This implies that for some atoms the interaction with their respective environments becomes less favorable, resulting in a negative contribution to the TDSS.

In terms of the atom-resolved solvation dynamics, the findings for the total Stokes shift shown in Tab. 3.5 apply at least partly. In fact, for the nine atoms shown in Tab. 3.6 the two time regimes are again weighted equally, reflecting the 1:1 weighting of the total $S(t)$ already seen in Tab. 3.5. For the inertial region even the relaxation times are quite uniform. In the long time regime the spread in $\tau_{K,\alpha}$ and β_α is considerable. However, when combined to an average relaxation time $\langle \tau_{K,\alpha} \rangle$ (see Eq. 3.68), the spread in relaxation times reduces to a maximum factor of 2. We observe that the $\langle \tau_{K,\alpha} \rangle$ of the two dominating atoms C6 and N23 is close to the amplitude-weighted average value.

3.3.4 Conclusion

This study is based on the combination of non-equilibrium simulations of solvation dynamics and the additive nature of Coulombic interactions. We have shown that this combination can be exploited to obtain a detailed and manifold decomposition of the Stokes shift, both for the solute and the solvent. In principle, this approach would be feasible for fully atomistic simulations as well. In practice, however, the high demands on statistical accuracy and consequently the high computational effort favour coarse-grained modelling. In this way, the Stokes shift can be resolved even up to individual solute atoms. As a model system we have chosen the chromophor coumarin 153 in the ionic liquid $EMIM^+$ OTf^- and have carried out 4000 independent non-equilibrium simulations.

As a first finding, we show that the initial sub-picosecond relaxation accounts for half the total observed Stokes shift in our test system. Resolution by solvation shells reveals that this contribution stems solely from the first solvation shell. The long time regime is split into contributions from the first and second solvation shells in the ratio of 3:1, with the relaxation time of the second shell also being more than double that of the first shell. The surrounding bulk solvent beyond the second shell is found to yield no net effect. However, a radial resolution shows clearly that this vanishing net effect of the bulk is brought about

by an almost perfect compensation of rather long-ranged radial shells. Separation of the contributions from ionic species confirms the dominating role of the anions in the Stokes shift. For our system we find a ratio of anionic and cationic contributions of 3:1, where both time regimes are equally weighted. The relaxation time of the cationic part of the Stokes shift is less than half that of the anionic part. However, the overall relaxation time is almost that of anionic part due to its larger amplitude, meaning that $S(t)$ largely resembles $S^{-}(t)$.

Decomposing the solute into individual atoms reveals that the solute atoms can be grouped into three sets, depending on their net contribution to the Stokes shift. Two atoms, C6 and N23, already comprise 90% of the total Stokes shift. Further seven atoms yield significant contributions, but these add up to zero. The remaining 10% stem from small contributions from the other atoms. Although there is little quantitative correlation, only those atoms with high partial charge differences Δq_α actually contribute to the Stokes shift. In the short time regime dynamics is fairly homogeneous across all atoms. We observe some spread in the long time regime.

In our test system the Stokes shift is found to be a local effect in a double sense: it is confined to the first two solvation shells and furthermore stems overwhelmingly from a few select atoms. This largely short-ranged nature we find in our test system raises the question, to what extent the time-dependent Stokes shift actually measures bulk solvent properties. There certainly is no general answer to this question, as it depends on the way the presence of the solute alone changes the local composition and dynamics of the solvent. Nevertheless, further studies could shed more light on this question.

Acknowledgement

We thankfully acknowledge the funding of this work by the Austrian Science Fund (FWF) through the project P23494.

4 The influence of different polarizability models on structure and dynamics of ionic liquids in classical MD simulations

4.1 Overview

Classical MD simulations of ionic liquids have been shown to yield dynamics substantially slower than in experiment, caused by strong electrostatic interactions. The inclusion of a model of electronic polarizability can be a remedy for this by dampening electrostatics and thereby making the system more fluid,[24] bringing simulation results closer to experiment. The two publications presented in this Chapter are methodical studies of the different polarizability models available.

When running MD simulations including atomic polarizabilities one can encounter a phenomenon termed the "polarization catastrophe". It occurs in two inducible dipoles at very short distances. These two dipoles induce each other to ever greater magnitude up to the point, where the simulation crashes. In order to avoid this unphysical behaviour, Thole suggested[43] three different dampening functions for use at short ranges. In the publication presented in Sec. 4.2 the influence of the choice of Thole function on simulation results is studied in detail for structural as well as dynamical properties.

Another choice one has is which polarizability model to use out of the three mainly used ones: Drude oscillators, induced point-dipoles and the fluctuating charge model. The publication presented in Sec. 4.3 is a detailed comparative analysis of Drude oscillators, as implemented in CHARMM, and induced point-dipoles, as implemented in AMBER. Using the same force field (apart from the polarizability model) in both programs, simulations have been carried out at varying strengths of atomic polarizability to study the effects on structural and dynamical properties.

4.2 The effect of Thole functions on the simulation of ionic liquids with point induced dipoles at various densities

J. Chem. Phys., ***138****, 204119 (2013)*

Thomas Taylor, [a] Michael Schmollngruber,[a] Christian Schröder,[a] and Othmar Steinhauser[a]

[a] *University of Vienna, Department of Computational Biological Chemistry, Währingerstrasse 17, A-1090 Vienna, Austria*

Point-induced dipoles are used to mimic electronic degrees of freedom in molecular dynamics simulations. Ultrashort distance interactions of these induced dipoles are damped by so-called Thole functions to avoid the "polarization catastrophe". This study aims at the overall impact of Thole functions on structure as well as single-particle and collective dynamics of the ionic liquid 1-ethyl-3-methylimidazolium trifluoromethylsulfonate and thereby extends common studies of the effect of Thole functions on energy minimized geometries.

4.2.1 Introduction

The last decade has seen a diversity of classical molecular dynamics (MD) simulations of ionic liquids based on force fields with permanent charges.[166,167] In particular, imidazolium-based ionic liquids attracted the most computational interest since much experimental data exist. For example, the self-aggregation of alkyl side chains has been reported from x-ray experiments[168,169] and by MD simulations.[170–172] Urahata *et al.* confirmed the experimentally suggested preferred anion positions near the imidazolium ring as a function of the side chains.[173] The most prominent and successful force field of this era was proposed by Pádua and Canongia Lopes,[174,175] which is also the basis of this work.

Experience has shown that permanent charges alone create forces that are too directional: For example, the local structure of an imidazolium ring and the first CH_2-unit attached to the nitrogens is almost rigid. Consequently, the electrostatic potential of a central imidazolium i with fixed partial charges $q_{i\beta}$ produces a jagged energy surface of more or less deep valleys forcing surrounding ions in particular positions. Moreover, these energetic valleys are preserved when when switching from one molecule i of a species to another although the corresponding environments between the two molecules may differ significantly and consequently the local electric field around these molecules. As a result, these systems are too structured and their dynamics is retarded.[24,27,167,176–179] As a first remedy, several groups reduced the partial charges, resulting in a non-integer molecular charge of less than $\pm$ 1 e, making the energetic valleys more shallow and accelerating the dynamics.[180–188] However, the problem of the prefabricated favorable positions remains in these classical MD simulations.

This problem can be solved by transient reorganization of the molecular charge distribution. In principle, ab initio methods inherently include the electronic degrees of freedom and allow for a flexible charge distribution as a function of the local environment but these methods suffer from their extremely high computational effort. As a result, the number of ion pairs is restricted to less than 100 and the trajectory period to less than a hundred picoseconds.[194–197] Unfortunately, such small systems are prone to considerable size effects[17] and may not represent a liquid but an ionic cluster. However, techniques to mimic charge reorganization with acceptable numerical effort have been developed in the literature.[198] The most prominent examples are fluctuating charges,[35,36,38] Drude oscillators (charge on a spring

Research group	Model	Minimization	MD
Schröder and Steinhauser[19,24,25,157]	Drudes	LAG	CHARMM[189]
Voth and Knox[27–30]	PID[i]	LAG	DL POLY[190]
Chang and Dang[31]	PID	SCF	
Borodin[32,34,191]	PID	SCF	Lucretius[192]
this work	PID	LAG	AMBER[193]

Table 4.1 Overview of polarizable simulation in ionic liquids. The polarization forces can be treated either by a self-consistent field (SCF) or by a Lagrangian (LAG) approach.

[i] Although standard DL POLY does not offer a PID model, Voth and Knox seemed to have a self-contained version using PID.[29]

model)[20–25] and point induced dipoles (PID).[27–32,34,191] In principle, all these polarizable models are available in the standard MD package CHARMM,[189] but only the Drude oscillator model is currently supported. Unfortunately, the interaction between point-induced dipoles in CHARMM (c37b1) is simply cut beyond the cut-off radius. The standard MD packages GROMACS[199] and DL POLY[190] provide a Drude oscillator model for polarization, whereas AMBER[193] favors PID. Polarizable simulations of ionic liquids are usually on the basis of point-induced dipoles as visible in Table 4.1. Only our group uses Drude oscillators as well which are more common in protein force fields.

To our best knowledge, AMBER is the only prominent MD program offering several types of Thole functions to damp induced dipolar interaction at short distances.[43] In order to test this set, we will stick to AMBER in this work. Thereby, our goal is not to optimize the existing non-polar force field[174,175] for 1-ethyl-3-methylimidazolium ($EMIM^+$) trifluoromethylsulfonate (TfO^-) by optimization of polarizabilities and a reparametrization of the Lennard-Jones Parameter afterwards, but monitoring structural and dynamical changes using various Thole functions and standard polarizabilities.[200] To our best knowledge, this is the first study to investigate the effect of Thole functions during simulation and not from energy minimized structures.[43,200–202]

4.2.2 Theory

Point-induced dipole model

The point-induced dipole method augments the standard set of coordinates $\{\mathbf{r}_\beta\}$ (representative of the nuclear degrees of freedom) by a set of atomic dipoles $\{\boldsymbol{\mu}_\beta^{\mathrm{ind}}\}$ which are intended to represent the electronic degrees of freedom. Consequently, the potential energy of the classical force field $U^{\mathrm{nuc}}(\{\mathbf{r}_\beta\})$ is augmented by a polarizable contribution $U^{\mathrm{pol}}(\{\mathbf{r}_\beta\},\{\boldsymbol{\mu}_\beta^{\mathrm{ind}}\})$:

$$\begin{aligned} U^{\mathrm{pol}}(\{\mathbf{r}_\beta\},\{\boldsymbol{\mu}_\beta^{\mathrm{ind}}\}) &= -\sum_\beta \boldsymbol{\mu}_\beta^{\mathrm{ind}}\cdot\mathbf{E}_\beta + \sum_\beta\sum_{\gamma\neq\beta}\boldsymbol{\mu}_\beta^{\mathrm{ind}}\mathbf{T}\boldsymbol{\mu}_\gamma^{\mathrm{ind}} \\ &+ \frac{1}{2}\sum_\beta \frac{(\boldsymbol{\mu}_\beta^{\mathrm{ind}})^2}{\alpha_\beta} \end{aligned} \tag{4.1}$$

Here, the dipole-dipole tensor $\mathbf{T}$ is a function of the distance $r=|\mathbf{r}_\beta-\mathbf{r}_\gamma|=\{x,y,z\}$ between the two interacting atoms (see Fig.4.1). $U^{\mathrm{nuc}}(\{\mathbf{r}_\beta\})$ comprises all bonded and non-bonded terms of a classical force field. In particular, it contains the interaction U^{elec} between the permanent charges q_β. Its derivative determines the electrostatic field $\mathbf{E}_\beta=-\nabla_\beta U^{\mathrm{elec}}/q_\beta$ at the position of the atom β and couples the nuclear and electronic degrees of freedom.

In the spirit of the Born-Oppenheimer approximation the complete potential energy

$$U^{\mathrm{tot}}(\{\mathbf{r}_\beta\};\{\boldsymbol{\mu}_\beta^{\mathrm{ind}}\}) = U^{\mathrm{nuc}}(\{\mathbf{r}_\beta\}) + U^{\mathrm{pol}}(\{\mathbf{r}_\beta\},\{\boldsymbol{\mu}_\beta^{\mathrm{ind}}\})$$

is minimized with respect to the electronic degrees of freedom represented by the point dipoles $\{\boldsymbol{\mu}_\beta^{\mathrm{ind}}\}$ while nuclear degrees of freedom $\{\mathbf{r}_\beta\}$ are kept fixed, *i.e.* $U^{\mathrm{nuc}}(\{\mathbf{r}_\beta\})$ is constant

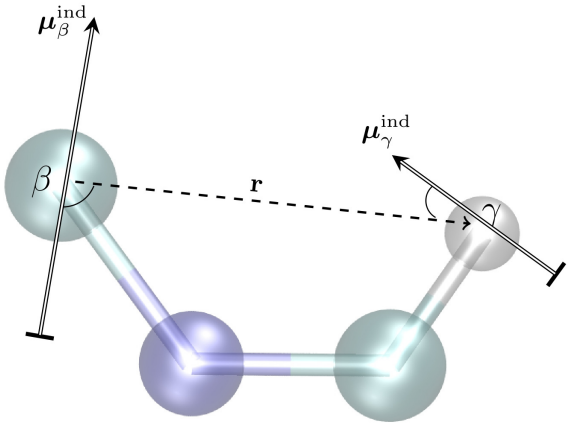

Figure 4.1 Interaction between two induced dipoles.

during the minimization process. This leads to the minimum condition

$$\boldsymbol{\mu}_\beta^{\mathrm{ind}} - \alpha_\beta(\mathbf{E}_\beta - \sum_\gamma^N \mathbf{T}\boldsymbol{\mu}_\gamma^{\mathrm{ind}}) = 0 \tag{4.2}$$

and can easily be rewritten in a matrix representation

$$\begin{pmatrix} \alpha_1^{-1} & \mathbf{T}_{12} & \cdots & \mathbf{T}_{1N} \\ \mathbf{T}_{12} & \alpha_2^{-1} & \cdots & \mathbf{T}_{2N} \\ \vdots & & \ddots & \\ \mathbf{T}_{N1} & \mathbf{T}_{N2} & \cdots & \alpha_N^{-1} \end{pmatrix} \begin{pmatrix} \boldsymbol{\mu}_1^{\mathrm{ind}} \\ \boldsymbol{\mu}_2^{\mathrm{ind}} \\ \vdots \\ \boldsymbol{\mu}_N^{\mathrm{ind}} \end{pmatrix} = \begin{pmatrix} \mathbf{E}_1 \\ \mathbf{E}_2 \\ \vdots \\ \mathbf{E}_N \end{pmatrix}. \tag{4.3}$$

In principle, the induced dipoles can be obtained from the last equation by matrix inversion, but due to the high number of degrees of freedom an iterative approach is usually chosen, *i.e.* the induced dipoles $\boldsymbol{\mu}_\beta^{\mathrm{ind}}$ in Eq. (4.2) are subsequently used to compute the induced dipole moments for the other atoms. This procedure is repeated until the induced dipole moments do not change anymore. If the threshold is sufficiently small, one gets close enough to the potential minimum of energy $U_{\mathrm{min}}^{\mathrm{pol}}$

$$U_{\mathrm{min}}^{\mathrm{pol}} = -\frac{1}{2}\sum_\beta \boldsymbol{\mu}_\beta^{\mathrm{ind}} \cdot \mathbf{E}_\beta \tag{4.4}$$

which represents half of the interaction energy between nuclear and electronic degrees of freedom. In other words, at the minimum the mutual coupling of induced dipoles augmented by their self-energy exactly compensates one half of the interaction energy in Eq. (4.1).

The dipole-dipole tensor $\mathbf{T}$ is the central quantity of the coupling of induced dipole moments sketched in Fig. 4.1. It is the negative double-gradient $\mathbf{T} = -\nabla\nabla\phi_k(r)$ of the respective

Thole function	shape function	default Thole radius R
ϕ_0 (Coulomb)	$\frac{d\phi_0}{dr} = -\frac{1}{r^2}$	
ϕ_1 ("linear")	$\frac{d\phi_1}{dr} = -\frac{1}{r^2}\begin{cases}1 & r \geq R\\ 4\left(\frac{r}{R}\right)^3 - 3\left(\frac{r}{R}\right)^4 & r < R\end{cases}$	$1.662\ (\alpha_\beta \cdot \alpha_\gamma)^{\frac{1}{6}}$
ϕ_2 (exponential)	$\frac{d\phi_2}{dr} = -\frac{1}{r^2}\left(1 - e^{-Rr^3}\right)$	$0.572\ (\alpha_\beta \cdot \alpha_\gamma)^{-\frac{1}{2}}$
ϕ_3 (exponential)	$\frac{d\phi_3}{dr} = -\frac{1}{r^2}\left(1 - e^{-Rr}\left(\frac{1}{2}R^2\, r^2 + R\, r + 1\right)\right)$	$2.089\ (\alpha_\beta \cdot \alpha_\gamma)^{-\frac{1}{6}}$

Table 4.2 Various Thole screening functions. For further details see Thole[43].

modified Coulomb interaction $\phi_k(r)$:

$$\mathbf{T} = -\frac{1}{r}\frac{d\phi_k}{dr}\ \mathbf{I} - \frac{1}{r^2}\left(\frac{d^2\phi_k}{dr^2} - \frac{1}{r}\frac{d\phi_k}{dr}\right)\mathbf{r}:\mathbf{r} \tag{4.5}$$

$$= f_1(\phi_k, r)\ \mathbf{I} - f_2(\phi_k, r)\ \mathbf{r}:\mathbf{r} \tag{4.6}$$

with $\mathbf{r}:\mathbf{r}$ being the dyadic product of the bond vector. Since $\mathbf{I}$ represents a unity matrix, the first part of $\mathbf{T}$ depends solely on the distance r between the interacting atoms β and γ. Consequently, this part of the dipole-dipole tensor correlates the mutual orientation of the interacting dipoles

$$\boldsymbol{\mu}_\beta^{\text{ind}}\mathbf{T}\,\boldsymbol{\mu}_\gamma^{\text{ind}} = f_1(\phi_k, r)\boldsymbol{\mu}_\beta^{\text{ind}} \cdot \boldsymbol{\mu}_\gamma^{\text{ind}} - f_2(\phi_k, r)\left(\boldsymbol{\mu}_\beta^{\text{ind}} \cdot \mathbf{r}\right)\left(\boldsymbol{\mu}_\gamma^{\text{ind}} \cdot \mathbf{r}\right) \tag{4.7}$$

If the induced dipoles $\boldsymbol{\mu}_\beta^{\text{ind}}$ and $\boldsymbol{\mu}_\gamma^{\text{ind}}$ are perpendicular to each other, $f_1(\phi_k, r)$ becomes meaningless for the dipolar interaction. In contrast, if both induced dipole moments are parallel to each other, $f_1(\phi_k, r)$ has the maximum effect. The second part of $\mathbf{T}$ contains information on the mutual position of the interacting atoms. Hence, this part of the dipole-dipole tensor correlates the induced dipoles with the bond vector $\mathbf{r}$ connecting these dipoles. This is indicated by the arcs in Fig. 4.1. If one of induced dipoles is almost perpendicular to the connecting vector $\mathbf{r}$ (e.g. $\boldsymbol{\mu}_\beta^{\text{ind}}$ and $\mathbf{r}$ in Fig. 4.1), $f_2(\phi_k, r)$ gets irrelevant. However, if both dipoles are on top of each other, *i.e.* both are parallel to $\mathbf{r}$, $f_2(\phi_k, r)$ reaches its maximum importance.

Thole functions

In the original point-induced dipole model by Applequist,[203] the Coulomb potential ϕ_0 is unmodified, *i.e.* $\phi_0 = r^{-1}$. This model reproduced mean polarizabilities satisfactorily but overestimated the anisotropy of the polarizability.[43] Furthermore, at short distances the interaction of the induced dipoles becomes too strong leading to even shorter distances and consequently stronger interactions. This so-called "polarization catastrophe" manifests also in the ill-condition of the matrix on the left-hand side of Eq. (4.3). For small distances r, the values of the $\mathbf{T}_{\beta\gamma}$-submatrices are in the same order of magnitude as the inverse values of the polarizability. As a result, the inverse of the matrix in Eq. (4.3) may not be positive definite anymore leading to negative eigenvalues, *i.e.* induced dipoles pointing in the opposite direction of the underlying electric field.[43] In order to avoid such unphysical effects, Thole

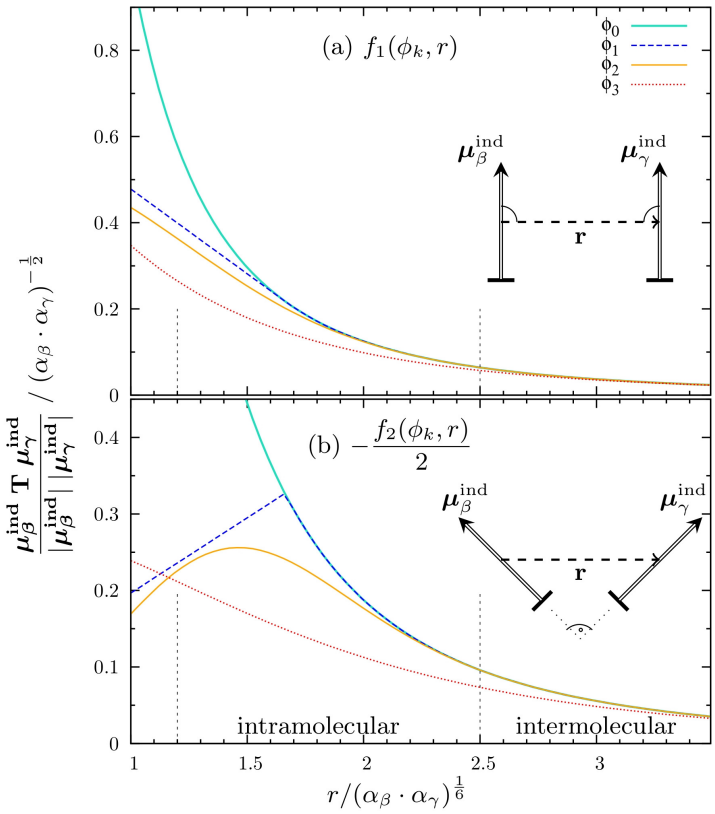

Figure 4.2 Dipolar interaction modified by Thole functions ϕ_k. Please note that both axes are dimensionless.

has suggested several inner damping functions ϕ_k of the Coulomb interaction (see Table 4.2) affecting the corresponding dipole-dipole tensor **T**. The effect of the linear (blue) and exponential (orange and red line) damping functions is demonstrated in Fig. 4.2. The idea behind these damping functions is that the modified **T**-tensor should still be keep its tensoric character, *i.e.* it should be invariant to the rotation or translation of the coordinate system. As a consequence, the modified **T**-tensor still fulfills Eq. (4.5). Additionally, the damping function should be scalable from microscopic to macroscopic polarizabilities and distances.[43] Therefore, the distance in the shape functions $d\phi_k/dr$ is always divided by a corresponding Thole "radius" R (see Table 4.2). This radius consists of the respective polarizabilities in order to get dimensionless properties and a prefactor which was determined by a fitting procedure to experimental polarizabilities.[43] This way, the overestimated anisotropy of the pure Applequist model could be avoided.[43,200] Moreover, the shape functions ϕ_k and their derivative reduce the respective **T**-tensors at short distances. This way, the off-diagonal contributions of the matrix in Eq. (4.3) become less critical making diagonal elements more prominent.

Fig. 4.2 demonstrates the consequences of the Thole damping model. In case of parallel dipoles which are perpendicular to the bond vector **r** (see Fig. 4.2(a)), only $f_1(\phi_k, r)$ affects the damping, *i.e.* the shape functions divided by the distance r. Here, the infinite value of $\phi_0(r \to 0)$ is reduced to a small non-zero value depending on the respective ϕ_k. This weakening of the dipolar interaction at short distances is sufficient to avoid the "polarization catastrophe". In

case of perpendicular induced dipoles, only $f_2(\phi_k, r)$ plays a role. In Fig. 4.2(b) the negative half of $f_2(\phi_k, r)$ is displayed because of the angle of $\pi/4$ and $3/4\ \pi$ between the dipoles and the bond vector, respectively. However, at short distances, the dipolar interaction is reduced to zero by the Thole functions. In Fig. 4.2 the "intramolecular regime" is indicated by vertical lines. It comprises typical distances between atoms connected by a harmonic bond or an angle potential. The shortest possible intermolecular distances can be found for hydrogen bonds. This zone starts at approximately $2.5(\alpha_\beta \cdot \alpha_\gamma)^{1/6}$. The polarizability scaling factor $(\alpha_\beta \cdot \alpha_\gamma)^{1/6}$ ranges from 0.75 Å, e.g. between two hydrogen or a hydrogen and a fluorine, to 1.1 Å in case of two carbons or a sulfur/oxygen interaction.[200]

4.2.3 Methods

The molecular dynamics simulations of [C_2mim][TfO] were carried out with AMBER 11 (see www[193]) on a Sun Fire X2270 dual Quadcore (Intel X5550, 2.66 GHz) using 32 computer cores per job. Since we have shown in a recent paper[17] that 500 ion pairs are the minimum system size to compute reliable dynamics of an ionic liquid system, our simulation box contains N =1000 ion pairs to be on the safe side. This corresponds to 27000 atoms. In order to cope with the long range nature of Coulomb interactions in a finite system, all simulations were carried out with an Ewald κ of 0.41 Å^{-1}, a skin of 2.0 Å and a van-der-Waals cut-off of 10.0 Å. The temperature was adjusted to 300 K by a Berendsen thermostat and trajectories are computed for at least 15 ns and extend up to 30 ns.

In principle, polarizable simulations are more CPU time consuming than non-polarizable ones, but the combination of point-induced dipoles and Lagrangian thermostats enables us to confine the additional effort to 40% as shown in Table 4.3. This is faster than our previous Drude model which expanded the numerical effort by a factor of 1.9. The table also shows that the increased accuracy ($T_\mu = 0.06$K) of the Lagrangian methods does not results in a significant increase in computational time. However, the dynamics is accelerated by approximately 10% since the more optimized induced dipoles ($T_\mu = 0.06$K) shield the adhesive interaction between cations and anions better compared to the weak Lagrangian thermostat with an average temperature of $T_\mu = 40$K for the induced dipole motion.

In contrast, conventional self-consistent field approaches (SCF) are slower by a factor of at least 3 for very low accuracy ($\delta\mu \leq 10^{-4}$D) or 18 at standard accuracy of $\delta\mu \leq 10^{-7}$D. In theses cases, the SCF iteration is stopped at step n, if the changes of induced dipoles

$$\delta\mu(n) = \sqrt{\frac{\sum_{\beta}^{N}\Big(\boldsymbol{\mu}_\beta(n) - \boldsymbol{\mu}_\beta(n-1)\Big)^2}{N}} \tag{4.8}$$

have become numerically negligible. Unfortunately, a slack SCF-threshold of $\delta\mu \leq 10^{-4}$D means that the potential minimum of $U_{\min}^{\mathrm{pol}}$ in Eq. (4.4) is not reached. This leads to an artificial deceleration of dynamics which is worse than the effect of a Lagrangian thermostat T_μ of 40 K.

AMBER 11 was used together with version 1.5 of AmberTools.[193] The latter is of impor-

Model	Method	Stringency	CPU time
non-polarizable			1.4 h
PID	LAG	$T_\mu = 40.0$K	2.2 h
PID	LAG	$T_\mu = 0.06$K	2.0 h
Drudes[24]	LAG	$T_\mu = 1$K	2.7 h
PID	SCF	$\delta\mu \leq 10^{-4}$D	3.9 h
PID	SCF	$\delta\mu \leq 10^{-7}$D	25.0 h

Table 4.3 Computational effort of various MD methods to produce a 100 ps trajectory slice of 1000 ionic liquid ion pairs.

tance since our Drude force field[24] including polarizabilities of van Duijnen[200] and classical force field parameters of Pádua and Canongia Lopes[174,175] was developed for CHARMM[189] and automatically translated for AMBER via CHAMBER. This ensures that the complete setup (including the accuracy of natural constants of CHARMM) stays the same. Afterwards, hydrogen polarizabilities are added since they were not part of the above mentioned force field.[24] The polarizabilities of the non-hydrogen atoms are identical.

In order to elucidate the influence of the Thole damping in more detail, we started four independent simulations including the Thole functions ϕ_0 to ϕ_3. These simulations were accompanied by a non-polarizable system. Furthermore, these simulations were performed at two different densities, ρ_{exp} =1.384 and ρ_{ff} =1.437 g/cm^3. The corresponding box lengthes are 67.8Å and 67.0Å, respectively. The lower density corresponds to the experimental value[204] while the higher density is obtained by a NPT equilibrium simulation prior to the production runs. This discrepancy of 3.8% between the experimental and the force field density is already found for the non-polarizable force field.[175] In contrast, Borodin reported that turning off the cationic polarizability results in a density decrease of 0.8% in case [C_2min][BF_4], whereas anionic polarizability seems to have no influence on density.[32]

4.2.4 Results and Discussion

The influence of density on the structure and dynamics

At first sight, one would expect that increasing the density would lead to a more or less uniform reduction of the interionic distances. However, in practice, it turns out that the increasing density primarily affects distances between ions of the same charge. As visible in Fig. 4.3a the center-of-mass distances between cations and anions is unaffected by the increase in density. This is true for the non-polarizable (gray and black) as well for the polarizable (bright and dark green) simulations. However, the probability for hydrogen-bonding of the imidazolium hydrogens is slightly affected. The chance to find a hydrogen bond[205] of an imidazolium ring hydrogen to a triflate fluorine in the non-polarizable simulations is approximately 10% and 9% for ρ_{ff} and ρ_{exp}, respectively. These chances are scaled roughly by a factor of 0.9 in case of the polarizable force field. Additionally, 2% of the imidazolium ring hydrogens are hydrogen-bonded to triflate oxygens, irrespective of the density and polarizability. The center-of-mass distances of adjacent cations is shifted by a little bit more

Method	Structure					Rotation				Translation					
	ρ $\left[\frac{\mathrm{g}}{\mathrm{cm}^3}\right]$	ϕ_k	G_K^{++}	G_K^{--}	G_K^{+-}	$\langle\tau_{\mathrm{ind}}^{+}\rangle$ [ns]	$\langle\tau_{\mathrm{ind}}^{-}\rangle$ [ns]	$\langle\tau_{\mathrm{rot}}^{+}\rangle$ [ns]	$\langle\tau_{\mathrm{rot}}^{-}\rangle$ [ns]	D^{+} $\left[10^{-8}\frac{\mathrm{cm}^2}{\mathrm{s}}\right]$	D^{-} $\left[10^{-8}\frac{\mathrm{cm}^2}{\mathrm{s}}\right]$	$\langle\tau_{\mathrm{cage}}^{++}\rangle$ [ns]	$\langle\tau_{\mathrm{cage}}^{--}\rangle$ [ns]	$\langle\tau_{\mathrm{cage}}^{+-}\rangle$ [ns]	$\sigma(0)$ [S/m]
non-pol.	1.437		0.71	0.67	1.17			7.3	2.1	1.9	0.87	≈72	≈83	≈92	0.052
LAG	1.437	ϕ_0	0.78	0.88	0.94	0.29	0.32	1.3	0.35	13.4	9.4	7.7	7.2	8.8	0.33
LAG	1.437	ϕ_1	0.97	0.88	0.94	0.29	0.31	1.3	0.34	13.1	9.4	8.0	7.6	9.1	0.29
LAG	1.437	ϕ_2	0.97	0.88	0.95	0.24	0.28	1.2	0.26	14.8	9.4	7.4	7.7	8.8	0.36
LAG	1.437	ϕ_3	0.99	0.86	0.96	0.33	0.39	1.5	0.40	11.1	6.7	11	12	14	0.29
non-pol.	1.384		0.96	0.86	1.17			2.5	0.59	5.6	1.8	≈23	≈25	≈38	0.22
LAG	1.384	ϕ_0	0.98	0.88	0.93	0.11	0.12	0.43	0.13	34.7	24.6	2.9	2.7	4.6	0.77
LAG	1.384	ϕ_1	1.01	0.88	0.95	0.12	0.12	0.44	0.13	34.3	23.7	3.0	2.9	4.7	0.64
LAG	1.384	ϕ_2	0.98	0.87	0.95	0.10	0.12	0.40	0.12	38.6	23.2	2.8	2.9	4.6	0.88
LAG	1.384	ϕ_3	0.97	0.85	0.96	0.11	0.13	0.49	0.15	34.0	20.8	3.8	3.8	5.5	0.75

Table 4.4 System dynamics as a function of density ρ and Thole screening function ϕ_k.

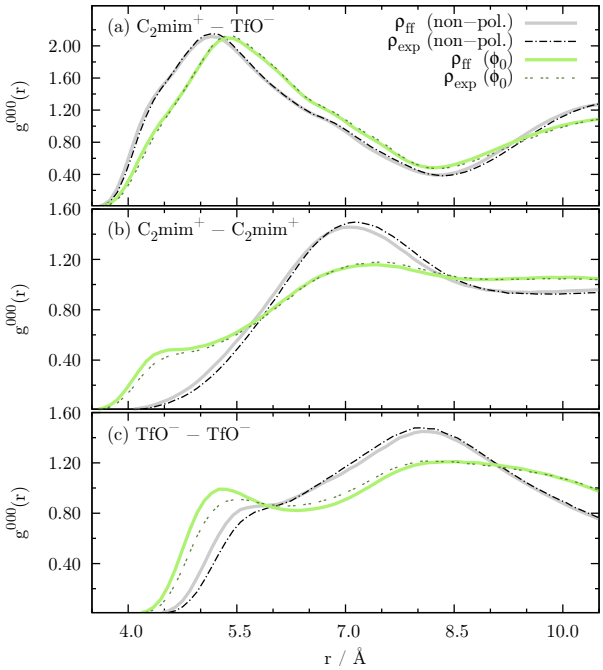

Figure 4.3 Change of the radial distribution functions as a function of polarizability and density.

than 2% in Fig. 4.3b. The density effect on the anions is even stronger (see Fig. 4.3c). Nevertheless, the overall shape of the radial distribution functions including peaks and shoulders is conserved in all cases.

However, the effect of polarizability is enormous at both densities. The induced dipoles act as an "inner solvent" reducing the effective charge of the molecules.[25,158] Consequently, the attractive interaction between cations and anions is reduced and the center-of-mass distance is shifted by 0.5 Å in the first shell. In contrast, the distance between the centers-of-mass of adjacent cations is reduced due to the lower charge repulsion. The emerging shoulder at 4.4 Å in case of the polarizable systems can be attributed to π-stacked imidazolium rings and was also observed in case of $[C_2mim][NO_3]$.[29] The lower charge repulsion due to the shielding by the polarizability is also visible in the radial distribution functions between anions. Since the charge density at the surface of the anions is higher when compared to the bulkier cations, the polarizability effect is stronger.

In case of $[C_2mim][NO_3]$ Yan *et al.* also reported a reduced Coulombic repulsion between like ions due to the induced dipoles,[29] but the impact is smaller than reported here. This may be due to the higher temperature of their simulations (=400 K) and/or their lower polarizabilities, *i.e.* $\alpha(C_2mim)$ is 11.8 Å^3 and 14.2 Å^3 for their and our simulations, respectively. However, the reduction of Coulombic interactions by induced dipoles is also known for molten salts.[206]

The radial distribution function $g^{000}(r)$ probes the distance between the molecules. Their orientation can be measured by the orientational correlation function $g^{110}(r)$ for cations–anions, cations–cations and anions–anions.[207] These distance-dependent functions can be

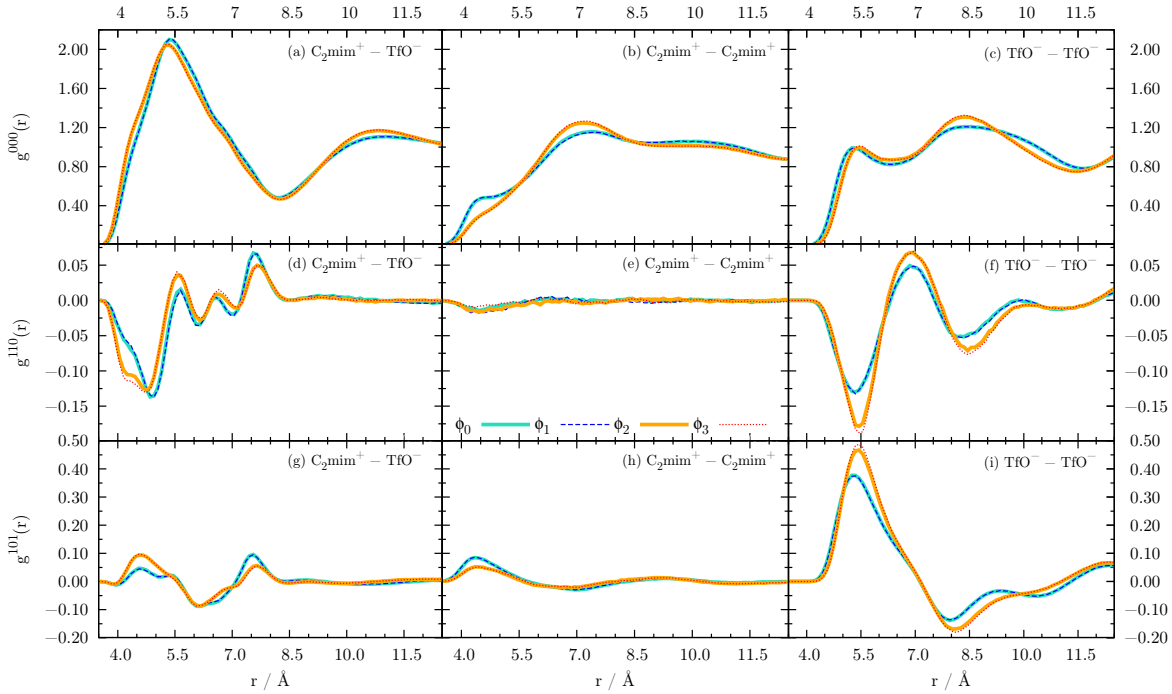

Figure 4.4 Radial distribution and orientational correlation functions at ρ_{ff} for various Thole functions.

integrated to yield the so-called Kirkwood G_K-factor:[207]

$$G_K = 1 + 4\pi\rho \int_0^{''\infty''} g^{110}(r)\, r^2 dr \tag{4.9}$$

The corresponding values for our (non-)polarizable [C_2mim][TfO]-systems under investigation are given in Table 4.4. Interestingly, the Kirkwood-factor G_K^{+-} for the non-polarizable systems is 1.17 at both densities indicating a weak preference for parallel dipoles between cations and anions. However, the point-induced dipoles weaken the correlation between cations and anions and the parallel dipolar alignment vanishes. The dipolar alignment for cation–cation and anion–anion depends on the density. At ρ_{exp} =1.384 g/cm^3 the system seems to be more relaxed compared to the higher density. Consequently, the dipolar orientation and hence G_K^{++} and G_K^{--} do not change when switching on the polarizability. In contrast, the anions at ρ_{ff} =1.437 g/cm^3 seem to be so close to each other that the unhindered charge repulsion forces orient the anionic dipoles in an antiparallel way (G_K^{--}=0.67). The point-induced dipoles extenuate the charge repulsion and weaken the preference for antiparallel anionic dipoles. In case of the cations, the polarizable effect is weaker but present.

In agreement with Yan *et al.*[29], the structural oscillations in $g^{000}(r)$ extend over more than 20 Å at both densities indicating strong long-range forces which should be of electrostatic nature. These oscillations are even more prominent in the non-polarizable systems and can be detected up to 40 Å.

The higher value of the density in the MD simulations can also be reached in experiment by lowering the temperature by more than 30 K.[208] Of course, this temperature reduction

goes along with an increase in viscosity and might be one reason for the slow dynamics of the Pádua force field.[174,175] It seems that the Lennard-Jones parameters used here (originally taken from the OPLS force field[209]) favor supercooling of the ionic liquid and should be optimized in future force fields. However, the dynamics can be accelerated in the MD simulation by a factor of approximately 2.7 when switching to the experimental density (ρ_{exp}=1.384 g/cm^{-3}) as visible in Table 4.4. Interestingly, this acceleration factor applies to the translation motion, e.g. diffusion coefficients of the cations and anions, as well as to the rotation, *i.e.* the relaxation constants for the induced and total dipole moments of the cations and anions. This uniform scaling points out, that the underlying effect should have hydrodynamic character, *i.e.* the viscosities of the systems should differ by the acceleration factor.

However, we are interested in the effect of the Thole functions on the interaction between cations and anions of the ionic liquid in this work. Since effects should be more visible for the higher density, ρ_{ff}=1.437 g/cm^{-3}, which corresponds to overall smaller distances between the ions (at least for like charges), we will use this system as reference for our observations. In addition, this is also the density at which the force field is in equilibrium.

Structural changes due to various Thole functions

The radial distribution functions $g^{000}(r)$ at force field density are depicted in Fig. 4.4a-c with the effective Thole functions ϕ_k. Interestingly, the "linear" Thole function (ϕ_1, blue line) seems to have no specific effect on the structure of the ionic liquid since it yields the very same results as using no Thole function (ϕ_0, turquoise solid line) at all. The corresponding g-functions of both exponential Thole functions (ϕ_2, orange solid line) and (ϕ_3, red dashed line) differ significantly from those of ϕ_0 and ϕ_1 but are very similar to each other. First, the radial distribution function between cations shows a shoulder at 4.5 Å which is not present in case of the exponential Thole functions. At these short center-of-mass distances, this peak can be attributed to π-stacking imidazolium ring. In addition, the radial distribution function between the anions (see Fig. 4.4c) seems to be shifted outwards by 0.2 Å. In contrast, $g^{000}(r)$ between cations and anions is shifted inwards by 0.2 Å.

Overall, this can be explained by the lower molecular polarizability in case of exponential Thole functions. Inspecting Fig. 4.2a and b shows that the intramolecular dipole-dipole interaction is unaffected in case of ϕ_1 at distances between 1.5 and 1.9$(\alpha_\beta \cdot \alpha_\gamma)^{1/6}$ but is screened for ϕ_2 and ϕ_3. Consequently, the inner solvent in case of ϕ_2 and ϕ_3 dampsthe repulsive interaction between like-charged ions less and therefore, too narrow positions seem unfavorable. This effect was already observed (even much stronger) for the juxtaposition of polarizable and non-polarizable simulations in Fig. 4.3.

Although emerging from atomic contributions, $\boldsymbol{\mu}_\beta^{\mathrm{ind}}\mathbf{T}\boldsymbol{\mu}_\gamma^{\mathrm{ind}}$, we interpret our data on a molecular level for the sake of simplicity and tradition. The molecular dipole μ_i consists of all permanent and induced contributions from all atoms β and γ. In particular, the induced contributions play an important role for the cationic dipoles. The dipole-dipole tensor $\mathbf{T}$ is not only affected by the distance of the two interacting dipoles but also by their orien-

tation and position (see Fig. 4.2). Its influence on the molecular structure can be described by the orientational correlation functions $g^{110}(r)$ and $g^{101}(r)$ which are an extension to the radial distribution function $g^{000}(r)$:[207,210]

$$g^{000}(r) = \frac{1}{\rho \cdot 4\pi r^2 dr} \left\langle \sum_j \delta(r - |\mathbf{r}_{ij}|) \right\rangle_i \tag{4.10}$$

$$g^{110}(r) = \frac{1}{\rho \cdot 4\pi r^2 dr} \left\langle \sum_j \frac{\boldsymbol{\mu}_i \cdot \boldsymbol{\mu}_j}{|\boldsymbol{\mu}_i| \, |\boldsymbol{\mu}_j|} \delta(r - |\mathbf{r}_{ij}|) \right\rangle_i \tag{4.11}$$

$$g^{101}(r) = \frac{1}{\rho \cdot 4\pi r^2 dr} \left\langle \sum_j \frac{\boldsymbol{\mu}_i \cdot \mathbf{r}_{ij}}{|\boldsymbol{\mu}_i| \, |\mathbf{r}_{ij}|} \delta(r - |\mathbf{r}_{ij}|) \right\rangle_i \tag{4.12}$$

Here, the mutual orientation and position of the pair of dipoles $\boldsymbol{\mu}_i$ and $\boldsymbol{\mu}_j$ is reflected by $g^{110}(r)$ and $g^{101}(r)$, respectively.

Application of ϕ_0 and ϕ_1 results in an almost identical orientation of the ionic dipoles. The same holds true for the pair ϕ_2 and ϕ_3. However, the respective orientation of the second pair is more pronounced, in particular for the anion–anion correlation in Fig. 4.4f. The orientational correlation function $g^{110}(r)$ indicates a preferred antiparallel alignment of dipoles between adjacent anions (see Fig. 4.4f) as well as between anions and cations (see Fig. 4.4d) because of the negative values at distances shorter than 6 Å. The overall alignment of anionic dipoles is also antiparallel as demonstrated by the corresponding G_K^{--} factor computed by Eq. (4.9). The collective cation-anion dipole alignment is weaker since the corresponding G_K^{+-} in Table 4.4 approaches unity. Both, the $g^{110}(r)$-function in Fig. 4.4e and its corresponding integral over spherical shells G_K^{++} in Table 4.4 show no systematic self-alignment of cationic dipoles.

$g^{101}(r)$ measures the anisotropy of ion distribution around a reference ionic dipole: Positive values indicate an ionic position in the northern hemisphere whereas negative values refer to the southern region. For example, in case of a TfO^- reference dipole, the northern hemisphere is around the CF_3-moiety. Correspondingly, for distances shorter than 6 Å subfigure 4.4i shows a crowding of TfO^--ions around the CF_3-unit with antiparallelly aligned dipoles (see Fig. 4.4f). For larger distances the mutual dipolar orientation is reversed. The $g^{101}(r)$-functions involving the cation are rather flat which would suggest an isotropic distribution. However, this is mainly caused by the large fluctuations of the reference cationic dipole. In addition, anions are usually located quite near the H2-hydrogen of the imidazolium ring. This configuration corresponds to an angle of a little less than 90° between $\mathbf{r}_{ij}$ and $\boldsymbol{\mu}_i$ and hence very small $g^{101}(r)$-values at distances shorter than 6 Å. As already observed for $g^{000}(r)$ and $g^{110}(r)$ the influence of the Thole functions again shows the resemblence of $\{\phi_0, \phi_1\}$ on the one side and $\{\phi_2, \phi_3\}$ on the other. Quite generally, the root of this pairing pattern is $g^{000}(r)$ which can in principle be shown by the normalized functions $g^{110}(r)/g^{000}(r)$ and $g^{101}(r)/g^{000}(r)$ (data not shown). This is also reflected by the Kirkwood-factors which are almost independent of the Thole function ϕ_k (see Table 4.4). This means that Thole damping is too weak to change the orientation and position of dipoles, it rather affects the translational packing of the ions. Considering non-polarizable and unchanged polarizable (ϕ_0) simulations, the exponential Thole functions, ϕ_2 and ϕ_3, seem to decrease the overall

polarizability of the system by a small amount. In this way, Thole damping shifts little the orientational structure towards that of the non-polarizable system.

The influence of Thole functions on the dynamics

The higher effective polarizability of ϕ_0 and ϕ_1 simulations is also reflected by the auto-correlation function of the induced dipole moments $\langle \boldsymbol{\mu}^{\mathrm{ind}}(0) \cdot \boldsymbol{\mu}^{\mathrm{ind}}(t) \rangle$. In order to be compatible with the dielectric spectrum discussed later we give N times the scaled Fourier Laplace transform

$$\mathscr{L}_{\mathrm{V}}\Big[f(t)\Big] = \frac{1}{3Vk_BT\varepsilon_0} \int_0^\infty -\frac{d}{dt}\langle f(0) \cdot f(t) \rangle \, e^{i\omega t} dt \tag{4.13}$$

in Fig. 4.5a-b. Here, we find the pairing of $\{\phi_0, \phi_1\}$ and $\{\phi_2, \phi_3\}$ again. The higher effective polarizability of the systems affected by the Thole functions ϕ_0 and ϕ_1 can be deduced from the peak heights. The average relaxation constant $\langle \tau^{\mathrm{ind}} \rangle$ is given in Table 4.4 for each Thole function, density and species.

As the overall molecular polarizability of the cations is almost twice that of the anions, the corresponding peaks differ approximately by a factor of four. In contrast, this ratio of dipoles is reversed in case of molecular dipoles, comprising permanent and induced contributions. In case of the cations, induced dipoles contribute significantly ($\simeq 20\%$) to the molecular dipole spectrum given in Fig. 4.5c. Since the permanent anionic dipoles are much stronger than their induced counterparts, they make up the anionic dipolar spectrum in Fig. 4.5d. So far, we have only considered molecular spectra lacking any cross-correlations between the dipolar ions. However, the dominance of the permanent dipoles of the anions even produces an apparent similarity of the anionic molecular spectrum to the dielectric permittivity $\varepsilon(\omega) = \mathscr{L}_{\mathrm{V}}[\mathbf{M}_{\mathrm{D}}(t)]$ governed by the overall collective rotational dipole moment $\mathbf{M}_{\mathrm{D}}(t)$. This similarity may be explained by the close-to-unity values of the three Kirkwood-factors G_K^{+-}, G_K^{--} and G_K^{++} given in Table 4.4. At the collective level, the pairings $\{\phi_0, \phi_1\}$ and $\{\phi_2, \phi_3\}$ are not visible anymore since collective dielectric properties are of long-range nature and therefore involves those intermolecular distances where the Thole damping has leveled off.

Since the molecular ions $EMIM^+$ and TfO^- are not only dipolar but also charged species, the dielectric spectrum is enriched by translational contributions. Here, the volume expansion of the charge centers may be seen as additional intermolecular dipoles. Consequently, the translation of these charge centers governs the relaxation of the collective translational dipole moment $\mathbf{M}_{\mathrm{J}}(t)$. In principle, the translational contribution to the generalized dielectric constant can be obtained by $\vartheta(\omega) = \mathscr{L}_{\mathrm{V}}[\mathbf{M}_{\mathrm{J}}(t)]$, but in practice it is much easier to fit the initial region of the collective charge displacement $\langle \Delta\mathbf{M}_J^2(t) \rangle$.[44,157] The curve presented in Fig.4.5f was obtained by a fit of $\langle \Delta\mathbf{M}_J^2(t) \rangle$ up to 500 ps although computed over the complete time window of the 30 ns trajectories.

As visible in Fig. 4.5e and f, the dielectric permittivity $\varepsilon(\omega)$ and the dielectric conductivity $\vartheta_0(\omega)$ overlap over a very large region in frequency space from GHz to THz. In addition, $\varepsilon(\omega)$ involves slow relaxation processes below 1 GHz which are not found in $\vartheta_0(\omega)$. The overlap complicates the interpretation of experimental spectra since only the sum of these

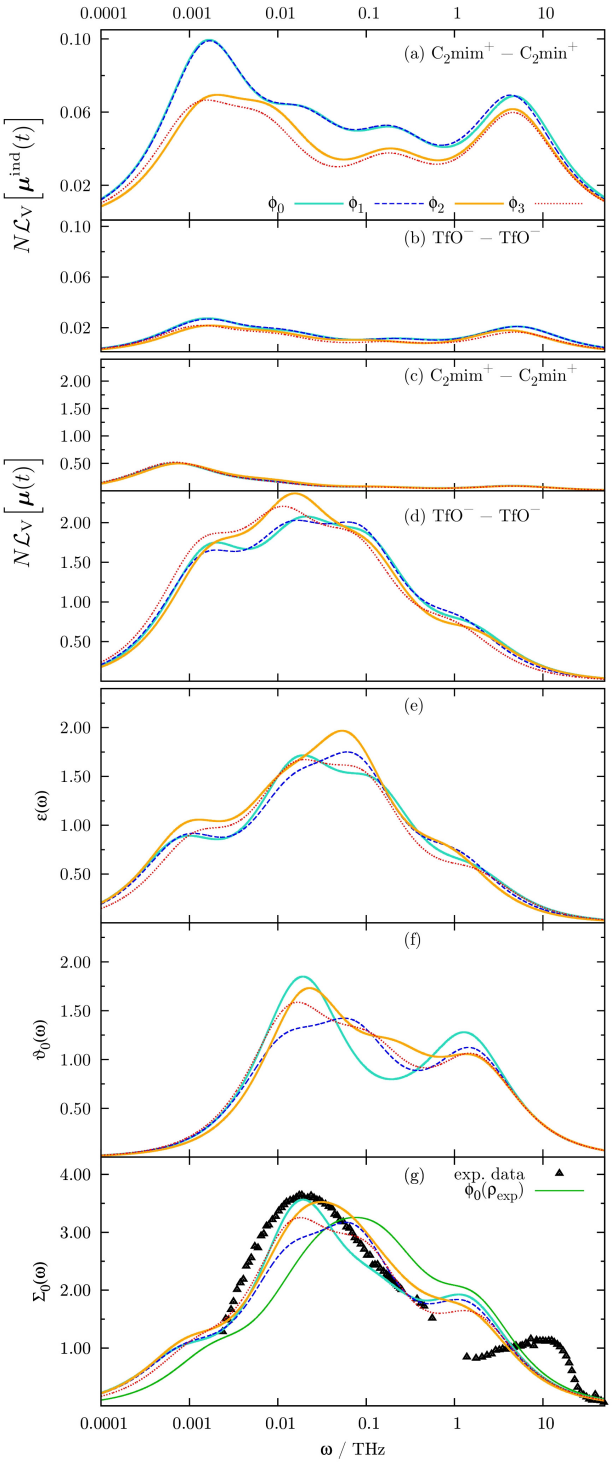

Figure 4.5 Frequency-dependence of autocorrelation functions contributing to the generalized dielectric constant $\Sigma_0(\omega)$: Induced dipole moments of the cations (a) and anions (b), molecular dipole moments of cations (c) and anions (d), dielectric permittivity $\varepsilon(\omega)$ (e), dielectric conductivity $\vartheta_0(\omega)$ (f) and the complete spectrum of $\Sigma_0(\omega)$ (g).

contribution can be measured.[19] The experimental data (see black triangles in Fig. 4.5g) agree reasonably with our simulations at force field density. In case of ρ_{exp}, the computational spectrum is shifted to higher frequencies (see green curve) by the acceleration factor of 2.7 discussed earlier.

The dielectric conductivity $\vartheta_0(\omega)$ is defined by

$$\vartheta_0 = 4\pi i \frac{\sigma(\omega) - \sigma(0)}{\omega} \tag{4.14}$$

and hence depends on the conductivity $\sigma(\omega)$. Although the zero-frequency value $\sigma(0)$ at ρ_{exp} fits better the experimental value of 0.774 S/m,[211] the non-directed translational motion, $\sigma(\omega) - \sigma(0)$, is better described at the higher density ρ_{ff}. Since the $\sigma(0)$-hyperbola is commonly removed from the dielectric spectrum (cf. Eq. (4.14)) by experimenters and in simulations, the directed translation of charge carriers does not play a significant role in the generalized dielectric spectrum $\Sigma_0(\omega)$. In contrast, the translational contribution to $\Sigma_0(\omega)$ is dominated by the jittering of ions in the cage of their neighbors.[157]

Cage dynamics in simulations are best investigated by Voronoi tessellation.[96,210] In particular, we have learnt that the first shell of the cage makes the essential contribution.[157] Therefore, we have calculated the mean residence time $\langle\tau_{\text{cage}}\rangle$ of the cations and anions around a central ion. Here, $\langle\tau_{\text{cage}}\rangle$ is the relaxation constant of the residence correlation function $\langle n(0)\cdot n(t)\rangle$, where $n(t)$ is a binary function indicating whether an ion is member of the first shell or not.[96,210] For a consistent interpretation we have fitted $\langle n(0)\cdot n(t)\rangle$ with a Kohlrausch-Williams-Watt function

$$\langle n(0)\cdot n(t)\rangle \simeq a\cdot e^{-\left(\frac{t}{\tau}\right)^{\beta}}. \tag{4.15}$$

Thereby, β-values for the combination cation–cation ($\beta^{++} = 0.595$), cation–anion ($\beta^{+-} = 0.748$) and anion–anion ($\beta^{--} = 0.414$) could be kept fixed for all Thole functions and densities in order to reduce the number of adjustable parameters. In this way, the variation of cage migration can be mapped to a single relaxation time τ. The respective average relaxation time $\langle\tau_{\text{cage}}\rangle = \tau/\beta\cdot\Gamma(1/\beta)$ is given in Table 4.4. Of course, the residence time $\langle\tau_{\text{cage}}^{+-}\rangle$ is the longest, but neighborhood relations between like charges is only 15% shorter. This is a clear evidence of a mixed cage instead of the classical picture of an anionic cage around the cations and vice versa. This finding can also be deduced from the coordination numbers computed by $\langle n(0)^2\rangle$:[96] $EMIM^+$ are surrounded by 9.5 cations and 8.2 anions on average. The anionic cage consists of approximately 4.0 anions and 8.2 cations. The high number of like charge ions in the ion cage is also reported by Yan *et al.*[29]

Interestingly, the residence times $\langle\tau_{\text{cage}}\rangle$ correlate with both, the rotational relaxation times $\langle\tau_{\text{rot}}\rangle$ and diffusion coefficients, for different Thole functions ϕ_k and densities. Therefore, the cage is essential for translational migration as well as reorientation. In particular, the dynamical results from ϕ_0, ϕ_1 and ϕ_2 accompany each other but dynamics in case of ϕ_3 seems to be decelerated by at least 20%. In contrast to the structure dominated by the intramolecular region ($r < 2.5(\alpha_\beta\cdot\alpha_\gamma)^{1/6}$) in Fig. 4.2, the dynamics is controlled by the inter-

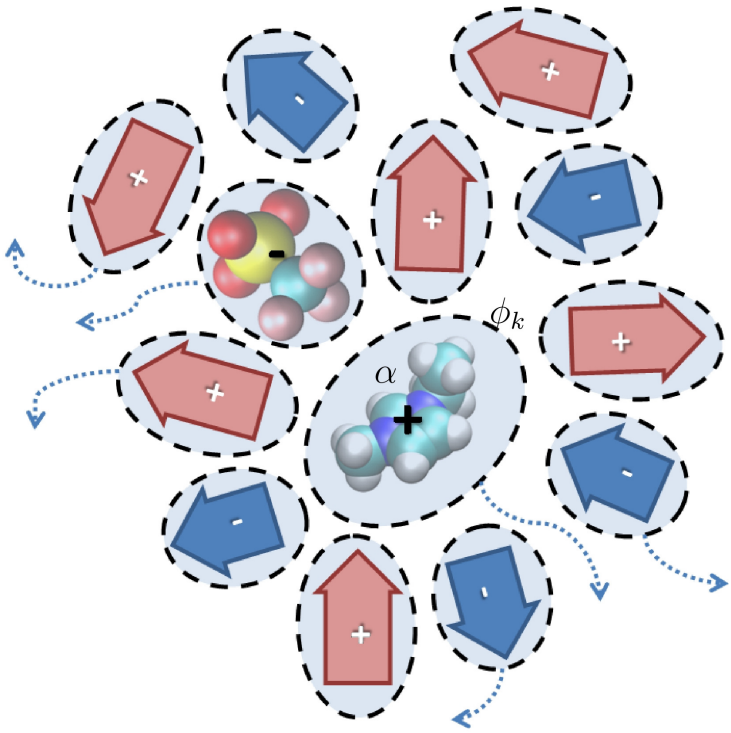

Figure 4.6 The induced dipoles act as inner solvent (blue shaded areas) to damp electrostatic interaction. They are controlled by the corresponding polarizabilities α. The Thole functions ϕ_k (black dashed lines) govern the effectivity of the inner solvent at short distances. Cations and anions are displayed as red and blue arrows, respectively. The arrows indicate the direction of the corresponding dipole moments.

molecular zone. In fact, for $r > 2.5(\alpha_\beta \cdot \alpha_\gamma)^{1/6}$ in Fig. 4.2 the Thole functions ϕ_0, ϕ_1 and ϕ_2 become identical while ϕ_3 is still below.

4.2.5 Conclusion

Overall, the use of Thole functions has only a moderate influence on the structure and dynamics of ionic liquids. On second sight, exponential Thole functions $\{\phi_2, \phi_3\}$ seem to reduce the molecular polarizability slightly shifting the polarizable systems back to the non-polarizable case. Corresponding changes in structure mainly affects the distance of the ions but keep the orientation and mutual position. Changes in single-particle dynamics only occur for ϕ_3. However, this effect can be reduced significantly by enhancing the Thole radius R_3. In fact, the default value of 2.089 (cf. Table 4.2) in AMBER is increased to 2.6 in CHARMM.[189] In any case, collective dynamics seems to be independent of Thole damping. By the way, we note that our simulations ran stable for 30 nanoseconds without any Thole function at both densities.

The different behavior of structure, single-particle and collective dynamics can be explained by a three zone model: For very short distances below a scaled distance of 2.5, exponential Thole functions modify induced dipolar interactions in the same fashion whereas the linear Thole function accompanies ϕ_0, *i.e.* no effective Thole damping. The second zone

is characterized by the short intermolecular distances typical for interactions of a central ion with its cage. Here, ϕ_1 and ϕ_2 have already leveled off and behave like ϕ_0. In contrast, ϕ_3 still damps the dipolar interaction to some extent. In the third region comprising long intermolecular distances, Thole damping has leveled off. Consequently, collective dynamics is hardly affected. It is interesting to note that the principal pattern derived from the atomic $\boldsymbol{\mu}_\beta^{\mathrm{ind}} T \boldsymbol{\mu}_\gamma^{\mathrm{ind}}$ can be mapped on structure, single-particle and collective dynamics of the ionic liquids molecules, respectively.

In a pictorial way our simulation studies on polarizable systems with Thole damping at various densities can be summarized by Fig. 4.6. Each ion is immersed in its "inner" solvent created by its induced dipoles (blue shaded areas). The interface to the inner solvent of other molecules is governed by the Thole functions ϕ_k indicated by black dashed lines in Fig. 4.6. The screening by the inner solvent favors the rapprochement of like charges thus stabilizing their residence in the cage. In fact, the cage around a central ion consists of cations and anions in comparable number. This finding strongly disagrees with the common picture of a cation surrounded solely by anions and vice versa.

Lowering the overall density results in larger distances between the like ions but hardly affects cation–anion distances. Nevertheless, these structural changes are sufficient to slacken the cage making it more permeable. This way, a central ion may escape its original cage more easily indicated by the blue arrows in Fig. 4.6.

Acknowledgement

The computational work was performed at the Vienna Scientific Cluster of the University of Vienna, the Vienna University of Technology and the University of Natural Resources and Applied Life Science, Vienna. We thank for generous allocation of computer time. This work was supported by Project No. P23494 of the FWF Austrian Science Fund.

4.3 Comparing induced point-dipoles and Drude oscillators

Phys. Chem. Chem. Phys., **17**, *14297 (2015)*

Michael Schmollngruber,[a] Volker Lesch,[b] Christian Schröder,[a] Andreas Heuer[b] and Othmar Steinhauser[a]

[a] *University of Vienna, Department of Computational Biological Chemistry, Währingerstrasse 17, A-1090 Vienna, Austria*

[b] *Insitute of Physical Chemistry, Westfälische Wilhelms-Universität Münster, Germany*

Classical Molecular Dynamics simulations describing electrostatic interactions only by point charges can be augmented by the inclusion of atomic polarisabilities modelling charge flexibility. Two widely used models, Drude oscillators and induced point-dipoles, are compared in a systematic study using their respective implementations in CHARMM and AMBER. The question of necessity and importance of polarisable hydrogen atoms is raised and two implementations, in an implicit or explicit manner, are compared to the case of non-polarisable hydrogen atoms. For all these polarisability models, the strength of the respective atomic polarisabilities was incremented in steps of ten percent up to their full values. The influence of polarisability on the structure and dynamics of the ionic liquid $EMIM^{+}TfO^{-}$, which is chosen as a test case, is studied thoroughly. Using appropriate model functions, the respective dynamical and structural data are fitted. Thus, a small set of parameters is deduced, which highlights the effect of polarisability. Generally, flexibility of the charge distribution leads to enhanced fluidity and less pronounced structure. As this usually occurs when adding a co-solvent to an ionic liquid, the inclusion of polarisability can be seen in much the same way in that it acts like an inner solvent.

4.3.1 Introduction

Computer simulations of soft matter have a long tradition.[16] In order to cope with the complexity of the problem, i.e. system size, simulation length and sufficient sampling, interaction potentials have to be designed which are both, realistic as well as economic.[212] For this reason, the electrostatic part of interaction is traditionally described by a set of permanent point charges.[213] This prohibits, however, the reaction of a molecular charge distribution to changes of its environment. Recent years have seen a development of models to introduce flexible charge distributions, thus augmenting traditional molecular mechanics force fields. Three principal methods have evolved in the literature.[198]

On the one hand, the strength of the charges may fluctuate within a molecule - constrained to a fixed net charge - while keeping the positions of the charges at atomic sites. This quite intuitive approach is usually called the Fluctuating Charge Model (FCM).[35–42] Unfortunately, its application is limited by the molecular geometry. For example, one cannot create out-of-plane charges in a planar molecule.

On the other hand, the permanent charges may be augmented by auxiliary charges or dipoles, the position or orientation of which is reactive to the environment. This idea has been realized in two concrete models: Induced Point-Dipoles (IPD)[27–34] and Drude Oscillators (DRU).[20–26] In the first case, mathematical dipoles located at atomic positions are calculated as a linear response to the local electric field. In other words, the strength of the induced dipoles is governed by a linear factor , i.e. the atomic polarisability. However, this implies that the traditional treatment of electrostatics based on point charges has to be extended to handle dipoles as well.[214,215] This initiated the idea of Drude oscillators: additional pairs of opposite charges are attributed to each atom. While one of these is united with the respective atom, the other one is tethered by a flexible spring. Its displacement is determined by the product of the atomic polarisability times the local field. Thus, the Drude pair creates an oscillating physical dipole.[20,26]

In this work, we aim for a critical comparison of the IPD and DRU models. As a test system we have chosen the molecular Ionic Liquid (IL) 1-ethyl-3-methyl-imidazolium ($EMIM^+$) triflate (TfO^-) (cf. Fig. 4.7). In this class of soft matter every molecule carries a net charge. This leads to extraordinarily strong local electric fields, which in their turn create strong induced dipoles. This makes this investigation of dual interest. On the one hand, we are testing the IPD and DRU models up to their methodic limits. On the other hand, we focus on a system, where flexible electrostatics is essential.[24,191]

Implementing either the IPD or the DRU model is an extensive endeavor and implies a lot of additional algorithmic development.[26] The local electric field inducing the IPD or displacing the Drude charge does not only depend on the permanent charges, but also on the field *in situ* created by the other IPDs or Drude charges. Therefore, they have to be calculated in a self-consistent cycle. The final result of this process corresponds to the minimum of the polarisation energy. However, such a procedure is quite time-consuming. An economic alternative route is the Lagrange formalism,[20] which treats the IPDs or the positions of the Drude charges as additional degrees of freedom, for which appropriate equations of motion

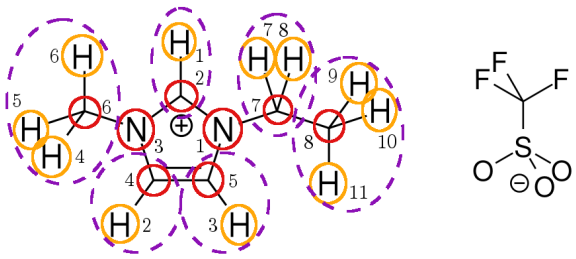

Figure 4.7 Structures of the cation $EMIM^+$ and the anion TfO^- used in this work. This figure also shows the hydrogen polarisation models of the cation $EMIM^+$. The circles illustrate which atoms are polarisable in the respective polarisation model: no hydrogen (only red), implicit hydrogen (purple), explicit hydrogen (red and orange).

are solved. This requires fictitious masses or moments of inertia to be attributed to the Drude particles or IPDs, respectively. The two sets of equations of motion for the permanent and induced particles are formally treated identically. Their thermostats, however, operate at quite different temperatures. The purpose of the thermostat governing the inducible part of the system is to keep it near the minimum of the polarisation energy. Consequently, the temperature is usually kept below 1 K.[20] Despite this dual thermostating, inductive electrostatics needs to be damped at close distances to avoid an uncontrollable increase of polarisation. This is usually done within the framework of the Thole algorithm.[43] Because of algorithmic complexity, prominent simulation packages usually focus on implementing either the IPD or the Drude oscillator model. Therefore, we used AMBER[216] (for IPD) as well as CHARMM[18] (for DRU) in our comparative study. Therefore, one has to pay attention to the differences inevitably arising between these two simulation packages.

A first difference results from the question, whether hydrogen atoms can be made polarisable or not. This affects only the cation of the IL $EMIM^+TfO^-$ chosen as our test system. While the IPD model in AMBER can explicitly handle polarisable hydrogen atoms, this cannot be done with the DRU model in CHARMM, as the hydrogen atoms and the Drude particles have comparable masses. This problem poses the second question, whether the hydrogen polarisability can be treated implicitly by adding it to the adjacent carbon atom. In this way, one can evade polarisable hydrogen atoms while still keeping the molecular polarisability the same. This creates four categories of polarisability distribution compared in this work. In the first case, all atoms are non-polarisable. Second, all non-hydrogen atoms are treated with their intrinsic polarisability. Third, all atoms are polarisable. And finally, the hydrogen polarisability is absorbed into the respective neighboring carbon atom. In the following, these four categories will be referred to as none, non-hydrogen, explicit hydrogen and implicit hydrogen.

1-ethyl-3-methyl-imidazolium				**Triflate**	
Atom	no H	implicit H	explicit H	Atom	α
N1	0.97157	0.97157	0.97157	C1	1.28860
C2	1.28860	1.70243	1.28860	F1	0.44475
N3	0.97157	0.97157	0.97157	F2	0.44475
C4	1.28860	1.70243	1.28860	F3	0.44475
C5	1.28860	1.70243	1.28860	S1	2.47445
H1	-	-	0.41383	O1	0.85197
H2	-	-	0.41383	O2	0.85197
H3	-	-	0.41383	O3	0.85197
C6	1.28860	2.53009	1.28860		
H4	-	-	0.41383		
H5	-	-	0.41383		
H6	-	-	0.41383		
C7	1.28860	2.11626	1.28860		
H7	-	-	0.41383		
H8	-	-	0.41383		
C8	1.28860	2.53009	1.28860		
H9	-	-	0.41383		
H10	-	-	0.41383		
H11	-	-	0.41383		
Sum	9.67474	14.22687	14.22687	**Sum**	7.65321

Table 4.5 Atomic polarisabilities[200] for the cation in the various polarisation models and the anion. The numbering of the atoms of the cation is shown in Fig. 4.7. Values are given in units of Å^3.

4.3.2 Methods

Simulation setup

This study is based on polarisable Molecular Dynamics (MD) simulations of the ionic liquid $EMIM^{+}TfO^{-}$. The parameters for the bonded and non-bonded interactions of the force field were taken from Pádua *et al.*[174,175]. The respective atomic polarisabilities for the above-mentioned four models are based upon van Duijnen and Swart[200] and are collected in Tab. 4.5. As this study is focused on a systematic study of different polarisability models, a possible recalibration of Lennard-Jones parameters was not done in order to keep parameter changes at a minimum.[24] With these values as a common input, we realized a suite of four polarisation models in AMBER 11[216] and three in CHARMM 38a2[18], where the explicit hydrogen model cannot be implemented. In addition to non-polarisable simulations, a series of polarisable simulations for each model was performed, thereby gradually changing the atomic polarisabilities in steps of ten percent up to their full value. Altogether, this comprised 52 simulations of varying length between 10 and 30 ns.

A non-polarisable system of 500 ion pairs in a cubic box was generated with PACKMOL.[79] After 20000 steps of energy minimization, a NpT equilibration run was performed at 300 K using the Berendsen barostat set to a reference pressure of 1 bar with a coupling constant of 1 ps, yielding an optimized box size of 54.6 Å. The final configuration served as the starting point for all subsequent NVT simulation runs. A uniform time step of 0.5 fs was used in all simulations. All bonds containing hydrogen atoms were constrained using the SHAKE algorithm[82]. The simulations were performed under periodic boundary conditions. Consequently, all electrostatic interactions were treated with the Particle Mesh Ewald method[80,81] using cubic splines of order 6 and a κ of 0.41 $Å^{-1}$. A grid with a spacing of approximately 1 Å was used in both cases. Instead of an SCF procedure to minimise the polariation energy, the Lagrange formalism was used with a dual thermostat keeping the system temperature near 300 K and the inducible part of the system below 1 K. The fictitious mass of the IPDs and the Drude particles were both set to 0.2 amu. A uniform Drude particle charge of $q^{\delta} = 2$ e was chosen. For the thermostat settings, the respective program default settings were used, i.e. Nosé-Hoover with τ=0.1 ps (300K) and τ=5 fs (1 K) in CHARMM and Berendsen with both τ set to 1 ps in AMBER.[162–164,217]

All analyses were carried out using a modified version of MDAnalysis[92]. Voronoi tessellations were calculated using the Voro++ library.[218]

Differences between CHARMM and AMBER

Before presenting the results, a brief summary of the differences between the IPD implementation in AMBER and the DRU implementation in CHARMM is given.

In the DRU model, the induced dipole moment $\vec{\mu}_{i,\beta}^{ind}$ assigned to atom β of molecule i is given by the product of the Drude charge q^{δ} times the displacement $\vec{d}_{i,\beta}$ of the two Drude

particles. Speaking in terms of atomic polarisabilities α_β, $\vec{\mu}_{i,\beta}^{ind}$ is given by

$$\vec{\mu}_{i,\beta}^{ind} = \alpha_\beta \vec{E}_{i,\beta}. \tag{4.16}$$

The principle equivalence between the IPD and Drude models can be shown by the way the local electric field $\vec{E}_{i,\beta}$ acting on atom β of molecule i is computed. In the Drude model, we have

$$\begin{aligned} \vec{E}_{i,\beta} &= \vec{E}_{i,\beta}^0 \\ &+ q^\delta \sum_j \sum_\gamma \left\{ \frac{\vec{r}_{i,\beta} - \vec{r}_{j,\gamma}}{|\,\vec{r}_{i,\beta} - \vec{r}_{j,\gamma}\,|^3} - \frac{\vec{r}_{i,\beta} - (\vec{r}_{j,\gamma} + \vec{d}_{j,\gamma})}{|\,\vec{r}_{i,\beta} - (\vec{r}_{j,\gamma} + \vec{d}_{j,\gamma})\,|^3} \right\}, \end{aligned} \tag{4.17}$$

where the summation runs over all Drude pairs γ of molecule j located at $\vec{r}_{j,\gamma}$ and $\vec{r}_{j,\gamma} + \vec{d}_{j,\gamma}$. The field exerted by the permanent charges is given by

$$\vec{E}_{i,\beta}^0 = \sum_j \sum_\gamma q_{j,\gamma} \frac{\vec{r}_{i,\beta} - \vec{r}_{j,\gamma}}{|\,\vec{r}_{i,\beta} - \vec{r}_{j,\gamma}\,|^3}. \tag{4.18}$$

For small displacements $\vec{d}_{j,\gamma}$, one can use the truncated Taylor expansion

$$\begin{aligned} &\frac{\vec{r}_{i,\beta} - (\vec{r}_{j,\gamma} + \vec{d}_{j,\gamma})}{|\,\vec{r}_{i,\beta} - (\vec{r}_{j,\gamma} + \vec{d}_{j,\gamma})\,|^3} = \\ &= \frac{\vec{r}_{i,\beta} - \vec{r}_{j,\gamma}}{|\,\vec{r}_{i,\beta} - \vec{r}_{j,\gamma}\,|^3} + \overleftrightarrow{T}_{\beta\gamma}(\vec{r}_{i,\beta} - \vec{r}_{j,\gamma}) \cdot \vec{d}_{j,\gamma} + \ldots \end{aligned} \tag{4.19}$$

with the dipole-dipole tensor

$$\overleftrightarrow{T}_{\beta\gamma}(\vec{r}_{i,\beta} - \vec{r}_{j,\gamma}) = \vec{\nabla}_{j,\gamma} \vec{\nabla}_{j,\gamma} \frac{1}{|\,\vec{r}_{i,\beta} - \vec{r}_{j,\gamma}\,|}. \tag{4.20}$$

Inserting Eq. 4.19 into Eq. 4.17 one gets

$$\vec{E}_{i,\beta} = \vec{E}_{i,\beta}^0 + \sum_j \sum_\gamma \overleftrightarrow{T}_{\beta\gamma}(\vec{r}_{i,\beta} - \vec{r}_{j,\gamma}) \cdot \vec{\mu}_{j,\gamma}^{ind}, \tag{4.21}$$

with the induced dipole $\vec{\mu}_{j,\gamma}^{ind} = q^\delta \vec{d}_{j,\gamma}$. Eq. 4.21 describes the IPD model. As long as the Taylor expansion in Eq. 4.19 is valid, it is equivalent to the Drude model in Eq. 4.17. Although the pair of Drude charges represents a physical dipole, it corresponds to a mathematical one, i.e. the IPD model, for small displacements. According to Eq. 4.16, higher atomic polarisabilities induce higher dipole moments in the IPD model or larger displacements in the Drude model. This deteriorates the validity of Eq. 4.19 and inevitably leads to deviations between physical and mathematical dipoles.

Simulations of polarisable systems may be prone to instabilities, if the short-range interaction between induced dipoles is not dampened. The Thole algorithm[43] provides a framework to achieve this and is implemented in most simulation packages, but the respective functional form and the threshold for its range may differ. Tab. II of Taylor *et al.*[219] lists the most fre-

	CHARMM						AMBER								
	no H			impl H			no H			impl H			expl H		
scale	$D^{\oplus}$	$\tau^{\oplus}_{avg}$	$\eta_{\oplus}$	$D^{\oplus}$	$\tau^{\oplus}_{avg}$	$\eta_{\oplus}$	$D^{\oplus}$	$\tau^{\oplus}_{avg}$	$\eta_{\oplus}$	$D^{\oplus}$	$\tau^{\oplus}_{avg}$	$\eta_{\oplus}$	$D^{\oplus}$	$\tau^{\oplus}_{avg}$	$\eta_{\oplus}$
0.0	2.16	625	71.3				2.24	643	66.9						
0.1	2.26	600	68.2	2.40	609	61.6	2.62	568	56.1	2.55	577	57.8	2.57	569	57.7
0.2	2.49	585	59.9	2.52	547	60.7	2.43	566	63.0	2.56	558	58.7	2.76	522	54.1
0.3	2.76	516	54.4	2.77	510	54.4	2.63	575	55.5	2.80	527	52.7	3.13	464	47.6
0.4	2.93	534	49.0	3.00	503	48.7	2.82	544	51.5	3.03	502	48.1	3.58	431	40.4
0.5	2.97	510	49.1	3.51	448	40.8	3.01	499	48.5	3.22	466	45.4	4.00	412	34.9
0.6	3.21	493	44.5	3.46	443	41.8	3.18	492	45.2	3.56	434	40.5	4.26	380	33.1
0.7	3.44	472	40.9	3.88	410	36.6	3.49	478	39.9	4.19	393	33.3	4.82	353	28.5
0.8	3.39	434	43.5	4.15	369	34.9	4.39	379	31.7	5.76	304	23.5	5.97	283	23.1
0.9	3.63	418	40.1	4.23	345	35.2	4.34	394	31.6	5.62	299	24.6	6.03	288	22.6
1.0	4.08	412	33.9	5.49	314	24.9	4.24	423	31.6	6.36	297	20.5	6.29	284	21.3

Table 4.6 The pseudo-viscosity $\eta_{\oplus}$ calculated from $D^{\oplus}$ and $\tau^{\oplus}_{avg}$ of the cation $EMIM^{+}$ using Eq. 4.27. $D^{\oplus}$ is given in units of 10^{-11} m^2 s^{-1}, $\tau^{\oplus}_{avg}$ in units of ps and $\eta_{\oplus}$ in units of mPa s.

quently used forms of Thole functions $\phi(r)$. The default settings of AMBER and CHARMM, which are $\phi_1(r)$ or $\phi_3(r)$, respectively, were used for the simulations presented here. AMBER would offer the possibility to use the same functional form $\phi_3(r)$, but CHARMM and AMBER would still differ with respect to the threshold of the range of the Thole functions. Because of this, the default settings of CHARMM and AMBER were kept.

As the Lagrange formalism requires a dual thermostat, as discussed above, and CHARMM and AMBER differ considerably in this regard, this may also be a source of differences. The elaborate Nosé-Hoover thermostat was used in CHARMM, which reliably kept both temperature baths close to the desired mean values. The Berendsen thermostat used in AMBER was not so accurate in this regard. At the highest levels of atomic polarisability, there was some heat exchange between the two baths with some flow of kinetic energy towards the induced dipoles, raising the temperature to a few K. This had a slight influence on the dynamics of the respective systems. Other parameters than the default settings did not improve this either. Therefore, we kept the default setting for all systems to maintain consistency.

4.3.3 Results and discussion

The following selection of results represents a mixture of traditionally given quantities in simulations of soft matter as well as other properties that were found to be quite indicative of the influence of polarisability. Thereby, the data are viewed from a threefold perspective: the systematic variation of polarisability in steps of ten percent, the difference between the IPD and DRU models and the question of the necessity of hydrogen polarisability.

Dynamics

As a first example, the mean square displacement (MSD) of the center-of-mass and the reorientation correlation function of the molecular dipole moment are given as typical representatives of single-particle translational and rotational motion. As done throughout this work, the numerical data were fitted to appropriate models of molecular motion to allow for better

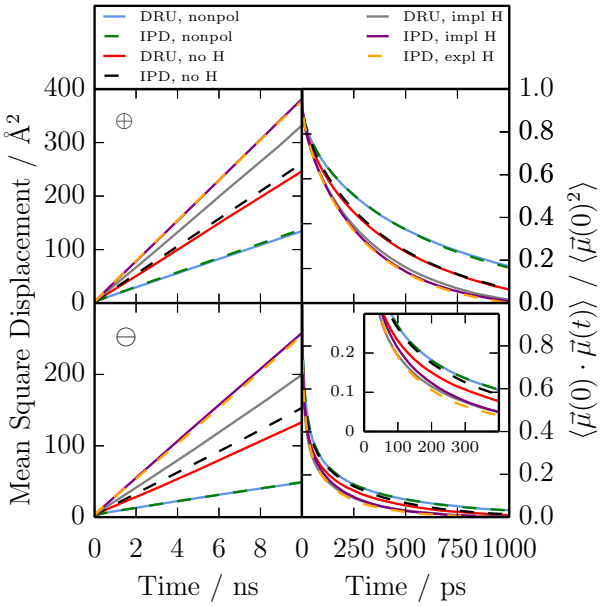

Figure 4.8 This figure shows a comparison of the single-particle dynamics for different polarisation models in CHARMM (DRU) and AMBER (IPD). The left column shows the single-particle mean square displacement, the right columns shows the normalised permanent dipole autocorrelation function. The upper row shows cation dynamics, the lower row anion dynamics. The inset in the lower right graph is a magnification to highlight the pattern of polarisation models.

quantification of the influence of polarisability. In the case of single-particle translation, the model function

$$\langle [\vec{R}_i(t) - \vec{R}_i(0)]^2 \rangle \cong 6D\sqrt{(t+\tau_0)^2 - \tau_0{}^2} \tag{4.22}$$

previously used by Gabl *et al.* [220] is applied. Throughout this work, the $\langle \ldots \rangle$ bracket notation is a shorthand for the ensamble average. Here, $\vec{R}_i(t)$ are the molecular center-of-mass coordinates at time t, D is the diffusion coefficient and τ_0 accounts for the non-linear behaviour at short times. τ_0 is a measure of the time required for the displacement to become linear. To describe single-particle rotation, the permanent dipole moment $\vec{\mu}_i$ of each molecule i was used. Since the species have a net charge, the molecular dipole moment depends on the origin of the chosen reference system. In accordance with earlier works,[221] each dipole moment is referenced to the respective molecular center of mass. Average values of the permanent dipole moment of $EMIM^+$ and TfO^- are 0.69 D and 6.37 D, respectively. The corresponding normalised time correlation function was fitted to a Kohlrausch-William-Watts (KWW) function of the form

$$\frac{\langle \vec{\mu}_i(t) \cdot \vec{\mu}_i(0) \rangle}{\langle \vec{\mu}_i(0)^2 \rangle} \cong e^{-(t/\tau)^\beta}. \tag{4.23}$$

This type of stretched exponential function characterises the diversity of dynamical processes by a single parameter β. Furthermore, an average τ can be obtained by the analytical expression

$$\tau_{avg} = \frac{\tau}{\beta}\,\Gamma\left(\frac{1}{\beta}\right), \tag{4.24}$$

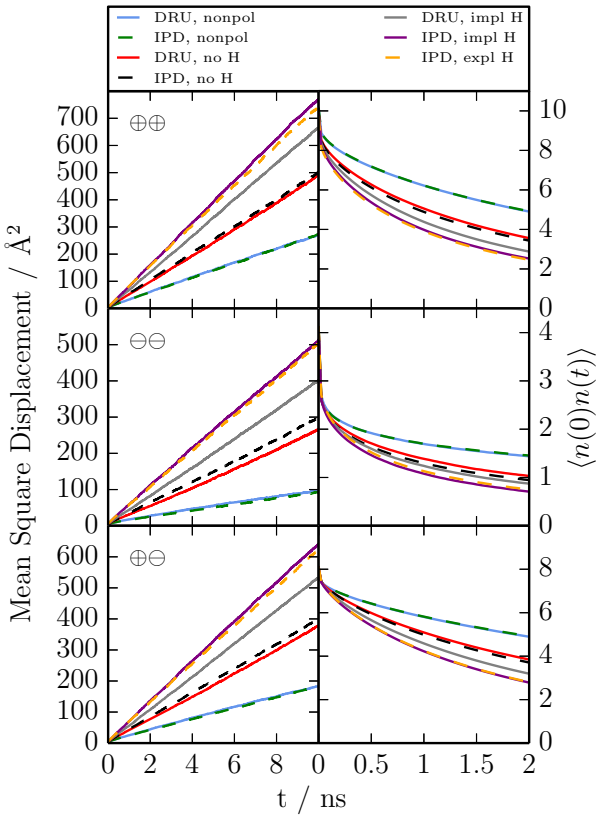

Figure 4.9 A comparison of pair and cage dynamics for different polarisability models implemented with the DRU and IPD models. The left column shows the mean square pair displacement $\langle[\vec{R}_{ij}(t) - \vec{R}_{ij}(0)]^2\rangle$, the right column shows the cage relaxation function $\langle n(0)n(t)\rangle$ of the first solvation shell with the initial value being the average coordination number $\langle CN\rangle$. The upper row shows the functions for cations with respect to other cations, the middle row for anions with respect to other anions and the lower row for cations with respect to anions or vice versa.

where Γ is the gamma function. The respective fit parameters are collected in Tabs. S1 and S2 in the Supplementary Material. Graphs of the results from the non-polarisable simulations and those performed at full strength of the respective polarisability models are shown in Fig. 4.8. As a general rule, dynamics is accelerated with increasing polarisability and a clear pattern can be found. First, AMBER and CHARMM yield equivalent results for the non-polarisable force field, both, in translation and rotation. Second, comparing the DRU and IPD polarisation models for the case of non-polarisable hydrogen atoms in terms of their implementation in CHARMM and AMBER, one still finds almost equivalent results. Third, upon implicit inclusion of hydrogen polarisability, i.e. absorbing it into the respective neighboring carbon atom, the results of CHARMM and AMBER start to deviate. As can be seen from Tab. 4.5, the implicit hydrogen model leads to very high polarisabilities of the carbon atoms, in some cases even exceeding that of sulfur. Considering Eqs. 4.16 - 4.21, it is shown that the DRU and IPD models must deviate beyond some threshold of polarisability. This seems to be the case here. Within AMBER, however, it does not matter whether hydrogen polarisability is modelled implicitly or explicitly, as both give equivalent results. Anyway, inclusion of hydrogen polarisability considerably raises the total sum of atomic polarisabilities, simply because of their large number (cf. Tab. 4.5). As a consequence, dynamics is accelerated accordingly.

The pattern described above can be found as well in the cases of pair dynamics and cage dynamics (see Fig. 4.9). Pair dynamics[220] is characterised by the mean square displacement of the center-of-mass distance of two molecules i and j

$$\begin{aligned}\langle[\vec{R}_{ij}(t)-\vec{R}_{ij}(0)]^2\rangle = \\ \langle[\vec{R}_i(t)-\vec{R}_i(0)]^2\rangle + \langle[\vec{R}_j(t)-\vec{R}_j(0)]^2\rangle \\ -2\langle[\vec{R}_i(t)-\vec{R}_i(0)]\cdot[\vec{R}_j(t)-\vec{R}_j(0)]\rangle.\end{aligned} \tag{4.25}$$

Again, the functional form given in Eq. 4.22 was used for fitting. The resulting parameters are collected in Tabs. S3 and S4 in the Supplementary Material. The data show clearly that the pair diffusion coefficient D^{ij} is the sum of the respective self diffusion coefficients $D^{ij} = D^i + D^j$. In other words, the cross-term appearing in Eq. 4.25 is negligible.[220] It is important to note, that this additivity holds for all polarisation models across all scales (cf. Tabs. S3 and S4 in the Supplementary Material). Combined with earlier findings,[220] the disappearance of cross-terms in the pair dynamics of binary ionic liquids seems to be a general rule. This is of importance for model theories of pair dynamics based on this assumption, e.g. model theories of the Nuclear Overhauser Effect in NMR spectroscopy.[220,222]

By cage dynamics, the relaxation of the solvation shell of a reference molecule is meant. In this case, the solvation shell is defined as the first Voronoi shell,[96,218] comprising all molecules with Delaunay distance one. A binary observable $n(t)$ is defined, depending on whether a molecule is at time t a member of a given Voronoi cage or not. The respective time correlation function $\langle n(0)n(t)\rangle$ is shown in Fig. 4.9. The initial value of this residence function is the average coordination number $\langle CN\rangle$, i.e. the average number of particles located within the first solvation shell. After subtracting the steady-state asymptotic value a_0, the integral is the

mean residence time τ_{cage}. The fit function[96]

$$\langle n(0)n(t)\rangle \cong a_1\, e^{-t/\tau_1} + (\langle CN\rangle - a_1)\, e^{-(t/\tau_2)^\beta} + a_0 \tag{4.26}$$

was used. Except for the $\ominus\ominus$ residence function, a_1 could be set to zero. The respective fit parameters are listed in Tabs. S5 and S6 in the Supplementary Material.

As shown above, the polarisability pattern appears in various aspects of dynamics: single-particle translation and rotation, pair displacement and cage residence function. This raises the question whether these properties may be traced back to a common quantity. For this purpose we used the hydrodynamical relationship[48]

$$\eta_\oplus = \frac{k_B T}{3\pi\sqrt{6}} \frac{1}{\sqrt{(D^\oplus)^3 \tau_{avg}^\oplus}} \tag{4.27}$$

to convert the diffusion coefficient $D^\oplus$ and the average reorientational time $\tau_{avg}^\oplus$ of the cation $EMIM^+$ to a pseudo-viscosity $\eta_\oplus$, which is not to be understood as the collective viscosity of the system. Here, $\eta_\oplus$ serves as a scaling factor for dynamical parameters involving the cations such as $1/D^\oplus$, $\tau_{avg}^\oplus$, $1/D^{\oplus\oplus}$, $1/D^{\oplus\ominus}$, $\tau_{cage}^{\oplus\oplus}$ and $\tau_{cage}^{\oplus\ominus}$. As such, $\eta_\oplus$ behaves much like the actual collective viscosity η, which can be applied as a global scaling factor for dynamical properties in homogeneous systems.[48] Rescaling the aforementioned dynamical parameters with $\eta_\oplus$, one finds almost uniform values across all polarisability scales. In other words, the influence of polarisability on dynamical parameters can be mapped to the underlying variations of the $\eta_\oplus$, i.e. $1/D^\oplus = c * \eta_\oplus$ etc. The applicability of Eq. 4.27 rests upon the constancy of the product $D^\oplus \cdot \tau_{avg}^\oplus$ inferred from hydrodynamics, which is fairly valid for $EMIM^+$, but not for TfO^-. Because of this, dynamical parameters involving only the anions scale less well, e.g. $\tau_{cage}^{\ominus\ominus}$, as will be discussed later. The resulting values for $\eta_\oplus$ are collected in Tab. 4.6 and graphically illustrated in Fig. 4.10. Thereby, not the scaling factor 0.0…1.0, but the total sum of the respective atomic polarisabilities of a single ion pair was used to compare polarisation models on a common scale. Inspired by the findings of Seddon *et al.*[223], that experimental viscosities follow an exponential law independent of the polarity of the added co-solvent, this law was adapted to the influence of polarisability on $\eta_\oplus$. The respective fit functions of the various polarisation models are also shown in Fig. 4.10. Indeed, all polarisation models, be they DRU or IPD, follow this experimentally inspired law and thus support the concept that polarisability acts as an inner solvent or co-solvent. Moreover, the DRU and IPD models lead to quite similar fit parameters, showing that they produce the same effects on dynamical observables.

As viscosity scaling stems from hydrodynamic diffusion tensors[48], its applicability is limited to time scales, where a system is diffusive in character. The model function given in Eq. 4.22 already indicates the typical non-diffusive behaviour exhibited by ionic liquids in the short-time regime. In order to gain a deeper insight, we have computed the van Hove self-correlation function[224,225] $G_s(r,t)$. This function shows the probability distribtion of the distance a given particle can travel within a certain time interval. The thick lines in Fig. 4.11

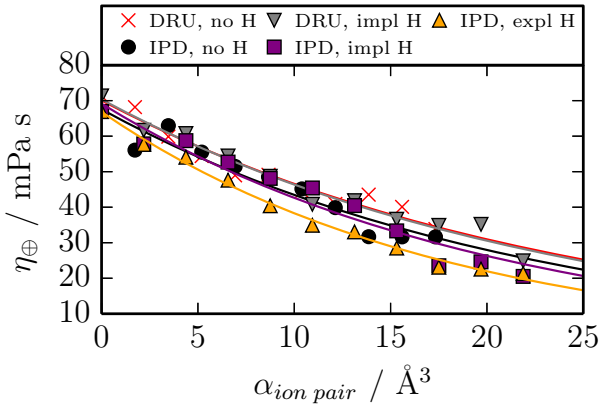

Figure 4.10 $\eta_\oplus$ is shown as a function of the sum of the respective atomic polarisabilities of an ion pair for the various polarisation models with the corresponding experimentally inspired fit function of the form $\eta_\oplus \cong a\, e^{-x/b}$. The fit parameters for the different models are: DRU, no H (a=70.0, b=24.5); DRU, impl H (a=70.3, b=24.0); IPD, no H (a=67.6, b=22.7); IPD, impl H (a=69.1, b=20.7); IPD, expl H (a=66.8, b=18.0).

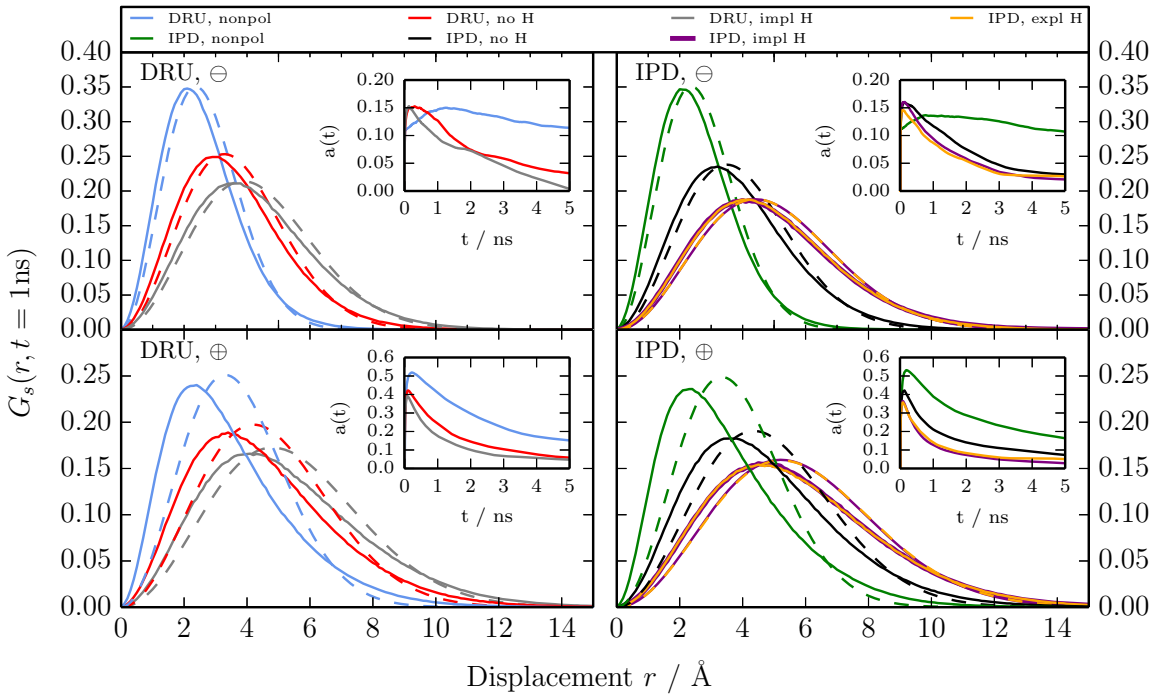

Figure 4.11 The van Hove self-correlation function $G_s(r,t)$[224,225] is shown as the thick lines for the different polarisation models in CHARMM and AMBER for a time interval of 1 ns. The respective expected Gaussian forms $G_s^0(r,t)$ (cf. Eq. 4.28) are shown as dashed lines of the same color. The insets show the functional form of the corresponding non-Gaussian parameter $a(t)$ (cf. Eq. 4.29).

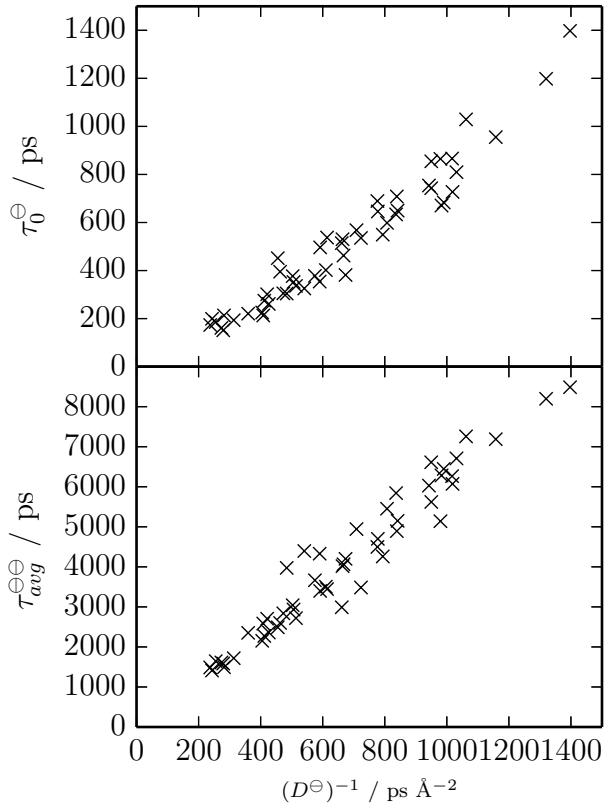

Figure 4.12 Scatter plots showing the correlation of $1/D^{\ominus}$ to $\tau_0^{\ominus}$ (upper panel) and $\tau_{avg}^{\ominus\ominus}$ (lower panel) for all polarisation models in CHARMM and AMBER.

show this function for all polarisation models at time t = 1 ns. With increasing total polarisability of the model, the distribution of accessible distance widens and the maximum of the distribtion shifts to higher distances, thus reflecting the increasing fluidity of the system. For a purely diffusive behaviour, one would expect $G_s(r,t)$ to follow a Gaussian form[224]

$$G_s^0(r,t) = \left(\frac{3\pi}{2}\langle|\Delta\vec{r}(t)|^2\rangle\right)^{\frac{3}{2}} e^{-3r^2/(2\langle|\Delta\vec{r}(t)|^2\rangle)}. \tag{4.28}$$

The corresponding curves are shown as dashed lines in Fig. 4.11. As a measure of the deviation of the actual data from Gaussian behaviour, one usually computes the non-Gaussian parameter:[224,226]

$$a(t) = \frac{3}{5}\frac{\langle|\Delta\vec{r}(t)|^4\rangle}{\langle|\Delta\vec{r}(t)|^2\rangle^2} - 1. \tag{4.29}$$

The larger $a(t)$ becomes, the more pronounced is the non-Gaussian behaviour of the system. As can be seen from the insets in Fig. 4.11, $a(t)$ reaches a maximum at very short times and then decays monotonically. For more complex polarisability models, this maximum clearly shifts to shorter times and also the decay is enhanced. In other words, the system comes closer to Gaussian behaviour and is thus more diffusive in character. Again, it is important to note, that the implicit and the explicit hydrogen models behave almost identically.

While the dynamics of the cation $EMIM^+$ could be mapped to $\eta_\oplus$, an analogous procedure for the anion did not work well. To further elucidate this, the non-Gaussian diffusive behaviour of the anions has to be studied. It can be quantified by two parameters, $\tau_0^\ominus$ of Eq. 4.22 and the time t_{max}, where $a(t)$ (cf. Eq. 4.29) reaches its maximum. Both parameters are a measure for the time interval needed to enter the Gaussian diffusive regime. Indeed, they are pretty close in absolute value, bearing in mind that both are difficult to determine. This raises the question, how the Gaussian and non-Gaussian diffusive regimes are correlated. In fact, Fig. 4.12 shows strong correlation between $1/D^\ominus$ and $\tau_0^\ominus$. In other words, the slower translational motion is, the longer it takes to reach the Gaussian diffusive regime. The fact that even $\tau_0^\ominus$ or t_{max} is proportional to $1/D^\ominus$ across all polarisability scales highlights the central role of the diffusion coefficient for the dynamics of the anions. Indeed, also $\tau_{avg}^{\ominus\ominus}$ can be rescaled following $1/D^\ominus$ (see Fig. 4.12). Therefore, while viscosity scaling across polarisability scales is not possible for anion dynamics due to the different rates of change of $D^\ominus$ and $\tau_{avg}^\ominus$ (cf. Tabs. S1 and S2 in the Supplementary Material), scaling by $D^\ominus$ is a working substitute.

Structure

From cage dynamics we have learned that the initial value of the residence function $\langle n(0)\cdot n(t)\rangle$, representing the average coordination number $\langle CN\rangle$, is rather insensitive to polarisability. However, coordination numbers are integrals of solvation shell-resolved pair correlation functions $g^{000}(r)$ between molecular centers-of-mass R_{ij}. Consequently, a possible dependence of $g^{000}(r)$ on polarisability may compensate upon integration. Therefore, $g^{000}(r)$ for

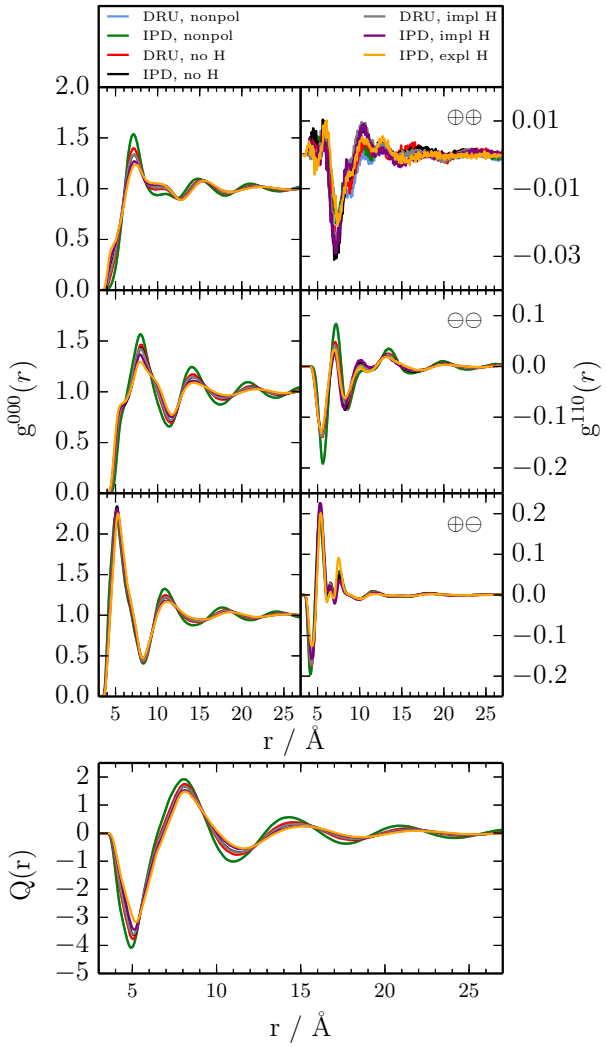

Figure 4.13 The left column of the upper panel shows the functional form of the radial distribution function $g^{000}(r)$, the right column of the upper panel shows the orientational correlation function $g^{110}(r)$. Both are given for the center-of-mass distances of each, cations around cations, anions around anions or cations around anions or vice versa. The lower panel shows the charge ordering function $Q(r)$. All functions are shown for the non-polarisable case and at full strength of all polarisation models, each in CHARMM and AMBER.

the combinations $\oplus\oplus$, $\ominus\ominus$ and $\oplus\ominus$ is studied at full radial resolution

$$g^{000}(r) = \frac{1}{\rho\ 4\pi r^2 dr} \sum_{j=1}^{N} \langle \delta(r - |R_{ij}|) \rangle. \tag{4.30}$$

This function measures the deviation of the local particle density within a spherical shell of thickness dr from the uniform particle density ρ and thus is an indicator of molecular packing. The mutual orientation of molecules at a distance R_{ij} is characterised by

$$g^{110}(r) = \frac{1}{\rho\ 4\pi r^2 dr} \sum_{j=1}^{N} \left\langle \frac{\vec{\mu}_i \cdot \vec{\mu}_j}{|\vec{\mu}_i| \cdot |\vec{\mu}_j|} \delta(r - |R_{ij}|) \right\rangle, \tag{4.31}$$

where $\vec{\mu}_i$ and $\vec{\mu}_j$ are the respective permanent molecular dipole moments. $g^{110}(r)$ is an extension of $g^{000}(r)$ in that it weights the local density by the cosine of the angle between the two dipole vectors.[221]

The respective graphs of $g^{000}(r)$ and $g^{110}(r)$ are given in Fig. 4.13. For the purpose of discussion, three regions may be discerned: the immediate short range below 5 Å, the region around the highest peak from 5 to 10 Å and the long range order beyond 10 Å. With increasing polarisability, a shoulder emerges in the immediate short range for like species, $\oplus\oplus$ and $\ominus\ominus$, while at the same time, the highest peak is reduced in height. This corresponds to the concept of polarisability acting as an inner solvent by screening the repulsive electrostatic forces between like-charged molecules. For unlike charges $\oplus\ominus$, $g^{000}(r)$ below 10 Å is largely unaffected by polarisability changes. Without polarisable hydrogen atoms, the DRU and IPD models largely agree. Including hydrogen polarisability explicitly or implicitly further pronounces the effects described above with even stronger effects in the explicit case. However, for implicit hydrogen polarisability, CHARMM and AMBER deviate.

In the asymptotic region beyond 10 Å, the set of $g^{000}(r)$ functions exhibit an increasingly regular pattern of structural oscillations. The individual onset of this behaviour goes along with the vanishing of the orientational correlation function $g^{110}(r)$. For unlike charges, orientational structure disappears at shorter distances than for like charges, although it should be noted that $g^{110}_{\oplus\oplus}$ shows almost no correlation. Since a fortuitous 90 degree conformation - nullifying the cosine - has been ruled out by further analysis (data not shown), this effect comes from a lack of orientational steering between the cations caused by their comparatively small dipole moment. If the onset of the regular oscillation pattern in packing correlates with the vanishing of orientational correlation, then this behaviour can be interpreted as the transition from that of anisotropic molecular ions to pseudo-spherical ions. In the latter case, the oscillations of like and unlike ions are synchronised with a coincidence of respective maxima and minima. The charge ordering function

$$Q(r) = g^{000}_{\oplus\oplus}(r) + g^{000}_{\ominus\ominus} - 2g^{000}_{\oplus\ominus} \tag{4.32}$$

by design rationalizes this oscillation pattern and is a measure of the surplus or deficit of like

	CHARMM								AMBER											
	no H				impl H				no H				impl H				expl H			
scale	A	$1/\sigma$	λ	ϕ	A	$1/\sigma$	λ	ϕ	A	$1/\sigma$	λ	ϕ	A	$1/\sigma$	λ	ϕ	A	$1/\sigma$	λ	ϕ
0.0	30.0	0.087	6.43	25.1					29.8	0.086	6.42	25.1								
0.1	30.2	0.089	6.44	25.1	30.1	0.089	6.45	25.1	30.0	0.088	6.45	25.1	30.3	0.090	6.44	25.1	30.3	0.090	6.44	25.1
0.2	30.5	0.091	6.46	25.1	30.6	0.092	6.46	25.1	30.4	0.091	6.45	25.1	30.6	0.093	6.47	25.1	30.8	0.093	6.46	25.1
0.3	30.6	0.093	6.47	25.1	31.0	0.096	6.48	25.1	30.8	0.094	6.47	25.1	31.1	0.098	6.49	25.1	31.1	0.097	6.48	25.1
0.4	30.9	0.096	6.47	25.1	31.0	0.098	6.49	25.1	31.3	0.098	6.49	25.1	31.2	0.102	6.51	25.0	31.3	0.100	6.49	25.1
0.5	30.9	0.096	6.49	25.1	31.6	0.102	6.51	25.1	31.4	0.101	6.50	25.1	31.9	0.108	6.55	25.1	32.1	0.105	6.53	25.1
0.6	31.0	0.099	6.50	25.1	31.6	0.104	6.53	25.1	31.9	0.105	6.52	25.1	32.2	0.112	6.57	25.0	32.8	0.112	6.55	25.1
0.7	31.6	0.103	6.51	25.1	32.2	0.109	6.55	25.1	32.3	0.109	6.54	25.1	32.3	0.117	6.60	25.0	33.2	0.117	6.57	25.1
0.8	32.0	0.107	6.53	25.1	32.2	0.111	6.56	25.1	32.3	0.112	6.56	25.1	32.6	0.123	6.63	25.0	33.6	0.124	6.61	25.1
0.9	32.3	0.110	6.54	25.1	32.4	0.114	6.54	25.0	33.2	0.118	6.59	25.1	33.2	0.130	6.66	25.0	34.6	0.132	6.65	25.1
1.0	32.4	0.112	6.56	25.1	32.7	0.120	6.61	25.1	33.5	0.123	6.62	25.1	33.8	0.138	6.68	25.0	35.4	0.140	6.70	25.1

Table 4.7 Parameters of the fit to the charge ordering function $Q(r)$ using the fit function $Q_{fit}(r)$ (cf. Eqs. 4.32 and 4.33) for all polarisation models in CHARMM and AMBER.

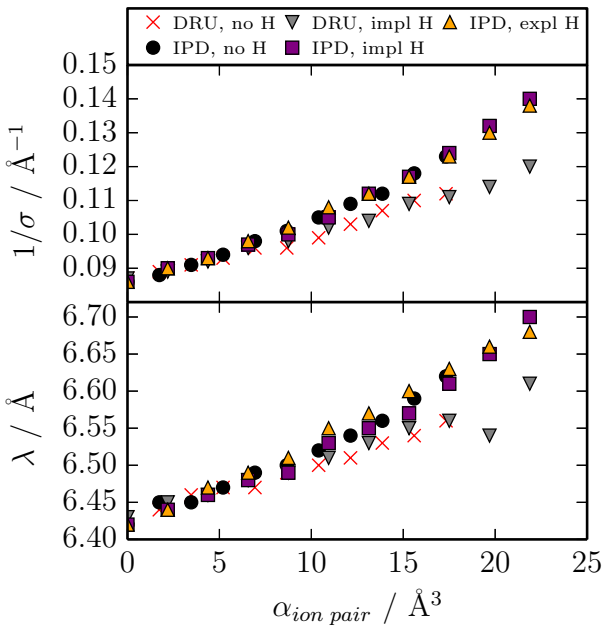

Figure 4.14 The charge ordering function fit parameters $1/\sigma$ and λ (cf. Eq. 4.33) shown as a function of the total sum of the respective atomic polarisabilities for all polarisability models in CHARMM and AMBER.

charged ions at distance r. $Q(r)$ can be fitted to the function[227]

$$Q_{fit}(r) = \frac{A}{r} e^{-r/\sigma} sin\left(\frac{2\pi r}{\lambda} + \phi\right). \tag{4.33}$$

As this function only describes the oscillating pattern just discussed, the fit can only be used beyond some threshold, in our case 5 Å. The respective fit parameters are collected in Tab. 4.7. The functions $Q(r)$ shown for selected systems in the lower panel of Fig. 4.13 illustrate the effect of polarisability. Quite intriguingly, the two hydrogen models, implcit and explicit, give a highly similar form of $Q(r)$. This shows, that for longer distances, the individual location of the hydrogen polarisabilities is less relevant than for shorter distances, but their inclusion is important nonetheless. As a general feature, increase of polarisability dampens the oscillations of the function. This can be quantified by the fit parameter $1/\sigma$, which increases monotonically. When again plotted as a function of the total sum of the polarisabilities of an ion pair, only two separate curves are observed (cf. the upper panel of Fig. 4.14). All hydrogen polarisability models - none, implicit or explicit - lie on the same curve, the only difference being between CHARMM and AMBER, i.e. between the DRU and IPD models. The overall trend for both models is quite the same, but it is less pronounced in CHARMM. Still, damping alone is not a sufficient description of the observed changes: when integrating over successive radial shells $\int_0^\infty Q(r) 4\pi r^2 dr$, the final cumulative value has to be independent of the polarisation model. This balance is conserved by the increase of the wavelength of the oscillations, described by the fit parameter λ (cf. the lower panel of Fig. 4.14), which shows the same pattern for the DRU and IPD models as $1/\sigma$. A higher λ shifts

the peaks of $Q(r)$ slightly outwards, where they are weighted with a higher r^2. In this way, the higher dampening is compensated. Thus, with increasing polarisability and the ensuing screening of electrostatic interaction, the long range charge ordering is less pronounced. In this sense, inductive effects make an ionic liquid behave more like a neutral molecular liquid.

4.3.4 Conclusion

In this paper, the influence of polarisability on the structure and dynamics of liquid systems is studied, using the ionic liquid $EMIM^+TfO^-$ as a test case. Three aspects have been highlighted: a systematic variation of the strength of polarisability, a comparison of the Drude oscillator model (DRU) and the induced point-dipole model (IPD) as implemented in CHARMM and AMBER, respectively as well as the special influence of hydrogen polarisability.

Concerning the variation of the polarisability, the total sum of polarisabilities of an ion pair turned out to be the common scale for the various polarisability models. The general influence of polarisability is to make the liquid more fluid and less structured. The effect on dynamics can be rationalized by introducing a common scaling factor $\eta_\oplus$, derived from hydrodynamical relationships involving the cationic diffusion coefficient $D^\oplus$ and reorientational time $\tau^\oplus_{avg}$. As the variation of many dynamical observables with increasing polarisability can be mapped to corresponding changes in $\eta_\oplus$, it may serve as a central quantity representing dynamics. The systematic loss of structure was quantified using the charge ordering function $Q(r)$ as a measure of alternating charge layers. Its behaviour upon raising the polarisability can be characterised by a pair of parameters, the damping factor $1/\sigma$ and the wavelength λ. From these parameters one can read, that the alternating charge layers increase in width. This partial penetration reduces maxima and minima of $Q(r)$. Thus, an increase in polarisability creates screening of electrostatic interaction and leads to a loss of long-range order. However, inclusion of polarisability does not change the short-range structural features of the liquid in a qualitative manner. In fact, these features are only less pronounced due to the aforementioned electrostatic screening. Both the damping of the structure as well as the increase in dynamics may be attributed to this screening. As the molecular packing becomes looser and the particles gain more freedom to move, dynamics is accelerated significantly, but the accessible configurations remain quite the same.

When comparing the different hydrogen polarisability models - non-polarisable, explicitly polarisable or implicitly polarisable hydrogen atoms - the importance of their inclusion becomes obvious. The way of inclusion - explicitly or implicitly - is not so important. This opens up the possibility to include hydrogen polarisability in the DRU model, where explicitly polarisable hydrogen atoms are methodically unfeasible. As the inclusion of hydrogens raises the total sum of polarisabilities, the effects on structure and dynamics described above are further increased according to this common scale.

With respect to the method of implementing polarisability - the DRU model in CHARMM or the IPD model in AMBER - it could be shown, that both models are equivalent at least in a qualitative sense. Trends in all observables are highly similar, although the results begin to deviate at the highest polarisability levels. This is most obvious, when comparing the implicit

hydrogen model, where the highest atomic polarisabilities are achieved, between CHARMM and AMBER. Generally, the IPD model in AMBER seems to have a slightly higher impact on the observables described here.

In addition to the principle equivalence of the Drude oscillator and the induced point-dipole models, the inclusion of polarisability in general may be seen as adding an inner solvent or co-solvent, in that via screening electrostatic interactions, dynamics is accelerated and structure is loosened.

Acknowledgment

We would like to thank the Vienna Scientific Cluster (http://www.zid.tuwien.ac.at/vsc) for the generous allocation of computer time. This work was funded by the Austrian Science Fund FWF in the context of Project No. P23494,by the Cost Action CM 1206: "Exchange on ionic liquids" and the SafeBatt project of the BMBF (Project No. 03X4631N).

4.3.5 Supporting Information

CHARMM	⊕ translation			⊖ translation			⊕ rotation			⊖ rotation		
model	D	τ_0	t_{max}	D	τ_0	t_{max}	τ	β	τ_{avg}	τ	β	τ_{avg}
nonpol	2.16	318	215	0.72	1400	1240	478	0.68	625	55.8	0.43	153
no H, 0.1	2.26	299	250	0.86	955	1380	467	0.69	600	54.0	0.42	156
no H, 0.2	2.49	265	183	0.98	727	1360	457	0.69	585	50.9	0.43	144
no H, 0.3	2.76	200	218	1.05	854	1420	415	0.71	516	48.2	0.42	141
no H, 0.4	2.93	130	203	1.19	650	878	424	0.70	534	48.1	0.41	149
no H, 0.5	2.97	222	163	1.29	646	588	394	0.68	510	45.5	0.42	130
no H, 0.6	3.21	155	175	1.50	463	633	389	0.70	493	44.9	0.42	133
no H, 0.7	3.44	111	120	1.64	402	480	377	0.71	472	44.2	0.43	124
no H, 0.8	3.39	209	113	1.69	496	425	348	0.71	434	42.9	0.43	121
no H, 0.9	3.63	234	105	1.99	377	373	343	0.73	418	42.4	0.43	116
no H, 1.0	4.08	72.7	108	2.11	305	303	331	0.71	412	40.6	0.43	114
impl H, 0.1	2.40	231	158	1.01	684	1460	472	0.69	609	53.7	0.43	152
impl H, 0.2	2.52	259	275	0.94	1030	635	427	0.69	547	50.2	0.43	140
impl H, 0.3	2.77	204	190	1.24	599	605	408	0.71	510	45.8	0.42	133
impl H, 0.4	3.00	233	230	1.29	689	670	398	0.70	503	43.6	0.42	129
impl H, 0.5	3.51	140	150	1.69	354	900	361	0.71	448	40.8	0.42	117
impl H, 0.6	3.46	155	120	1.63	537	320	354	0.71	443	39.9	0.43	111
impl H, 0.7	3.88	131	128	1.98	352	800	328	0.71	410	37.6	0.42	107
impl H, 0.8	4.15	125	118	2.16	395	610	304	0.73	369	35.9	0.43	100
impl H, 0.9	4.23	172	113	2.20	452	168	285	0.74	345	33.6	0.43	92.4
impl H, 1.0	5.49	54.2	85.0	3.19	193	125	259	0.74	314	31.7	0.44	82.7

Table 4.8 MSD and $\langle\vec{\mu}(0)\cdot\vec{\mu}(t)\rangle/\langle\vec{\mu}(0)^2\rangle$ fit parameters of all CHARMM simulations. D is given in units of 10^{-11} m^2 s^{-1}, τ_0, t_{max}, τ and τ_{avg} in units of ps. The first column lists the polarisability model and the respecitve strength of polarisabilities.

AMBER model	⊕ translation			⊖ translation			⊕ rotation			⊖ rotation		
	D	τ_0	t_{max}	D	τ_0	t_{max}	τ	β	τ_{avg}	τ	β	τ_{avg}
nonpol	2.24	282	185	0.76	1200	740	491	0.68	643	55.8	0.42	160
no H, 0.1	2.62	136	228	0.97	809	763	449	0.70	568	52.8	0.42	150
no H, 0.2	2.43	302	178	0.98	866	883	446	0.70	566	51.7	0.42	147
no H, 0.3	2.63	193	153	1.06	754	440	446	0.69	575	52.2	0.42	148
no H, 0.4	2.82	221	220	1.19	708	860	419	0.68	544	50.2	0.42	147
no H, 0.5	3.01	182	153	1.48	382	618	403	0.72	499	48.9	0.43	139
no H, 0.6	3.18	183	170	1.51	530	745	394	0.71	492	49.7	0.43	139
no H, 0.7	3.49	124	120	1.74	378	213	388	0.72	478	49.7	0.43	139
no H, 0.8	4.39	85.6	113	2.45	213	305	314	0.74	379	42.8	0.43	115
no H, 0.9	4.34	97.9	120	2.47	225	143	328	0.74	394	47.6	0.44	123
no H, 1.0	4.24	114	123	2.43	275	128	344	0.72	423	50.9	0.44	132
impl H, 0.1	2.55	232	253	1.02	671	1440	450	0.69	577	51.0	0.43	144
impl H, 0.2	2.56	255	173	1.02	865	1340	428	0.68	558	48.6	0.42	138
impl H, 0.3	2.80	221	160	1.26	550	628	419	0.70	527	47.8	0.43	135
impl H, 0.4	3.03	185	143	1.38	536	660	403	0.71	502	45.9	0.43	129
impl H, 0.5	3.22	153	175	1.51	514	550	383	0.73	466	44.3	0.42	130
impl H, 0.6	3.56	175	135	1.95	336	428	357	0.73	434	43.9	0.44	117
impl H, 0.7	4.19	121	133	2.35	261	328	322	0.73	393	40.8	0.43	111
impl H, 0.8	5.76	80.7	78.0	3.58	151	150	250	0.73	304	33.1	0.45	82.3
impl H, 0.9	5.62	145	75.0	3.55	213	100	252	0.75	299	35.2	0.45	86.1
impl H, 1.0	6.36	66.5	78.0	4.21	173	133	248	0.75	297	36.9	0.47	85.0
expl H, 0.1	2.57	205	201	1.05	743	1720	447	0.70	569	50.5	0.43	140
expl H, 0.2	2.76	213	205	1.20	634	910	409	0.69	522	45.7	0.43	127
expl H, 0.3	3.13	185	118	1.41	568	478	379	0.72	464	42.5	0.44	113
expl H, 0.4	3.58	125	140	1.85	326	355	348	0.72	431	39.9	0.44	104
expl H, 0.5	4.00	78.1	105	2.07	304	340	335	0.72	412	38.0	0.44	101
expl H, 0.6	4.26	116	100	2.38	301	253	314	0.73	380	36.0	0.44	94.0
expl H, 0.7	4.82	90.7	105	2.78	221	408	288	0.72	353	34.6	0.45	86.3
expl H, 0.8	5.97	69.3	95.0	3.66	161	163	237	0.75	283	29.0	0.46	68.7
expl H, 0.9	6.03	77.9	70.0	3.92	186	125	243	0.76	288	31.7	0.47	72.7
expl H, 1.0	6.29	92.5	80.0	4.11	199	68	242	0.76	284	33.1	0.47	76.0

Table 4.9 MSD and $\langle\vec{\mu}(0)\cdot\vec{\mu}(t)\rangle/\langle\vec{\mu}(0)^2\rangle$ fit parameters of all AMBER simulations. D is given in units of 10^{-11} m^2 s^{-1}, τ_0, t_{max}, τ and τ_{avg} in units of ps. The first column lists the polarisability model and the respecitve strength of polarisabilities.

CHARMM model	$\oplus\oplus$ $D^{\oplus\oplus}$	$\tau_0^{\oplus\oplus}$	$D^{\oplus}+D^{\oplus}$	$\ominus\ominus$ $D^{\ominus\ominus}$	$\tau_0^{\ominus\ominus}$	$D^{\ominus}+D^{\ominus}$	$\oplus\ominus$ $D^{\oplus\ominus}$	$\tau_0^{\oplus\ominus}$	$D^{\oplus}+D^{\ominus}$
nonpol	4.48	267	4.33	1.55	1250	1.43	3.01	485	2.88
no H, 0.1	4.79	218	4.52	1.75	959	1.73	3.30	376	3.12
no H, 0.2	5.13	270	4.97	1.98	1010	1.96	3.60	429	3.47
no H, 0.3	5.42	189	5.52	2.08	867	2.11	3.74	356	3.81
no H, 0.4	5.77	189	5.86	2.32	841	2.38	4.05	349	4.12
no H, 0.5	5.78	201	5.94	2.46	623	2.57	4.12	318	4.25
no H, 0.6	6.54	173	6.41	2.94	502	3.00	4.73	269	4.71
no H, 0.7	6.77	117	6.88	3.35	307	3.28	5.07	174	5.08
no H, 0.8	6.95	189	6.79	3.53	397	3.38	5.24	256	5.08
no H, 0.9	7.38	220	7.26	3.90	442	3.98	5.63	296	5.62
no H, 1.0	7.92	96.2	8.17	4.16	284	4.23	6.05	155	6.20
impl H, 0.1	4.70	383	4.81	2.06	751	2.02	3.40	476	3.41
impl H, 0.2	5.00	278	5.03	1.89	1040	1.88	3.44	466	3.46
impl H, 0.3	5.57	202	5.54	2.49	590	2.48	4.04	309	4.01
impl H, 0.4	6.03	225	6.00	2.59	697	2.58	4.31	355	4.29
impl H, 0.5	6.99	150	7.01	3.33	329	3.39	5.15	207	5.20
impl H, 0.6	6.83	234	6.93	3.24	562	3.26	5.03	337	5.09
impl H, 0.7	7.69	152	7.77	3.97	362	3.95	5.83	221	5.86
impl H, 0.8	8.41	62.4	8.31	4.36	345	4.32	6.39	148	6.31
impl H, 0.9	8.60	90.4	8.45	4.49	334	4.39	6.55	168	6.42
impl H, 1.0	11.2	33.0	11.0	6.44	170	6.39	8.80	79.9	8.68

Table 4.10 Fit parameters for the pair displacement $\langle[\vec{R}_{ij}(t)-\vec{R}_{ij}(0)]^2\rangle$ for all CHARMM simulations. D is given in units of 10^{-11} m^2 s^{-1}, τ_0 in units of ps. The parameters show that each pair diffusion coefficient is roughly the sum of the respective single-particle diffusion coefficients of the two species.

AMBER model	$\oplus\oplus$ $D^{\oplus\oplus}$	$\tau_0^{\oplus\oplus}$	$D^{\oplus}+D^{\oplus}$	$\ominus\ominus$ $D^{\ominus\ominus}$	$\tau_0^{\ominus\ominus}$	$D^{\ominus}+D^{\ominus}$	$\oplus\ominus$ $D^{\oplus\ominus}$	$\tau_0{}_{\oplus\ominus}$	$D^{\oplus}+D^{\ominus}$
nonpol	4.32	311	4.47	1.38	1450	1.52	2.85	2.99	545
no H, 0.1	5.07	155	5.25	1.83	1030	1.94	3.45	3.59	353
no H, 0.2	4.71	241	4.86	1.80	901	1.97	3.26	3.41	401
no H, 0.3	5.09	219	5.26	2.08	701	2.12	3.58	3.69	348
no H, 0.4	5.59	182	5.63	2.30	784	2.38	3.95	4.01	338
no H, 0.5	5.92	229	6.03	2.96	417	2.97	4.44	4.50	288
no H, 0.6	6.45	177	6.36	3.00	543	3.01	4.72	4.68	285
no H, 0.7	6.98	96.8	6.97	3.34	379	3.48	5.16	5.23	183
no H, 0.8	8.73	85.2	8.78	4.85	211	4.90	6.78	6.84	130
no H, 0.9	8.48	124	8.67	4.79	263	4.94	6.64	6.80	171
no H, 1.0	8.29	118	8.47	4.69	306	4.86	6.49	6.67	182
impl H, 0.1	4.87	287	5.11	1.84	928	2.03	3.35	3.57	446
impl H, 0.2	5.00	281	5.12	1.91	1070	2.04	3.45	3.58	476
impl H, 0.3	5.44	259	5.60	2.43	604	2.52	3.93	4.06	362
impl H, 0.4	5.71	185	6.05	2.60	563	2.77	4.16	4.41	295
impl H, 0.5	6.20	159	6.44	3.03	452	3.02	4.62	4.73	249
impl H, 0.6	7.01	164	7.13	3.88	272	3.89	5.44	5.51	203
impl H, 0.7	8.07	123	8.39	4.45	286	4.69	6.26	6.54	179
impl H, 0.8	11.3	97.5	11.5	6.75	199	7.16	9.00	9.34	134
impl H, 0.9	11.1	144	11.3	7.02	176	7.10	9.04	9.17	158
impl H, 1.0	12.9	65.0	12.7	8.56	169	8.42	10.7	10.6	106
expl H, 0.1	4.76	329	5.14	1.86	942	2.11	3.32	3.62	485
expl H, 0.2	5.63	198	5.53	2.41	651	2.39	4.02	3.96	324
expl H, 0.3	6.32	175	6.26	2.70	661	2.82	4.50	4.54	309
expl H, 0.4	7.10	172	7.15	3.60	351	3.70	5.34	5.43	230
expl H, 0.5	7.85	86.1	8.00	4.03	307	4.13	5.94	6.07	155
expl H, 0.6	8.30	120	8.53	4.64	330	4.75	6.46	6.64	192
expl H, 0.7	9.21	106	9.65	5.43	243	5.56	7.31	7.60	156
expl H, 0.8	11.9	76.1	12.0	7.18	170	7.31	9.50	9.63	111
expl H, 0.9	12.3	42.9	12.1	7.95	135	7.84	10.1	9.95	78.2
expl H, 1.0	12.3	113	12.6	8.22	187	8.22	10.3	10.4	141

Table 4.11 Fit parameters for the pair displacement $\langle[\vec{R}_{ij}(t)-\vec{R}_{ij}(0)]^2\rangle$ for all AMBER simulations. D is given in units of 10^{-11} m^2 s^{-1}, τ_0 in units of ps. The parameters show that each pair diffusion coefficient is roughly the sum of the respective single-particle diffusion coefficients of the two species.

CHARMM model	⊕⊕ ⟨CN⟩	τ	β	a_0	τ_{avg}	⊖⊖ ⟨CN⟩	a_1	τ_1	τ_2	β	a_0	τ_{avg}	⊕⊖ ⟨CN⟩	τ	β	a_0	τ_{avg}
nonpol	10.1	3350	0.57	0.00	5450	4.11	1.45	9.97	5760	0.47	0.00	8490	7.05	5410	0.77	0.45	6310
no H, 0.1	10.1	3290	0.57	0.00	5370	4.12	1.45	10.0	5240	0.49	0.00	7190	7.07	5330	0.78	0.40	6140
no H, 0.2	10.1	2930	0.57	0.01	4750	4.12	1.45	10.0	4680	0.50	0.00	6070	7.21	4960	0.77	0.32	5780
no H, 0.3	10.1	2660	0.57	0.04	4290	4.11	1.46	10.0	4260	0.49	0.00	5620	7.32	4570	0.76	0.24	5380
no H, 0.4	10.1	2480	0.57	0.10	3980	4.10	1.45	10.3	4090	0.51	0.00	5150	7.11	4290	0.79	0.40	4920
no H, 0.5	10.1	2320	0.57	0.13	3790	4.09	1.46	10.4	3740	0.51	0.00	4700	7.33	4160	0.75	0.27	4960
no H, 0.6	10.0	2160	0.57	0.15	3490	4.09	1.30	10.3	2780	0.48	0.00	4060	7.40	3850	0.74	0.28	4630
no H, 0.7	10.0	2070	0.58	0.11	3270	4.08	1.34	10.9	2600	0.50	0.03	3510	7.24	3560	0.79	0.32	4070
no H, 0.8	9.97	1930	0.56	0.12	3170	4.07	1.43	12.1	2810	0.52	0.00	3400	7.27	3330	0.77	0.34	3890
no H, 0.9	9.96	1900	0.56	0.09	3160	4.06	1.18	9.16	2000	0.48	0.01	3040	7.29	3090	0.75	0.38	3660
no H, 1.0	9.94	1730	0.57	0.15	2770	4.04	1.42	12.5	2390	0.53	0.00	2840	7.34	2980	0.76	0.32	3490
impl H, 0.1	10.1	3071	0.58	0.00	4836	4.12	1.37	10.3	4342	0.47	0.00	6446	7.40	5433	0.78	0.08	6288
impl H, 0.2	10.1	2888	0.59	0.00	4466	4.12	1.36	10.1	4452	0.45	0.00	7258	7.53	5507	0.75	0.00	6580
impl H, 0.3	10.1	2645	0.58	0.00	4202	4.12	1.39	10.3	3743	0.48	0.00	5452	6.99	4064	0.79	0.54	4659
impl H, 0.4	10.0	2469	0.56	0.00	4107	4.12	1.40	10.3	3391	0.50	0.00	4497	7.67	4444	0.71	0.00	5526
impl H, 0.5	10.0	2214	0.57	0.00	3577	4.12	1.37	10.4	3065	0.49	0.00	4329	7.64	3967	0.73	0.00	4812
impl H, 0.6	9.99	2132	0.56	0.00	3507	4.10	1.41	11.1	2749	0.51	0.00	3445	7.36	3414	0.75	0.30	4078
impl H, 0.7	9.96	1944	0.56	0.00	3202	4.11	1.41	11.3	2429	0.53	0.00	2934	7.14	2978	0.78	0.47	3437
impl H, 0.8	9.93	1790	0.56	0.00	2972	4.11	1.40	11.6	2191	0.53	0.00	2598	7.27	2779	0.77	0.37	3239
impl H, 0.9	9.90	1644	0.55	0.04	2774	4.09	1.41	11.7	2083	0.53	0.00	2489	7.38	2639	0.74	0.33	3172
impl H, 1.0	9.87	1250	0.57	0.20	2005	4.10	1.28	9.81	1377	0.53	0.03	1718	7.59	2196	0.74	0.21	2647

Table 4.12 Fit parameters for the cage relaxation function $\langle n(0)n(t)\rangle$ for all CHARMM simulations. $\langle CN\rangle$ is the average number of particles of particles in the first solvation shell and a_0 is the steady-state value this function is approaching in the asymptotic limit. τ and τ_{avg} are given in units of ps. τ_{avg} describes the mean residence time of a particle in the first solvation shell of another particle.

AMBER model	⊕⊕ ⟨CN⟩	τ	β	a_0	τ_{avg}	⊖⊖ ⟨CN⟩	a_1	τ_1	τ_2	β	a_0	τ_{avg}	⊕⊖ ⟨CN⟩	τ	β	a_0	τ_{avg}
nonpol	10.2	3140	0.57	0.14	5130	4.10	1.49	9.59	6190	0.49	a0	8200	7.28	5750	0.74	0.28	6920
no H, 0.1	10.1	3060	0.57	0.00	4890	4.08	1.45	10.1	4920	0.49	0.00	6710	7.30	5080	0.75	0.28	6060
no H, 0.2	10.1	2800	0.56	0.13	4680	4.08	1.46	10.2	4730	0.49	0.00	6260	7.16	5030	0.76	0.35	5910
no H, 0.3	10.1	2520	0.58	0.21	3990	4.06	1.48	10.6	4580	0.49	0.00	6030	7.23	4640	0.76	0.35	5460
no H, 0.4	10.1	2460	0.57	0.11	3930	4.05	1.46	11.0	3960	0.51	0.00	4890	7.33	4350	0.75	0.27	5150
no H, 0.5	10.0	2390	0.57	0.09	3880	4.04	1.33	11.6	3010	0.49	0.00	4200	7.43	4140	0.73	0.24	5030
no H, 0.6	10.0	2190	0.57	0.13	3560	4.02	1.45	12.2	3260	0.51	0.02	4020	7.45	3890	0.73	0.23	4720
no H, 0.7	9.99	2020	0.57	0.17	3260	4.00	1.32	13.8	2640	0.49	0.00	3660	7.33	3520	0.76	0.33	4160
no H, 0.8	9.95	1600	0.58	0.17	2530	4.00	1.24	11.2	1870	0.50	0.00	2580	7.48	2830	0.75	0.22	3360
no H, 0.9	9.92	1630	0.57	0.15	2640	3.98	1.26	10.0	1690	0.52	0.00	2150	7.34	2780	0.77	0.32	3230
no H, 1.0	9.90	1600	0.57	0.20	2610	3.96	1.09	8.31	1490	0.49	0.06	2270	7.54	2800	0.74	0.24	3380
impl H, 0.1	10.1	2900	0.56	0.04	4740	4.09	1.46	10.0	4770	0.48	0.04	6610	7.21	4890	0.76	0.33	5760
impl H, 0.2	10.1	2650	0.56	0.14	4370	4.09	1.46	9.99	4440	0.49	0.00	5840	7.11	4650	0.76	0.43	5460
impl H, 0.3	10.1	2660	0.55	0.02	4520	4.08	1.46	10.6	3850	0.50	0.00	4940	7.23	4360	0.76	0.34	5120
impl H, 0.4	10.1	2350	0.56	0.10	3930	4.07	1.44	10.7	3570	0.51	0.00	4400	7.30	4090	0.75	0.31	4880
impl H, 0.5	10.0	2240	0.57	0.11	3640	4.06	1.44	11.2	3260	0.52	0.00	3970	7.23	3850	0.78	0.32	4420
impl H, 0.6	9.98	1920	0.57	0.13	3110	4.06	1.34	10.7	2100	0.51	0.00	2710	7.38	3330	0.76	0.25	3900
impl H, 0.7	9.94	1680	0.56	0.12	2740	4.06	1.31	10.5	1820	0.51	0.06	2350	7.53	2910	0.73	0.21	3530
impl H, 0.8	9.90	1190	0.58	0.16	1890	4.05	1.20	8.88	1170	0.51	0.05	1610	7.60	2060	0.73	0.20	2500
impl H, 0.9	9.86	1150	0.56	0.19	1880	4.05	1.09	7.93	1080	0.49	0.04	1640	7.67	1970	0.71	0.21	2450
impl H, 1.0	9.81	1060	0.57	0.18	1700	4.04	0.93	3.00	850	0.48	0.03	1410	7.76	1790	0.71	0.17	2220
expl H, 0.1	10.1	2780	0.57	0.12	4490	4.10	1.47	10.0	4620	0.49	0.02	6280	7.18	4760	0.77	0.36	5560
expl H, 0.2	10.1	2720	0.56	0.01	4480	4.10	1.45	10.3	4070	0.51	0.00	5140	7.42	4640	0.74	0.19	5600
expl H, 0.3	10.0	2290	0.56	0.08	3740	4.11	1.46	10.5	3440	0.51	0.00	4260	7.32	3890	0.75	0.31	4630
expl H, 0.4	10.0	1960	0.57	0.16	3150	4.11	1.45	11.0	2860	0.52	0.00	3480	7.25	3460	0.78	0.33	4000
expl H, 0.5	9.97	1870	0.57	0.09	3020	4.11	1.29	10.7	2140	0.50	0.00	2990	7.45	3170	0.75	0.25	3790
expl H, 0.6	9.93	1620	0.57	0.16	2590	4.12	1.19	9.58	1820	0.49	0.02	2720	7.41	2820	0.76	0.29	3330
expl H, 0.7	9.88	1400	0.57	0.19	2260	4.12	1.14	9.07	1520	0.48	0.00	2360	7.51	2500	0.75	0.23	2980
expl H, 0.8	9.83	1150	0.57	0.14	1880	4.13	1.22	9.73	1180	0.52	0.01	1580	7.67	1970	0.72	0.20	2420
expl H, 0.9	9.79	1110	0.57	0.16	1800	4.13	1.09	8.01	1010	0.50	0.03	1490	7.71	1930	0.72	0.18	2380
expl H, 1.0	9.73	1040	0.56	0.16	1720	4.14	0.96	7.01	920	0.49	0.03	1490	7.80	1780	0.71	0.19	2240

Table 4.13 Fit parameters for the cage relaxation function $\langle n(0)n(t)\rangle$ for all AMBER simulations. $\langle CN\rangle$ is the average number of particles of particles in the first solvation shell and a_0 is the steady-state value this function is approaching in the asymptotic limit. τ and τ_{avg} are given in units of ps. τ_{avg} describes the mean residence time of a particle in the first solvation shell of another particle.

5 Conclusion

In this doctoral thesis I present six related studies on the broader topic of using molecular dynamics (MD) simulations to compute spectroscopic properties of soft matter systems. Two such systems, water-in-oil reverse micelles (RM) and ionic liquids (IL), are characterized in detail. The great detail available from simulation data is used to analyze and decompose the respective observables of each experimental method. A dielectric relaxation spectrum can be related to relaxation processes of the collective electric dipole moment of a sample, while the time-dependent Stokes shift (TDSS) seen in fluorescence spectroscopy can be seen to arise from a change in the solvation energy of the chromophor. In addition, different methods to model atomic polarizabilities are compared in their influence on structural and dynamical properties of IL in an effort to bring simulation results closer to experimental data. The following short discussion will give a brief overview of the most important findings.

5.1 Central findinds

RM are shown to exhibit a strong dielectric depolarization in order to blend in with the surrounding apolar medium isooctane. This depolarization is found not only in the average structure, but also in the relaxation dynamics of the collective electric dipole moment of RM. When decomposing the collective dipole moment into contributions by species, big individual effects of opposite sign are revealed, which lead to a small total average value. Decomposition of the time correlation function of the total dipole moment shows that each time domain of the relaxation process is characterized by a cancellation of specific molecular species, according to their dynamical capacity. This behaviour of the collective dipole moment translates into a dielectric relaxation spectrum with very small amplitudes. It is shown that this dielectric depolarization is found for RM with different water loading and even upon inclusion of the strongly polar protein ubiquitin. Taking these results together, individual RM appear as particles with highly coupled electrostatics and strongly correlated internal dynamics.

In principle, a structure such as a RM has two pathways of dipolar relaxation: by overall micellar tumbling motion or by internal reorganization. Typically, internal reorganization is much faster than the tumbling motion of the whole RM. It is shown that for RM with low water loading, internal dynamics slow down considerably, while, at the same time, tumbling motion is faster due to the smaller total size of the particle. In fact, if both relaxation pathways occur within similar time scales, then micellar tumbling motion has a significant impact on the observed dielectric spectrum, which no longer characterizes internal dynamics of the RM alone. A remedy to disentangle the two pathways is developed on the basis that RM tumbling motion is governed by hydrodynamics and obeys the Debye-Stokes equation.

This allows for a calculation of the average tumbling time, if one knows the average micellar volume and the viscosity of the outside medium. Using the resulting tumbling time and assuming that micellar rotation and internal reorganization are independent processes, it is shown that the dielectric relaxation spectrum can be corrected for the effects of tumbling motion. This approach should be applicable to experimental data in much the same way.

The TDSS and dielectric relaxation spectroscopy can both be seen as measuring the capacity of a solvent to react to a change in an applied electric field, with the difference being that in the case of DRS the electric field is applied externally, while in the TDSS the change of the electric field is caused by electronic excitation of solute molecules embedded in the solvent. In this way, the solute molecules can be seen as local probes of their environment. A reaction field continuum model to predict the TDSS from the frequency-dependent dielectric permittivity well-established for polar solvents is generalized to study the special role of conductivity in IL, where the model theory was shown to predict too fast relaxation times for the TDSS. In IL a collective electric dipole moment is not only formed through the orientational structuring of the molecules. Rather, as each particle carries a charge, their relative positions also create an electric dipole moment, which relaxes by means of diffusion of particles. In fact, this dielectric conductivity[98] alone is shown to be sufficient to predict the characteristic two time regimes in the TDSS, while the relaxation process is still too fast in comparison to experiment. One would expect that including rotational contributions, which are located at lower frequencies in the dielectric spectrum, makes up for that deficiency by adding slower processes to the TDSS. However, it is shown that the TDSS predicted from the complete dielectric relaxation spectrum is quite the same as the one obtained from the dielectric conductivity alone. The reason is that in a conducting system the dielectric relaxation spectrum at lower frequencies is completely dominated by static conductivity (cf. Fig. 3.5). In this way, the reaction field continuum model is shown to severely underestimate low-frequency contributions to the TDSS in conductive systems such as IL.

Non-equilibrium simulations of the TDSS in IL are shown to be a powerful tool allowing for a detailed analysis of the relaxation process. The solvation energy governing the time-dependence of the TDSS is given by additive Coulomb interactions. Exploiting this additive nature, the TDSS can in principle be decomposed down to the atomic level. It is shown that with a high number of independent non-equilibrium simulations of the TDSS, the necessary statistical accuracy can be achieved. Using the chromophor coumarin 153 (C153) in a coarse-grained representation of the IL 1-ethyl-3-methylimidazolium triflate as a model system, various ways to investigate the origin of the observed TDSS are explored. When decomposing contributions of the solvent, it is confirmed that anions have a much larger part in the observed energy shift than cations. Additionally, the TDSS is revealed to be largely caused by molecules in the first solvation shell around the chromophor. When decomposing the TDSS in terms of individual atoms of the solute, it is shown that only 9 out of 36 atoms of C153 contribute to the total signal significantly, yielding 90% of the total Stokes shift. Taking these observations together, the TDSS appears to be a rather localized effect, mostly measuring changes of the solvent in close vicinity to specific parts of the solute. This raises

the question to what extent the TDSS is actually measuring bulk solvent properties, which likely are already disturbed to some degree by the presence of the solute alone.

The addition of atomic polarizabilities to classical MD simulations of IL is shown to have a profound impact on the observed structural and dynamical properties. Intermolecular electrostatic interactions are damped significantly, leading to accelerated dynamics and less pronounced structural features. In a sense, this behaviour is reminiscent of adding a co-solvent, suggesting that atomic polarizabilities can be seen as an "inner" solvent. In a direct comparison of two widely used methods to implement atomic polarizabilities, namely Drude oscillators and induced point-dipoles, rather similar effects are found in both cases. Structural as well as dynamical properties are shown to depend on the total polarizability of both ionic species in the system, which thus can be used as a common scale to compare different polarizability models. The influence on all properties shows the same qualitative trend in both models, though it is more pronounced when using the induced point-dipole model. Due to technical limitations, hydrogen atoms cannot be made polarizable when using the Drude oscillator model in combination with the computationally efficient Lagrangian formalism. A remedy for this is to add the atomic polarizability of each hydrogen atom to the respective heavy atom to which it is connected, instead of simply omitting hydrogen polarizabilities. In this way, the two polarizability models are shown to yield consistent results, that differ only slightly in the size of the observed effect.

The choice of Thole function to dampen short-range interactions of induced point-dipoles is shown to have only little influence on structural and dynamical properties of IL. This shows that using a Thole function to avoid the "polarization catastrophe" in polarizable simulations will not affect the obtained results in a significant way.

5.2 Final remarks

The common ground of all six publications presented in this thesis is that computer simulation can be valuable tool in helping to interpret experimental spectroscopic results. Specifically, newly developed methods are shown to provide a deeper understanding the molecular origins of experimentally observed signals. It is shown that MD simulations can reproduce experimental spectra with good success. Furthermore, the respective experimental observable can be decomposed, yielding insightful results, which aid in obtaining a more complete picture of what is actually measured in experiment.

In addition to comprehensive computational studies of spectroscopic properties, this thesis includes investigations into how to bring simulation results closer to experiment by using a model of atomic polarizabilities. As various such models have been implemented, a comparative study of two such models was done confirming that they give qualitatively consistent results. This result thus proves that both models can be used largely interchangebly and that results obtained using different models can be compared.

Bibliography

[1] N. V. Plechkova and K. R. Seddon, *Chem. Soc. Rev.*, 2008, **37**, 123.

[2] M. Armand, F. Endres, D. R. MacFarlane, H. Ohno and B. Scrosati, *Nature Materials*, 2009, **8**, 621.

[3] T. Welton, *Chem. Rev.*, 1999, **99**, 2071.

[4] A. Pinkert, K. N. Marsh, S. Pang and M. P. Staiger, *Chem. Rev.*, 2009, **109**, 6712.

[5] H.-X. Zhou, *Arch. Biochem. Biophys.*, 2008, **469**, 76.

[6] I. Dodevski, N. V. Nucci, K. G. Valentine, G. K. Sidhu, E. S. O'Brien, A. Pardi and A. J. Wand, *J. Am. Chem. Soc.*, 2014, **136**, 3465.

[7] D. Braun, M. Schmollngruber and O. Steinhauser, *Phys. Chem. Chem. Phys.*, 2016, **18**, 24620.

[8] D. S. Venables, K. Huang and C. A. Schmuttenmaer, *J. Phys. Chem. B*, 2001, **105**, 9132.

[9] D. E. Rosenfeld and C. A. Schmuttenmaer, *J. Phys. Chem. B*, 2006, **110**, 14304.

[10] M. D'Angelo, D. Fioretto, G. Onori, L. Palmieri and A. Santucci, *Phys. Rev. E*, 1995, **52**, 4620.

[11] M. D'Angelo, D. Fioretto, G. Onori and A. Santucci, *J. Mol. Struct.*, 1996, **383**, 157.

[12] M. D'Angelo, D. Fioretto, G. Onori, L. Palmieri and A. Santucci, *Phys. Rev. E*, 1996, **54**, 993.

[13] M. Freda, G. Onori, A. Paciaroni and A. Santucci, *J. Mol. Liquids*, 2002, **101**, 55.

[14] S. Balakrishnan, *Structure and dynamics of fluids in confinement: A case study of water, protein and ionic liquid in reverse micelles and microemulsions*, Ruhr-University Bochum, 2007.

[15] A. Patra, T. Q. Luong, R. K. Mitra and M. Havenith, *Phys. Chem. Chem. Phys.*, 2014, **16**, 12875.

[16] M. P. Allen and D. J. Tildesley, *Computer simulations of liquids*, Oxford Press, New York, 1989.

[17] S. Gabl, C. Schröder and O. Steinhauser, *J. Chem. Phys.*, 2012, **137**, 094501.

[18] B. R. Brooks, C. L. Brooks III, A. D. MacKerell Jr., L. Nilsson, R. J. Petrella, B. Roux, Y. Won, G. Archontis, C. Bartels, S. Boresch, A. Caflisch, L. Caves, Q. Cui, A. R. Dinner, M. Feig, S. Fischer, J. Gao, M. Hodoscek, W. Im, K. Kuczera, T. Lazaridis, J. Ma, V. Ovchinnikov, E. Paci, R. W. Pastor, C. B. Post, J. Z. Pu, M. Schaefer, B. Tidor, R. M. Venable, H. L. Woodcock, X. Wu, W. Yang, D. M. York and M. Karplus, *J. Comput. Chem.*, 2009, **30**, 1545.

[19] C. Schröder, T. Sonnleitner, R. Buchner and O. Steinhauser, *Phys. Chem. Chem. Phys.*, 2011, **13**, 12240.

[20] G. Lamoureux and B. Roux, *J. Chem. Phys.*, 2003, **119**, 3025.

[21] H. Yu, T. Hansson and W. F. van Gunsteren, *J. Chem. Phys.*, 2003, **118**, 221.

[22] E. Harder, V. M. Anisimov, I. V. Vorobyov, P. E. M. Lopes, S. Y. Noskov, A. D. MacKerell Jr. and B. Roux, *J. Chem. Theory Comput.*, 2006, **2**, 1587.

[23] D. P. Geerke and W. F. van Gunsteren, *J. Chem. Theory Comput.*, 2007, **3**, 2128.

[24] C. Schröder and O. Steinhauser, *J. Chem. Phys.*, 2010, **133**, 154511.

[25] C. Schröder, *Phys. Chem. Chem. Phys.*, 2012, **14**, 3089.

[26] P. E. M. Lopes, B. Roux and A. D. MacKerell Jr., *Theor. Chem. Acc.*, 2009, **124**, 11.

[27] T. Yan, C. J. Burnham, M. G. Del Pópolo and G. A. Voth, *J. Phys. Chem. B*, 2004, **108**, 11877.

[28] W. Jiang, T. Yan, Y. Wang and G. A. Voth, *J. Phys. Chem. B*, 2008, **112**, 3121.

[29] T. Yan, Y. Wang and C. Knox, *J. Phys. Chem. B*, 2010, **114**, 6886.

[30] T. Yan, Y. Wang and C. Knox, *J. Phys. Chem. B*, 2010, **114**, 6905.

[31] T.-M. Chang and L. X. Dang, *J. Phys. Chem. A*, 2009, **113**, 2127.

[32] O. Borodin, *J. Phys. Chem. B*, 2009, **113**, 11463.

[33] O. Borodin, W. Gorecki, G. Smith and M. Armand, *J. Phys. Chem. B*, 2010, **114**, 6786.

[34] J. B. Hooper, O. N. Starovoytov, O. Borodin, D. Bedrov and G. D. Smith, *J. Chem. Phys.*, 2012, **136**, 194506.

[35] S. W. Rick, S. J. Stuart and B. J. Berne, *J. Chem. Phys.*, 1994, **101**, 6141.

[36] S. Patel and C. L. Brooks III, *J. Comput. Chem.*, 2004, **25**, 1.

[37] A. K. Rappe and W. A. Goddard III, *J. Phys. Chem.*, 1991, **95**, 3358.

[38] M. C. C. Ribeiro, *Phys. Rev. B*, 2001, **63**, 094205.

[39] A. de Oliveira Cavalcante, M. Ribeiro and M. Skaf, *J. Chem. Phys.*, 2014, **140**, 144108.

[40] H. A. Stern, F. Rittner, B. J. Berne and R. A. Friesner, *The Journal of Chemical Physics*, 2001, **115**, 2237–2251.

[41] S. W. Rick, *The Journal of Chemical Physics*, 2001, **114**, 2276–2283.

[42] S. Zhu, S. Singh and G. W. Robinson, *The Journal of Chemical Physics*, 1991, **95**, 2791–2799.

[43] B. T. Thole, *Chem. Phys.*, 1981, **59**, 341.

[44] C. Schröder and O. Steinhauser, *J. Chem. Phys.*, 2009, **131**, 114504.

[45] M. Maroncelli, X.-X. Zhang, M. Liang, D. Roy and N. P. Ernsting, *Faraday Discuss.*, 2012, **154**, 409.

[46] T. Keyes and D. Kivelson, *J. Chem. Phys.*, 1972, **56**, 1057.

[47] D. Kivelson and P. Madden, *Mol. Phys.*, 1975, **30**, 1749.

[48] D. Braun, S. Boresch and O. Steinhauser, *J. Chem. Phys.*, 2014, **140**, 064107.

[49] W. D. Van Horn, M. E. Ogilvie and P. F. Flynn, *J. Am. Chem. Soc.*, 2009, **131**, 8030.

[50] S. Mukherjee, P. Chowdhury and F. Gai, *J. Phys. Chem. B*, 2006, **110**, 11615.

[51] H. Workman and P. F. Flynn, *J. Am. Chem. Soc.*, 2009, **131**, 3806.

[52] J. Tian and A. E. García, *J. Chem. Phys.*, 2011, **134**, 225101.

[53] S. Abel, M. Waks, W. Urbach and M. Marchi, *J. Am. Chem. Soc.*, 2006, **128**, 383.

[54] A. V. Martinez, S. C. DeSensi, L. Dominguez, E. Rivera and J. E. Straub, *J. Chem. Phys.*, 2011, **134**, 055107.

[55] J. Tian and A. E. García, *Biophys. J.*, 2009, **96**, L57.

[56] S. Abel, M. Waks and M. Marchi, *Eur. Phys. J. E*, 2010, **32**, 399.

[57] J. M. Kielec, K. G. Valentine and A. J. Wand, *Biochim. Biophys. Acta*, 2010, **1798**, 150.

[58] N. V. Nucci, M. S. Pometun and A. J. Wand, *Nature*, 2011, **18**, 245.

[59] A. J. Wand, M. R. Ehrhardt and P. F. Flynn, *Proc. Natl. Acad. Sci.*, 1998, **95**, 15299.

[60] C. R. Babu, P. F. Flynn and A. J. Wand, *J. Am. Chem. Soc.*, 2001, **123**, 2691.

[61] N. V. Nucci, K. G. Valentine and A. J. Wand, *J. Magn. Reson.*, 2014, **241**, 137.

[62] J. Faeder and B. M. Ladanyi, *J. Phys. Chem. B*, 2000, **104**, 1035.

[63] A. V. Martinez, L. Dominguez, E. Malolepsza, A. Moser, Z. Ziegler and J. E. Straub, *J. Phys. Chem. B*, 2013, **117**, 7345.

[64] J. Chowdhary and B. M. Ladanyi, *J. Phys. Chem. B*, 2009, **113**, 15029.

[65] E. N. Brodskaya and G. V. Mudzhikova, *Mol. Phys.*, 2006, **104**, 3635.

[66] S. Abel, F. Sterpone, S. Bandyopadhyay and M. Marchi, *J. Phys. Chem. B*, 2004, **108**, 19458.

[67] J. Faeder and B. M. Ladanyi, *J. Phys. Chem. B*, 2001, **105**, 11148.

[68] M. Marchi and S. Abel, *J. Phys. Chem. Lett.*, 2015, **6**, 170.

[69] V. R. Vasquez, B. C. Williams and O. A. Graeve, *J. Phys. Chem. B*, 2011, **115**, 2979.

[70] E. Negro, R. Latsuzbaia, A. H. de Vries and G. J. M. Koper, *Phys. Chem. Chem. Phys.*, 2014, **10**, 8685.

[71] M. H. H. Pomata, D. Laria, M. S. Skaf and M. D. Elola, *J. Chem. Phys.*, 2008, **129**, 244503.

[72] G. Carlström and B. Halle, *Langmuir*, 1988, **4**, 1346.

[73] M. Freda, G. Onori, A. Paciaroni and A. Santucci, *Phys. Rev. E*, 2003, **68**, 021406.

[74] D. Cringus, A. Bakulin, J. Lindner, P. Vöhringer, M. S. Pshenichnikov and D. A. Wiersma, *J. Phys. Chem. B*, 2007, **111**, 14193.

[75] I. R. Piletic, D. E. Moilanen, D. B. Spry, N. E. Levinger and M. D. Fayer, *J. Phys. Chem. A*, 2006, **110**, 4985.

[76] D. E. Moilanen, E. E. Fenn, D. Wong and M. D. Fayer, *J. Chem. Phys.*, 2009, **131**, 014704.

[77] T. Kinugasa, A. Kondo, S. Nishimura, Y. Miyauchi, Y. Nishii, K. Watanabe and H. Takeuchi, *Colloids and Surfaces A: Physicochem. Eng. Aspects*, 2002, **204**, 193.

[78] A.-P. Hynninen and M. F. Crowley, *J. Comput. Chem.*, 2014, **35**, 406.

[79] L. Martínez, R. Andrade, G. Birgin and J. M. Martínez, *J. Comput. Chem.*, 2009, **30**, 2157.

[80] T. Darden, D. York and L. Pedersen, *J. Chem. Phys.*, 1993, **98**, 10089.

[81] U. Essmann, L. Perera, M. L. Berkowitz, T. Darden, H. Lee and L. G. Pedersen, *J. Chem. Phys.*, 1995, **103**, 8577.

[82] J.-P. Ryckaert, G. Ciccotti and H. J. C. Berendsen, *J. Comput. Phys.*, 1977, **23**, 327.

[83] H. J. C. Berendsen, J. R. Grigera and T. P. Straatsma, *J. Phys. Chem.*, 1987, **91**, 6269.

[84] L. D. Schuler, X. Daura and W. F. van Gunsteren, *J. Comput. Chem.*, 2001, **22**, 1205.

[85] A. D. MacKerell Jr., D. Bashford, M. Bellott, R. L. Dunbrack, J. D. Evanseck, M. J. Field, S. Fischer, J. Gao, H. Guo, S. Ha, D. Joseph-McCarthy, L. Kuchnir, K. Kuczera, F. T. K. Lau, C. Mattos, S. Michnick, T. Ngo, D. T. Nguyen, B. Prodhom, W. E. Reiher, B. Roux, M. Schlenkrich, J. C. Smith, R. Stote, J. Straub, M. Watanabe, J. Wiorkiewicz-Kuczera, D. Yin and M. Karplus, *J. Phys. Chem. B*, 1998, **102**, 3586.

[86] A. D. MacKerell, Jr., M. Feig and C. L. Brooks, III, *J. Am. Chem. Soc.*, 2004, **126**, 698.

[87] R. B. Best, X. Zhu, J. Shim, P. E. M. Lopes, J. Mittal, M. Feig and A. D. MacKerell, Jr., *J. Chem. Theory Comput.*, 2012, **8**, 3257.

[88] D. Beglov and B. Roux, *J. Chem. Phys.*, 1994, **100**, 9050.

[89] S. Vijay-Kumar, C. E. Bugg and W. J. Cook, *J. Mol. Biol.*, 1987, **194**, 531.

[90] H. M. Berman, J. Westbrook, Z. Feng, G. Gilliland, T. N. Bhat, H. Weissig, I. N. Shindyalov and P. E. Bourne, *Nucl. Acids Res.*, 2000, **28**, 235.

[91] M. Sega and C. Schröder, *J. Phys. Chem. A*, 2015, **119**, 1539.

[92] N. Michaud-Agrawal, E. J. Denning, T. B. Woolf and O. Beckstein, *J. Comput. Chem.*, 2011, **32**, 2319.

[93] C. H. Rycroft, *Voro++: a three-dimensional Voronoi cell library in C++*, Lawrence Berkeley National Laboratory, 2009.

[94] D. Brown and J. H. R. Clarke, *J. Phys. Chem.*, 1988, **92**, 2881.

[95] C. Schröder, T. Rudas, G. Neumayr, S. Benkner and O. Steinhauser, *J. Chem. Phys.*, 2007, **127**, 234503.

[96] G. Neumayr, C. Schröder and O. Steinhauser, *J. Chem. Phys.*, 2009, **131**, 174509.

[97] M. Neumann and O. Steinhauser, *Chem. Phys. Lett.*, 1983, **95**, 417.

[98] C. Schröder and O. Steinhauser, *J. Chem. Phys.*, 2010, **132**, 244109.

[99] B. González, A. Domínguez and J. Tojo, *J. Chem. Eng. Data*, 2006, **51**, 1076.

[100] A. Pádua, J. Fareleira, C. Calado and W. Wakeham, *J. Chem. Eng. Data*, 1996, **41**, 1488.

[101] M. Schmollngruber, C. Schröder and O. Steinhauser, *Phys. Chem. Chem. Phys.*, 2014, **16**, 10999.

[102] B. Guillot, *J. Chem. Phys.*, 1991, **95**, 1543.

[103] J.-B. Brubach, A. Mermer, A. Filabozzi, A. Gerschel and P. Roy, *J. Chem. Phys.*, 2005, **122**, 184509.

[104] T. Rudas, C. Schröder, S. Boresch and O. Steinhauser, *J. Chem. Phys.*, 2006, **124**, 234908.

[105] A. Savitzky and M. J. E. Golay, *Anal. Chem.*, 1964, **36**, 1627–1639.

[106] T. Fukasawa, T. Sato, J. Watanabe, Y. Hama, W. Kunz and R. Buchner, *Phys. Rev. Lett.*, 2005, **95**, 197802.

[107] H. Yada, M. Nagai and K. Tanaka, *Chem. Phys. Lett.*, 2008, **464**, 166.

[108] F. Wooten, *Optical Properties of Solids*, Academic Press, New York and London, 1972.

[109] H. Fröhlich, *Theory of Dielectrics*, Oxford Clarendon Press, 1990.

[110] C. J. F. Böttcher, *Theory of electric polarization*, Elsevier, Amsterdam, 1952.

[111] M. Schmollngruber, D. Braun, D. Oser and O. Steinhauser, *Phys. Chem. Chem. Phys.*, 2016, **18**, 3606.

[112] P. A. Pieniazek, Y. S. Lin, J. Chowdhary, B. M. Ladanyi and J. L. Skinner, *J. Phys. Chem. B*, 2009, **113**, 15017.

[113] M. D. Fayer and N. E. Levinger, *Annu. Rev. Anal. Chem.*, 2010, **3**, 89.

[114] N. E. Levinger and L. A. Swafford, *Annu. Rev. Phys. Chem.*, 2009, **60**, 385.

[115] H. Eicke and J. Rehak, *Helv. Chim. Acta*, 1976, **59**, 2883.

[116] C. J. F. Böttcher and P. Bordewijk, *Theory of electric polarization*, Elsevier, Amsterdam, 1978, vol. 2.

[117] B. K. P. Horn, *J. Opt. Soc. Am. A*, 1987, **4**, 629.

[118] C. Schröder, C. Wakai, H. Weingärtner and O. Steinhauser, *J. Chem. Phys.*, 2007, **126**, 084511.

[119] C. Schröder, J. Hunger, A. Stoppa, R. Buchner and O. Steinhauser, *J. Chem. Phys.*, 2008, **129**, 184501.

[120] M. L. Horng, J. A. Gardecki, A. Papazan and M. Maroncelli, *J. Phys. Chem.*, 1995, **99**, 17311.

[121] X. Song, *J. Chem. Phys.*, 2009, **131**, 044503.

[122] X.-X. Zhang, M. Liang, N. P. Ernsting and M. Maroncelli, *J. Phys. Chem. B*, 2013, **117**, 4291.

[123] X.-X. Zhang, M. Liang, J. Hunger, R. Buchner and M. Maroncelli, *J. Phys. Chem. B*, 2013, **117**, 15356.

[124] M. Liang, X.-X. Zhang, A. Kaintz, N. P. Ernsting and M. Maroncelli, *J. Phys. Chem. B*, 2014, **118**, 1340.

[125] M. Schmollngruber, C. Schröder and O. Steinhauser, *J. Chem. Phys.*, 2013, **138**, 204504.

[126] B. M. Ladanyi and M. Maroncelli, *J. Chem. Phys.*, 1998, **109**, 3204.

[127] B. M. Ladanyi and R. M. Stratt, *J. Phys. Chem.*, 1995, **99**, 2502–2511.

[128] R. M. Stratt and M. Cho, *J. Chem. Phys.*, 1994, **100**, 6700.

[129] B. M. Ladanyi and R. M. Stratt, *J. Phys. Chem.*, 1996, **100**, 1266.

[130] M. Maroncelli and G. R. Fleming, *J. Chem. Phys.*, 1988, **89**, 5044.

[131] L. R. Martins, A. Tamashiro, D. Laria and M. S. Skaf, *J. Chem. Phys.*, 2003, **118**, 5955.

[132] P. V. Kumar and M. Maroncelli, *J. Chem. Phys.*, 1995, **103**, 3038.

[133] N. Ito, S. Arzhantsev and M. Maroncelli, *Chem. Phys. Lett.*, 2004, **396**, 83.

[134] P. K. Chowdhury, M. Halder, L. Sanders, T. Calhoun, J. L. Anderson, D. W. Armstrong, X. Song and J. W. Petrich, *J. Phys. Chem. B*, 2004, **108**, 10245.

[135] L. S. Headley, P. Mukherjee, J. L. Anderson, R. Ding, M. Halder, D. W. Armstrong, X. Song and J. W. Petrich, *J. Phys. Chem. A*, 2006, **110**, 9549.

[136] B. L. Bhargava and S. Balasubramanian, *J. Chem. Phys.*, 2005, **123**, 144505.

[137] M. N. Kobrak, *J. Chem. Phys.*, 2006, **125**, 064502.

[138] Y. Shim, M. Y. Choi and H. J. Kim, *J. Chem. Phys.*, 2005, **122**, 044511.

[139] Y. Shim, J. Duan, M. Y. Choi and H. J. Kim, *J. Chem. Phys.*, 2003, **119**, 6411.

[140] D. Jeong, Y. Shim, M. Y. Choi and H. J. Kim, *J. Phys. Chem. B*, 2007, **111**, 4920.

[141] M. N. Kobrak and V. Znamenskiy, *Chem. Phys. Lett.*, 2004, **395**, 127.

[142] H. K. Kashyap and R. Biswas, *J. Phys. Chem. B*, 2010, **114**, 254.

[143] S. Daschakraborty and R. Biswas, *J. Chem. Phys.*, 2012, **137**, 114501.

[144] S. Daschakraborty and R. Biswas, *J. Phys. Chem. B*, 2011, **115**, 4011.

[145] S. Daschakraborty and R. Biswas, *J. Chem. Phys.*, 2013, **139**, 164503.

[146] X.-X. Zhang, C. Schröder and N. P. Ernsting, *J. Chem. Phys.*, 2013, **138**, 111102.

[147] Y. Shim and H. J. Kim, *J. Phys. Chem. B*, 2013, **117**, 11743.

[148] Z. L. Terranova and S. A. Corcelli, *J. Phys. Chem. B*, 2013, **117**, 15659.

[149] S. Arzhantsev, H. Jin, G. A. Baker and M. Maroncelli, *J. Phys. Chem. B*, 2007, **111**, 4978.

[150] M. Maroncelli and G. R. Fleming, *J. Chem. Phys.*, 1987, **86**, 6221.

[151] Y. Mazurenko, *Opt. Spectrosc. (USSR)*, 1974, **36**, 283.

[152] C.-P. Hsu, X. Song and R. A. Marcus, *J. Phys. Chem. B*, 1997, **101**, 2546–2551.

[153] I. Rips, J. Klafter and J. Jortner, *J. Chem. Phys*, 1988, **88**, 3246.

[154] T. G. Scholte, *Physica*, 1949, **15**, 437.

[155] C. J. F. Böttcher and P. Bordewijk, *Theory of electric polarization*, Elsevier, Amsterdam, 1978, vol. 1.

[156] E. Castner, G. Fleming and B. Bagchi, *Chem. Phys. Lett.*, 1988, **143**, 270.

[157] C. Schröder, *J. Chem. Phys.*, 2011, **135**, 024502.

[158] K. Bica, C. Schröder, M. Deetlefs and K. R. Seddon, *Phys. Chem. Chem. Phys.*, 2013, **15**, 2703.

[159] L. Hongping, S. Arzhantsev and M. Maroncelli, *J. Phys. Chem. B*, 2007, **111**, 3208.

[160] D. Roy and M. Maroncelli, *J. Phys. Chem. B*, 2012, **116**, 5951.

[161] D. Braun and O. Steinhauser, *Phys. Chem. Chem. Phys.*, 2015, **17**, 8509.

[162] S. Nosé, *Mol. Phys.*, 1984, **52**, 255.

[163] S. Nosé, *J. Chem. Phys.*, 1984, **81**, 511.

[164] W. G. Hoover, *Phys. Rev.*, 1985, **A31**, 1695.

[165] D. Wolf, P. Keblinski, S. R. Phillpot and J. Eggebrecht, *J. Chem. Phys.*, 1999, **110**, 8254.

[166] P. A. Hunt, *Mol. Sim.*, 2006, **32**, 1.

[167] E. J. Maginn, *Condens. Matter*, 2009, **21**, 373101.

[168] A. Triolo, O. Russina, H.-J. Bleif and E. Di Cola, *J. Phys. Chem. B*, 2007, **111**, 4641.

[169] O. Russina, A. Triolo, L. Gontrani, R. Caminiti, D. Xiao, L. G. Hines Jr., R. A. Bartsch, E. L. Quitevis, N. Plechkova and K. R. Seddon, *J. Phys. Condens. Matter*, 2009, **21**, 424121.

[170] J. N. A. Canongia Lopes and A. A. H. Pádua, *J. Phys. Chem. B*, 2006, **110**, 3330.

[171] A. A. H. Pádua, M. F. Costa Gomes and J. N. A. Conongia Lopes, *Acc. Chem. Res.*, 2007, **40**, 1087.

[172] Y. Wang, W. Jiang, T. Yan and G. A. Voth, *Acc. Chem. Res.*, 2007, **40**, 1193.

[173] S. M. Urahata and M. C. C. Ribeiro, *J. Chem. Phys.*, 2004, **120**, 1855.

[174] J. N. Canongia Lopes, J. Deschamps and A. A. H. Pádua, *J. Phys. Chem. B*, 2004, **108**, 2038.

[175] J. N. Canongia Lopes and A. A. H. Pádua, *J. Phys. Chem. B*, 2004, **108**, 16893.

[176] A. Bagno, F. D'Amico and G. Saielli, *J. Mol. Liquids*, 2007, **131-132**, 17.

[177] L. J. A. Siqueira and M. C. C. Ribeiro, *J. Phys. Chem. B*, 2007, **111**, 11776.

[178] J. Pićalek and J. Kolafa, *J. Mol. Liquids*, 2007, **134**, 29.

[179] E. J. Maginn, *Acc. Chem. Res.*, 2007, **40**, 1200.

[180] F. Dommert, J. Schmidt, C. Krekeler, Y. Y. Zhao, R. Berger, L. delle Site and C. Holm, *J. Mol. Liquids*, 2010, **152**, 2.

[181] V. V. Chaban, I. V. Voroshylova and O. N. Kalugin, *Phys. Chem. Chem. Phys.*, 2011, **13**, 7910.

[182] B. L. Bhargava and S. Balasubramanian, *J. Chem. Phys.*, 2007, **127**, 114510.

[183] W. Zhao, H. Eslami, W. L. Cavalcanti and F. Müller-Plathe, *J. Phys. Chem.*, 2007, **221**, 1647.

[184] J. Schmidt, C. Krekeler, F. Dommert, Y. Zhao, R. Berger, L. delle Site and C. Holm, *J. Phys. Chem. B*, 2010, **114**, 6150.

[185] D. Roy and M. Maroncelli, *J. Phys. Chem. B*, 2010, **114**, 12629.

[186] D. T. Bowron, C. D'Agostino, L. F. Gladden, C. Hardacre, J. D. Holbrey, M. C. Lagunas, J.McGregor, M. D. Mantle, C. L. Mullan and T. G. A. Youngs, *J. Phys. Chem. B*, 2010, **114**, 7760.

[187] M. Kohagen, M. Brehm, J. Thar, W. Zhao, F. Müller-Plathe and B. Kirchner, *J. Phys. Chem. B*, 2011, **115**, 693.

[188] H. Liu and E. Maginn, *J. Chem. Phys.*, 2011, **135**, 124507.

[189] *CHARMM: Chemistry at HARvard Macromolecular Mechanics*, `http://www.charmm.org/`.

[190] I. T. Todorov, W. Smith, K. Trachenko and M. T. Dove, *J. Mater. Chem.*, 2006, **16**, 1911.

[191] D. Bedrov, O. Borodin, Z. Li and G. D. Smith, *J. Phys. Chem. B*, 2010, **114**, 4984.

[192] `http://www.eng.utah.edu/~gdsmith/lucretius.html`.

[193] *AMBER: Assisted Model Building with Energy Refinement*, `http://www.ambermd.org/`.

[194] M. G. Del Pópolo, R. M. Lynden-Bell and J. Kohanoff, *J. Phys. Chem. B*, 2005, **109**, 5895.

[195] C. Spickermann, J. Thar, S. B. C. Lehmann, S. Zahn, J. Hunger, R. Buchner, P. A. Hunt, T. Welton and B. Kirchner, *J. Chem. Phys.*, 2008, **129**, 104505.

[196] S. Zahn, J.Thar and B. Kirchner, *J. Chem. Phys.*, 2010, **132**, 124506.

[197] M. Brüssel, M. Brehm, T. Voigt and B. Kirchner, *Phys. Chem. Chem. Phys.*, 2011, **13**, 13617.

[198] H. Yu and W. F. van Gunsteren, *Comput. Phys. Commun.*, 2005, **172**, 69.

[199] D. van der Spoel, E. Lindahl, B. Hess, G. Groenhof, A. E. Mark and H. J. C. Berendsen, *J. Comput. Chem.*, 2005, **26**, 1701.

[200] P. T. van Duijnen and M. Swart, *J. Phys. Chem. A*, 1998, **102**, 2399.

[201] J. Applequist, J. R. Carl and K.-K. Fung, *J. Am. Chem. Soc.*, 1972, **94**, 2952.

[202] Y. Gu and T. Yan, *J. Phys. Chem. A*, 2013, **117**, 219.

[203] J. Applequist, *Acc. Chem. Res.*, 1977, **10**, 79.

[204] H. Rodriguez and J. F. Brennecke, *J. Chem. Eng. Data*, 2006, **51**, 2145.

[205] H. De Loof, L. Nilsson and R. Rigler, *J. Am. Chem. Soc.*, 1992, **114**, 4028.

[206] P. A. Madden and M. Wilson, *Chem. Soc. Rev.*, 1996, **25**, 339.

[207] C. Schröder, T. Rudas and O. Steinhauser, *J. Chem. Phys.*, 2006, **125**, 244506.

[208] J. M. Crosthwaite, M. J. Muldoon, S. N. V. K. Aki, E. J. Maginn and J. F. Brennecke, *J. Phys. Chem. B*, 2006, **110**, 9354.

[209] W. L. Jorgensen, D. S. Maxwell and J. Tirado-Rives, *J. Am. Chem. Soc.*, 1996, **118**, 11225.

[210] C. Schröder, G. Neumayr and O. Steinhauser, *J. Chem. Phys.*, 2009, **130**, 194503.

[211] N. Ignat'ev, U. Welz-Biermann, A. Kucheryna, G. Bissky and H. Willner, *J. Fluorine Chem.*, 2005, **126**, 1150.

[212] L. Verlet, *Phys. Rev.*, 1967, **159**, 98.

[213] U. Singh and P. Kollman, *J. Comput. Chem.*, 1984, **5**, 129.

[214] H. Kornfeld, *Zeitschrift für Physik*, 1924, **22**, 27–43.

[215] D. Adams and G. Dubey, *Journal of Computational Physics*, 1987, **72**, 156–176.

[216] D. A. Case, T. A. Darden, T. E. Cheatham, III, C. Simmerling, J. Wang, R. E. Duke, R. Luo, R. C. Walker, W. Zhang, K. Merz, B. Roberts, B. Wang, S. Hayik, A. Roitberg, G. Seabra, I. Kolossvary, K. Wong, F. Paesani, J. Vanicek, X. Wu, S. Brozell, T. Steinbrecher, H. Gohlke, Q. Cai, X. Ye, J. Wang, M.-J. Hsieh, G. Cui, D. Roe, D. Mathews,

M. Seetin, C. Sagui, V. Babin, T. Luchko, S. Gusarov, A. Kovalenko and P. Kollman, *Amber 11*, San Francisco, 2010.

[217] H. Berendsen, J. Postma, W. van Gunsteren, A. DiNola and J. Haak, *J. Chem. Phys.*, 1984, **81**, 3684.

[218] C. Rycroft, G. Grest, J. Landry and M. Bazant, *Phys. Rev. E*, 2006, **74**, 021306.

[219] T. Taylor, M. Schmollngruber, C. Schröder and O. Steinhauser, *J. Chem. Phys.*, 2013, **138**, 204119.

[220] S. Gabl, C. Schröder, D. Braun, H. Weingärtner and O. Steinhauser, *J. Chem. Phys.*, 2014, **140**, 184503.

[221] C. Schröder, T. Rudas, G. Neumayr, W. Gansterer and O. Steinhauser, *J. Chem. Phys.*, 2007, **127**, 044505.

[222] S. Gabl, O. Steinhauser and H. Weingärtner, *Angew. Chem. Int. Ed.*, 2013, **52**, 9242.

[223] K. R. Seddon, A. Stark and M.-J. Torres, *Pure Appl. Chem.*, 2000, **72**, 2275.

[224] M. G. Del Pópolo and G. A. Voth, *J. Phys. Chem. B*, 2004, **108**, 1744.

[225] L. van Hove, *Phys. Rev.*, 1954, **95**, 249.

[226] A. Rahman, *Phys. Rev.*, 1964, **136**, A405.

[227] M. Haberler, C. Schröder and O. Steinhauser, *J. Comput. Theory Chem.*, 2012, **8**, 3911.